Catalytic Autothermal Reforming of Biomass to Synthesis Gas

A DISSERTATION

SUBMITTED TO THE FACULTY OF THE GRADUATE SCHOOL

OF THE UNIVERSITY OF MINNESOTA

BY

Joshua Leigh Colby

IN PARTIAL FULFILLMENT OF THE REQUIREMENTS

FOR THE DEGREE OF

Doctor Of Philosophy

July, 2010

Acknowledgements

I would like to thank Professor Lanny Schmidt for his advice and guidance, and for further developing my understanding of science. I would also like to thank Dr. Paul Dauenhauer, Dr. Bradon Dreyer, Brian Michael and the rest of the Schmidt research group for their insightful discussions, which were not only intellectually stimulating but also very useful for improving my research.

I would also like to thank Professor Eric McFarland and Dr. Michael Sushchikh for their contributions during my undergraduate experience at the University of California at Santa Barbara. Working under their direction I developed a genuine interest in academic research, which eventually lead to my decision to attend graduate school at the University of Minnesota.

Finally, I would like to thank my family for their support in all aspects of life, including my education.

ABSTRACT

As global energy demands continue to soar, natural resources continue to diminish. More than 90% of the global annual energy consumption is derived from non-renewable fossil fuel energy sources. Lignocellulosic biomass in the form of trees, grasses, and agricultural residues provides a realistic source for sustainable production of carbon-based fuels and chemicals. The dominant structure in all non-food sources of biomass, lignocellulose, consists of the biopolymers cellulose, hemicellulose, and lignin in a design that provides optimal materials properties to plant structures while resisting chemical degradation. These same properties also prevent the direct utilization of most conventional petroleum processing equipment thereby driving the development of new technology for handling and processing solid, carbonaceous materials. This thesis examines the catalytic partial oxidation (CPO) of biomass as a potentially more efficient alternative to existing biomass-to-fuel processing techniques.

The majority of research performed on catalytic partial oxidation has used methane as a feedstock for synthesis gas production. The mechanistic insights gained through this work is vital in understanding more complicated CPO systems, such as CPO of biomass. Chapter 2 examines existing literature describing catalytic partial oxidation, its application to gaseous, volatile liquid, and non-volatile liquid fuels, and common catalyst formulations for CPO. It is well documented that Rh-based catalysts provide the most effective and robust catalysts for the partial oxidation of biomass.

Traditional biomass processing technologies suffer from the production of undesired chars and tars resulting from relatively slow reaction rates and heat transfer limitations. Chapter 3 assesses the ability of the catalytic partial oxidation process to overcome these limitations by using the catalytic partial oxidation process to integrate three biomass-to-liquid process steps (volatilization of cellulose, tar-cleaning of organic products, and water-gas-shift of the gaseous effluent) into a single autothermal catalytic reactor for the

production of high quality synthesis gas at millisecond residence times (∼30 ms). Particles of cellulose (∼300 μm) were directly impinged upon the hot, catalytic bed of Rh-Ce/γ-Al_2O_3 catalyst on 1.3 mm α-Al_2O_3 spheres in the presence of O_2, N_2, and steam in a continuous flow fixed-bed reactor at 500-1100 °C. Complete conversion to gases was observed for all experimental parameters including N_2/O_2, steam to carbon ratio (S/C), the total flow rate of cellulose, and the fuel-to-oxygen ratio (C/O). The addition of steam increased the selectivity to H_2 and decreased the selectivity to CO in agreement with water-gas-shift equilibrium. Optimal conditions produced a clean gaseous effluent which exhibited ∼80% selectivity to H_2 at a synthesis gas ratio of H_2/CO=2.3 with no dilution from N_2 at a fuel efficiency of ∼75%. Carbon-free processing was explained by relating the domain of experimental parameters to the thermodynamic prediction for the formation of solid carbon, C_S.

No commercial process exists capable of converting biomass into useful fuels and chemicals without significant carbon losses (50% of fuel carbon) to char or CO_2 because of process or thermodynamic constraints.[1, 2] Chapter 4 focuses on the development of a reactor capable of improving the utilization of biomass-derived carbon during thermochemical conversion to synthesis gas. By co-processing hydrogen-deficient biomass (H/C∼2) with hydrogen-rich feedstocks (H/C≥4) through catalytic partial oxidation over Rh based catalysts, it was demonstrated experimentally that 100% of the fuel carbon atoms fed to the reactor can be converted to CO. Such an improvement in carbon efficiency has the potential to double the yield of biofuels from the limited annual biomass supply. In addition to experimental results, reaction equilibrium calculations are presented describing the limits of the reaction system as dictated by thermodynamics.

Biomass catalytic partial oxidation proceeds in three primary steps: 1) homogeneous carbohydrate pyrolysis at the front face of the catalyst, 2) convection of pyrolysis vapors and co-feeds into the catalyst bed for oxidation, and 3) reforming of the syngas, combustion, and undesired tar products to chemical equilibrium. Chapter 5 focuses

on the reforming zone of the reactor, examining in depth the ability of Rh based catalysts to convert undesired tars to equilibrium synthesis gas products. Experiments were performed in a fixed bed reactor at temperatures of 650-850 °C and atmospheric pressure using C_6H_6 as a model tar compound. Benzene conversion exhibited a strong dependence on temperature and H_2O concentration in the feed. Significantly better catalyst performance was observed upon addition of Ce to the catalyst, which increased Rh dispersion and stability. The concentration of C_6H_6 in the feed had very little effect on catalyst performance. CO_2, H_2, and CO co-feeds had positive, neutral, and negative effects, respectively, on C_6H_6 conversion. A representative biomass-derived syngas mixture of N_2, H_2, CO, CO_2, H_2O, and C_6H_6 was tested on the Rh-Ce catalyst at 850 °C and 2 SLPM total flow rate, resulting in almost complete C_6H_6 conversion to a near equilibrium product stream.

Advanced biomass processing technology integrating fast pyrolysis and inorganic catalysis requires an improved understanding of the thermal decomposition of biopolymers in contact with porous catalytic surfaces. Chapter 6 uses high speed photography (1000 frames per second) to reveal that direct impingement of microcrystalline cellulose particles (300 μm) with rhodium-based reforming catalysts at high temperature (700 °C) produces an intermediate liquid phase that reactively boils to vapors. The intermediate liquid maintains contact with the porous surface permitting high heat transfer (MW m^{-2}) generating an internal thermal gradient visible within the particle as a propagating wave of solid to liquid conversion. Complete conversion to liquid yields a fluid droplet on the catalyst surface exhibiting a linear decrease in droplet volume with time leaving behind a clean surface absent of solid residue (char). Under specific interfacial conditions, conversion with large cellulosic particles on the length-scale of wood chips (millimeters) occurs continuously as generated liquid and vapors are pushed into the porous surface. A more detailed discussion of experimental setups and calculations used in this chapter can be found in Appendix F.

The topics presented in this thesis examine in depth the technical feasibility of using

catalytic partial oxidation to convert biomass to a clean synthesis gas product stream. Through extensive performance testing and process characterization, an in depth understanding of how the fuel feed is converted to product gases is described. Although preliminary testing with clean biomass feedstocks show promising performance with a rapid system approach to thermodynamic equilibrium, further studies are needed to examine the effect of biomass-derived inorganics from non-ideal feedstocks (e.g. corn stover) on Rh-based catalysts. Finally, a technical assessment of the economics associated with distributed catalytic partial oxidation of biomass to fuels and chemicals is needed to determine the feasibility of the overall process.

Contents

List of Tables

List of Figures

Chapter 1

Introduction

As global energy demands continue to soar, fossil fuel resources continue to diminish. This chapter serves to motivate the need for sustainable alternative energy sources, with an emphasis on the important role biofuels will likely play in the near future. The chemical structure of biomass is discussed, elucidating the challenges being encountered in efforts to develop efficient technologies for converting biomass to valuable biofuels. Finally, a brief overview of existing biomass processing technologies is given, focusing on the process of biomass gasification. The research presented in this thesis aims to eliminate the technological hurdles being encountered in traditional biomass gasification processes through a process referred to as catalytic partial oxidation.

1.1 The Energy Crisis

The global energy market currently supplies roughly 12 terawatts for human consumption annually, equivalent to a continuous demand of 13 trillion watts, or 2,000 barrels of oil every second.[3, 4] This already enormous demand is projected to climb considerably within highly developed OECD (Organization for Economic Cooperation and Development) countries, and increase even more dramatically for underdeveloped non-OECD countries.[5]

As global energy demands continue to soar, resources continue to diminish. More than 90% of the global annual energy consumption is derived from non-renewable fossil fuel energy sources, over one-third of which is from oil alone.[4] Dr. M. King Hubbert, who accurately predicted that the U.S. would be forced to become a net importer of oil in the early 1960's and would reach peak domestic oil production in approximately 1970, projected the global oil production peak near the turn of the century, stating that "...[t]here is a different and more fundamental cost that is independent of the monetary price. That is the energy cost of exploration and production. So long as oil is used as a source of energy, when the energy cost of recovering a barrel of oil becomes greater than the energy content of the oil, production will cease no matter what the monetary price may be".[6] Today, experts agree that peak oil production will be within the next couple of decades. Once we have reached peak oil production by extracting the most energy-efficient global oil reserves, then over the next 20-40 years the relative energy efficiency of remaining oil supplies will decrease to a point of diminishing net energy return as energy costs to recover less accessible oil increase.

In addition to having sustainability issues, fossil fuels are the leading contributor to global warming, releasing more than 25,000 million metric tons of carbon dioxide into the atmosphere annually.[5] This number increases substantially every year, and projections estimate the release of over 40 billion metric tons by 2030. Currently the largest source of fossil fuel derived carbon dioxide emissions is oil. Biofuels produce zero net carbon dioxide because they are part of a carbon closed cycle. To avoid potentially irreversible climate changes, energy sources with zero net carbon dioxide emissions must be exploited.

Driven by economics, the world is moving toward a new era of resource management where only attempting to 'reduce, reuse, and recycle' non-renewable resources will no longer suffice. People will be forced to replace their dependence on fossil fuels with sustainable alternative energy resources.

1.2 Motivations for Biofuels

Liquid hydrocarbons are appealing for their extremely high energy density and ease of storage. Collectively, these characteristics are unique to carbon-rich liquid fuels currently produced almost entirely from oil. Biomass, the only source of renewable carbon, represent the only sustainable feedstock for the production of carbon-rich fuels referred to as 'biofuels'.[7] Although the general public tends to associate the term 'biofuel' with ethanol and biodiesel, there are many other forms. These fuels include other transportation fuels such as dimethyl ether, methanol, dimethyl furan, mixed alcohols, Fischer-Tropsch diesel, heating gases such as synthesis gas (syngas) and methane, and simply using the solid biomass (i.e. wood) for its heating value.[8, 9, 10]

Reducing society's dependence on fossil fuels will almost certainly require a broad array of alternative energy resources and technologies. However, biofuels will likely play a key role in these efforts, namely in the transportation sectors. A number of other renewable energy sources are being considered for the transportation sectors such as electricity for battery powered vehicles and H_2 for internal combustion engines or fuel cells. Using current storage technologies these sources are at best 75% less energy dense than liquid fuels, preventing their application in airplanes, trains, buses, and even cars.[11]

The extent to which biofuels can meet the United States' growing energy demands is a key concern. The first step to addressing this issue is quantifying available biomass resources. A recent joint study between the US Departments of Energy and Agriculture investigated the potential sustainable domestic biomass production assuming feasible infrastructure changes. It was determined that about 368 million dry tons of harvestable biomass could be produced annually on forestlands, and 998 million dry tons from agricultural lands.[12] This represents a sustainable annual biomass harvest of 1.3 billion dry tons per year. This is enough biomass, for example, to produce more than one-third of US transportation fuel with existing technologies.[12] As biomass processing

technologies continue to develop, it is likely a larger fraction of the US energy demand will be met with available biomass resources. Furthermore, a more aggressive expansion of agricultural resources would increase the feedstock supply.

Biofuels are also appealing because they generate less greenhouse gas emissions than fossil fuels.[1, 9, 10, 13] If renewable sources of energy are used in the production of biofuels, the biofuels are completely carbon neutral, contributing no net carbon dioxide to the atmosphere. This is in contrast to fossil fuels, which take millions of years to form and, at current rates, only a matter of centuries to consume. The reduction of carbon dioxide placed into the atmosphere by an increased use of biofuels can help slow anthropogenic global warming.

1.3 The Structure of Biomass

There is a distinction between biomass and lignocellulosic biomass. Biomass refers to all plant matter and animal waste, including all types of trees, grasses, animal feces, agricultural residues such as corn stover and straw, and aquatic plants. Lignocellulosic biomass refers more specifically to the main physical structure of biomass, composed of cellulose, hemicellulose, and lignin. Other components of biomass, besides lignocellulosic materials, include extractives (such as starch found in corn kernels), uronic acids, and inorganic compounds (commonly referred to as ash). This section serves to introduce the chemical structure of biomass with a focus on the three components of lignocellulosic biomass, which comprise nearly 90% of all plant matter.[14]

1.3.1 Cellulose

The most abundant component of biomass is cellulose, a long chain polysaccharide with chemical formula $(C_6H_{10}O_5)_n$. This polysaccharide is essentially composed of many glucose monomers, formally referred to in their cellulose polymer form as glucopyranose. The $\beta(1,4)$-glycosidic bonds connecting these monomers create a fully equatorial chair

structure, minimizing the flexibility of cellulose and giving it very high tensile strength. These bonds form amorphous and crystalline regions, far more crystalline when compared to starch which is also composed of glucose monomer units but connected by a highly branched $\alpha(1,4)$ bonding pattern. Cellulose polymer units are linear chains that typically range from 7,000 to 15,000 monomers in length.[15] The chemical formulation of cellulose is critical to the integrity of plant cell walls, where cellulose polymers are woven into a complex carbohydrate matrix that keeps plant structures rigid. Much of the research presented in this thesis focuses on the conversion of cellulose to fuels and chemicals.

1.3.2 Lignin

Lignin and hemicellulose compose approximately the same weight fraction of biomass, lignin being slightly more abundant in softer species such as balsa wood.[14] Lignin is a highly cross-linked macromolecule with average mass generally exceeding 10,000 AMU. Individual lignin macromolecules range dramatically in structure and size due to the seemingly random cross-linking that occurs during their formation. Large amounts of aromatic and hydrophobic molecules form lignin, but the exact chemical structure varies between lignin molecules. Lignin is woven into plant cell walls with cellulose and hemicellulose, enhancing overall molecular cross-linking in the biomass. The hydrophobic structure of lignin creates defined pathways for vascular systems to form in plants resulting in efficient transport of water. Another important characteristic of lignin is that it is inherently difficult to degrade, serving as a natural defense mechanism for plants by preventing pathogens such as bacteria and molds from penetrating the cell walls.[16]

1.3.3 Hemicellulose

Hemicellulose is a heteropolymer usually containing glucose, mannose, arabinose, and xylose monomers, comprising 20% to 30% of biomass dry-weight.[14] More generally, hemicellulose is all polysaccharide components of the cell wall other than cellulose. The

hemicellulose polymer chains are usually on the order of 200 monomers long, significantly shorter than those of cellulose. Additionally, the shorter hemicellulose polymers are highly branched, compared to the linear conformation of cellulose. Because of its branching structure, hemicellulose naturally intertwines with other molecules in cell walls and accounts for much of the transversal strength and elasticity in a cell, whereas cellulose accounts for most of the plant's longitudinal strength.[17]

1.3.4 Other Components of Biomass

Besides the lignocellulosic portions of biomass, there are extractives, uronic acids, and inorganic compounds. Extractives are defined as compounds that are not lignocellulosic materials and are soluble in common solvents. Uronic acids are extractives that have oxidized into acids. Inorganic compounds typically found in biomass include copper, iron, potassium, magnesium, and lead. Although non-lignocellulosic components of biomass make up only a small fraction of the material, they can create significant complications in biomass processing and can affect the overall economics of the process. In particular, inorganic compounds are an issue during thermochemical conversion of biomass, especially in processes that use catalysts.

1.4 Biomass Processing Technologies

The efficient conversion of biomass to value-added chemicals is extremely difficult given the complex mixture of organic compounds and inorganic impurities in the feedstock.[9] However, several technologies introduced over the past few decades have demonstrated potential for strong economics, large volume production, and feedstock flexibility. These technologies can be categorized into three primary routes for upgrading biomass to value-added chemicals: 1) biological routes for liquid fuel production, 2) liquefaction and fast pyrolysis for bio-oils production, and 3) gasification for synthesis gas production.[7, 14]

1.4.1 Biological Routes to Liquid Fuels

Ethanol produced through the enzymatic fermentation of corn kernel starch is the principal domestic renewable transportation fuel.[18] It is also the primary biofuel considered for production via biological routes from lignocellulosic biomass.[2, 19] This process involves three main steps: 1) biomass pretreatment, 2) hydrolysis, and 3) fermentation.

Biomass pretreatment makes the feedstock more susceptible to chemical and enzymatic hydrolysis. This improves process efficiencies and reduces deactivation of enzymes and microbial agents. Pretreatment accomplishes this by: 1) removing and separating hemicellulose from cellulose, 2) disrupting and removing lignin, 3) decreasing cellulose crystallinity, and 4) increasing accessible surface area of cellulose.[20] Although necessary, pretreatment is expensive and results in poor process economics when compared to starch based ethanol production.[7]

After separation, lignin is typically used for its heating value since upgrading to liquid fuels is prohibitively expensive. Cellulose and hemicellulose undergo hydrolysis and are decomposed to simple sugars by acids or the enzyme cellulose.[7] Cellulose decomposes primarily to glucose (with yields greater than 95%), whereas hemicellulose hydrolyzes to a mixture of mainly xylose and glucose, with small amounts of arabinose, galactose and mannose.

The final step is the conversion of sugars to ethanol, typically through fermentation by yeast. Many processes ferment hemicellulose and cellulose separately because glucose ferments in approximately 2 hours, but xylose requires up to 72 hours.[20]

Biological processing of lignocellulosic biomass to ethanol has demonstrated potential but has technical barriers to overcome before commercialization. The primary problems are costly preprocessing of lignocellulosic materials, slow fermentation of sugars from hemicellulose, and high sensitivity to feedstock variability. These problems generate poor economics relative to the process of converting corn starch to ethanol, a process that already requires large government subsidies to be competitive in the

marketplace.[18]

1.4.2 Production of Liquid Fuels by Liquefaction and Fast Pyrolysis

Bio-oil, a liquid biofuel, can be produced by thermochemical decomposition of biomass, namely through liquefaction or fast pyrolysis. Biomass is heated in the absence of oxygen, thermally decomposing bonds without combustion to permanent gases. The resulting bio-oil is a complex mixture of up to 400 different hydrocarbons including acids, alcohols, aldehydes, esters, ketones, and aromatic compounds.[7]

The most prevalent process for industrial bio-oil production is fast pyrolysis in fluidized beds, circulating fluid beds, ablative pyrolyzers, or vacuum pyrolyzers.[7] Fast pyrolysis is the process of heating biomass to 450-550 °C in the absence of air, typically at atmospheric pressure. Modern reactors have up to an 80% yield of bio-oil by weight, with residence times on the order of seconds to minutes.[14] Production is limited in large capacity reactors as they require high heat transfer rates to provide enough energy to drive the endothermic reactions in such short residence times. Bio-oil produced by fast pyrolysis is high in water and oxygen content, resulting in a lower heating value (17 MJ kg^{-1}) compared to that of conventional fuels (43 MJ kg^{-1}).[21] Furthermore, the fuel is not at thermodynamic equilibrium, and slowly degrades to lighter species during storage.

Bio-oil is also produced by liquefaction of biomass, a process where biomass is suspended in a solvent then reacted at 250-450 °C and 50-200 atm. Common solvents include water, ethylene glycol, methanol, and recycled bio-oil; water being the most common because of its low cost. Residence times for this process are generally 10-30 minutes due to lower temperatures and therefore slower rates of reaction. Advantages of liquefaction include high thermal efficiencies for conversion of wet feedstock (most notably when water is the solvent) and easily scalable processing.[21] The primary benefit of this process is that solvent, pressure, temperature, and catalyst can be adjusted to produce a higher grade bio-oil that has less oxygenated species and a higher

heating value (34 MJ kg^{-1}), relative to fast pyrolysis.[22] These reaction conditions can also be tuned to increase selectivity to specific product species, which is appealing when producing bio-oil for specialty chemicals rather than as heating fuel. Downsides of liquefaction include high operating and capital costs because of the high operating pressures.

Bio-oil is currently used for heating value and specialty chemical production. Expansion of these oils into other markets is currently difficult because of their higher cost relative to fossil fuels (10-100% higher).[1] Furthermore, high viscosity, thermal instability, corrosiveness, and mixture inhomogeneity make bio-oil difficult to directly substitute for existing fossil fuels.[22] Bio-oil upgrading processes, comparable to existing crude oil refining techniques, are currently being developed to alleviate these problems.[7, 21, 22] However, the economics of crude bio-oil production must be improved to facilitate large-scale commercialization.

1.4.3 Gasification of Biomass to Synthesis Gas and Upgrading to Liquid Fuels

Biomass gasification is the process in which biomass or biomass derivatives react with oxygen and/or steam to produce synthesis gas. Synthesis gas (syngas) is a mixture of hydrogen (H_2) and carbon monoxide (CO), and is so named because it can be used to synthesize a large variety of liquid fuels including gasoline, diesel fuel, methanol, and ethanol. Syngas can also be used as a medium BTU value gas for heat or electricity generation, or the hydrogen can be separated as a fuel. Currently, most syngas is produced through the gasification of fossil fuels, namely methane and coal. However, recently attention has shifted towards using biomass as a feedstock for syngas production.

Gasification of biomass has attracted more interest than pyrolysis or liquefaction because of its higher energy efficiency and simple product mixture.[1] Its insensitivity to feedstock variability is also appealing, in contrast to existing biological processing technologies. Gasification offers the potential for a simple, robust process for large-scale

commercial biofuels production, unlike biological routes and pyrolysis or liquefaction.

However, several technical barriers currently hinder the economics of gasification processes. The formation of tars during biomass gasification is "the most cumbersome and problematic parameter in any gasification commercialization effort".[23] Tars are high molecular weight hydrocarbons that can condense from the effluent, damaging equipment and requiring costly downstream cleanup stages. Gasification projects often fail based purely on the added cost of tar removal.[7] Tars form as a result of incomplete conversion of biomass to permanent gases, usually caused by heat transfer limitations. The addition of catalysts to the process is reported to minimize tar production during biomass gasification, but heat transfer limitations require prohibitively long reactor residence times for complete tar removal. Furthermore, existing gasification technologies are sensitive to biomass water content, which has a large heat capacity capable of further slowing an already heat transfer limited process. Solid carbon formation is also a problem during biomass gasification as it can deactivate catalysts and lowers CO yields.[23] Finally, existing biomass gasification processes are scale-sensitive and only efficient when built as large units. However, biomass demands localized, small-scale plant construction since it is a diffuse resource and expensive to transport.

Gasification continues to attract interest as a process to efficiently convert biomass to value added chemicals, heat, and electricity. It offers a robust, simple alternative to biological, pyrolysis, and liquefaction processing technologies. However, undesirable tar and carbon formation, sensitivity to water, and poor small-scale economics must be resolved before large-scale commercialization of this process can be realized.

1.5 Summary

Lignocellulosic biomass gasification is a robust process for producing syngas, used for its heating value, electricity generation, and the synthesis of fuels and chemicals. However, current technologies demonstrate mediocre economics for the production of syngas, and

conversion of syngas to liquid fuels. “The greatest impact on improving the economics of [synthesis] gas to liquids plants is through 1) decreasing capital costs associated with syngas production and 2) improving the thermal efficiency with better heat integration and utilization”.[24] More specifically, commercialization of existing gasification processes are hindered by: 1) tar formation, 2) carbon formation, 3) sensitivity to water, 4) inefficient carbon utilization, and 5) poor small-scale economics.

This thesis focuses on the development of a novel biomass to synthesis gas process void of limitations observed in traditional gasification reactors. By applying a process referred to as catalytic partial oxidation to biomass gasification, it is shown that high efficiencies can be realized even at small scales through heat integration and the use of Rh-based catalysts. Such a technology could substantially improve gasification process economics by reducing both capital and operating costs.

Chapter 2

Catalytic Partial Oxidation

Most research on catalytic partial oxidation has used methane as a feedstock for synthesis gas production. The mechanistic insights gained through this work is vital in understanding more complicated CPO systems, such as CPO of biomass. This chapter focuses on existing literature describing catalytic partial oxidation, its application to gaseous, volatile liquid, and non-volatile liquid fuels, and common catalyst formulations for CPO.

2.1 The Catalytic Partial Oxidation Process

Methane is the most popular feedstock for syngas production because it is inexpensive and abundant. Methane steam reforming (Eqn. 2.1) is currently the primary process used for large scale industrial syngas production.

$$CH_4 + H_2O \rightarrow CO + 3H_2, \qquad \Delta H^o_{rxn} = 206\ kJ\ mol^{-1} \tag{2.1}$$

However, this process is only economically competitive on large scales, which are unappealing for construction in remote gas fields. Furthermore, the process is endothermic, requiring significant heat inputs and contributing to transport issues that limit the process residence time to $\sim$1 second.

The catalytic partial oxidation (CPO) of methane (Eqn. 2.2) has been researched extensively as a route for the efficient production of syngas on small scales. The process works by partially oxidizing a fuel with oxygen over a fixed bed noble metal catalyst to form hydrogen and carbon monoxide.

$$CH_4 + \frac{1}{2}O_2 \rightarrow CO + 2H_2, \qquad \Delta H^o_{rxn} = -36\ kJ\ mol^{-1} \tag{2.2}$$

CPO is exothermic and proceeds at extremely high reaction rates, with nearly complete conversion of methane to syngas at millisecond contact times. Because the reaction is exothermic and proceeds so rapidly it can run autothermally, meaning the reactor is self heating and no external energy sources are required. As a result, it can be easily constructed on small scales ideal for remote locations. Furthermore, CPO of methane produces a syngas ratio of H_2/CO=2, ideal for methanol and Fischer-Tropsch liquid fuel production.

The precise mechanism by which the partial oxidation of methane occurs on catalyst surfaces remains an area of research and debate. The two primary global mechanisms that have been proposed are: 1) a direct mechanism by which H_2 and CO are directly formed through partial oxidation of methane, and 2) an indirect mechanism that states methane is strongly combusted to H_2O and CO_2 before undergoing steam and carbon dioxide reforming to form syngas. Others also report a mechanism that involves significant contributions from both the direct and indirect mechanisms.

Although the specific mechanism is still debated, experimental data has been obtained that describes two distinct zones in the CPO of methane.[25] Spatial species concentration profiles measured along the axis of catalyst loaded foam monoliths using a micro-capillary sampling technique revealed the existence of an oxidation zone in the first portion of the catalyst followed by a reforming zone toward the downstream side of the catalyst.[26]

The existence of two reaction zones makes possible the autothermal behavior of this process. Traditional syngas production only uses the endothermic steam reforming

reaction. CPO utilizes partial combustion at the upstream side of the catalyst, which generates large amounts of heat. This heat is continuously conducted downstream through the catalyst support, where it is used to power the endothermic reforming reactions. Although a series of reaction pathways are used, the global reaction can be described by Equation 2.2, which is net exothermic.

In addition to methane many other fuels can be used as a feedstock for CPO such as a variety of volatile liquids (e.g. ethanol) and non-volatile liquids (e.g. soy oil). Catalytic partial oxidation of ethanol was demonstrated in a reactor analogous to that described for methane partial oxidation.[27] It was shown that ∼100% selectivity to hydrogen could be achieved at ≥95% conversion of ethanol at millisecond catalyst contact times.

The general mechanism by which ethanol is converted to syngas during CPO is thought to be similar to that described for methane.[27, 28] Ethanol enters the reactor in the presence of oxygen where it is oxidized toward the upstream side of the catalyst, followed by reforming chemistry on the downstream side. The CPO of methane and ethanol differ primarily in their heats of reaction. Partial oxidation of ethanol is slightly endothermic (Eqn 2.3) and the system cannot maintain autothermal operation without additional heat.

$$C_2H_5OH + \frac{1}{2}O_2 \rightarrow 2CO + 3H_2, \qquad \Delta H^o_{rxn} = 20\ kJ\ mol^{-1} \tag{2.3}$$

In order to create an autothermal process, a small portion of the ethanol must be fully oxidized. This provides necessary heat to the reforming zone, where the primary reactions are ethanol steam reforming and water-gas-shift (WGS) reactions, while sacrificing selectivity to syngas. In order to increase hydrogen selectivity to the reported value, water can be added to shift the WGS equilibrium. The global reaction for this system can be described by the net exothermic reaction of Equation 2.4.

$$C_2H_5OH + 2H_2O + \frac{1}{2}O_2 \rightarrow 2CO_2 + 5H_2, \qquad \Delta H^o_{rxn} = -50\ kJ\ mol^{-1} \tag{2.4}$$

Catalytic partial oxidation of non-volatile fuels, such as soy oil, was also demonstrated in a reactor analogous to that described for methane partial oxidation.[29] It

was shown that ∼80% selectivity to syngas could be achieved at ∼100% conversion of soy oil at millisecond catalyst contact times.

The general mechanism by which CPO converts soy oil to syngas likely follows a similar process to that described for methane once.[29] However, there is a third zone in process of CPO for all non-volatile fuels. Unlike the CPO gaseous or volatile liquid feedstocks, non-volatile fuels must undergo homogeneous pyrolytic reactions on the front face of the catalyst before being convected into the catalyst bed. The pyrolysis process is also endothermic; heat generated in the oxidation zone must not only be conducted downstream to the reforming zone, but also upstream to the catalyst front face. In order to make the process autothermal, a portion of the soy oil feed must be fully oxidized to provide the additional heat.

The catalytic partial oxidation of biomass is in many ways analogous to CPO of non-volatile liquids.[30] Biomass CPO involves the same three zones: pyrolysis, oxidation, and reforming. Some of the biomass must be fully combusted to provide heat for endothermic polymer decomposition at the front face of the catalyst and for reforming toward the downstream side of the catalyst bed. This thesis focuses on the application of the catalytic partial oxidation process to biomass feedstocks.

2.2 Catalyst Selection

2.2.1 CPO over Rhodium

At the core of the catalytic partial oxidation process is a catalyst capable of rapidly converting fuel and oxygen to synthesis gas. Noble metals have been demonstrated to be highly effective partial oxidation catalysts. Specifically, rhodium is generally considered the most effective catalyst for syngas production, used in all catalytic processes presented in this thesis.[26] Rhodium is capable of catalyzing reforming reactions and approaching water gas shift equilibrium more effectively than other noble metals, such as platinum, which favors total oxidation.[25] Rhodium is also highly resistive to surface

carbon formation, a significant source of deactivation for many competing catalysts.[31]

Rhodium is unique as a group 9 d-block transition metal because it has only one electron in its d-orbital when in ground state. It is known for its catalytic properties, capable of forming a complex with species that can donate lone electron pairs, lowering their activation energy for reaction. Furthermore, rhodium is capable of residing in multiple oxidation states, facilitating the gain and loss of electrons and powering redox reactions with adsorbed species.

2.2.2 Catalyst Supports and Promotion

In addition to catalyst selection, choosing an effective catalyst support is extremely important. Although common supports of Rh-based catalysts can improve overall performance through catalyst promotion, the support is generally selected to: 1) increase catalyst dispersion thereby reducing the amount of catalyst needed, improving performance, or both, 2) improve catalyst stability by reducing sintering, and 3) resist attrition, increasing the lifetime of the catalyst. α-Al_2O_3 was selected as the primary support for all experiments presented in this thesis.

Two geometries of α-Al_2O_3 supports were used: 1) Sud-Chemie Hi-Tech Ceramics Corporation 65 ppi (pores per linear inch) α-Al_2O_3 monolithic foams with an unmodified surface area on the order of 100 cm^2 g^{-1}, and 2)Saint-Gobain NorPro Corporation 1.3 mm diameter α-Al_2O_3 spheres with an unmodified surface area of 5.35 m^2 g^{-1}.[32]

The α-Al_2O_3 monolithic foams were used to gain kinetic insights and for comparison with previously published results on catalytic foams, where catalyst performance was not the primary concern. Their low surface areas (Fig. 2.1) make them non-ideal for high catalyst dispersions and, therefore, efficient catalyst performance. At only 2.5 wt% Rh loading, it is observed that the monolith supports have low enough surface areas to be completely covered in Rh (Fig. 2.2), rendering most of the Rh unused (dispersions $\leq$1%).

The α-Al_2O_3 spheres were used for their high surface area (Fig. 2.1), resistance to attrition, and industrial relevance. At 2.5 wt% Rh loading, the α-Al_2O_3 sphere

supports yielded a catalyst dispersion of 8.3%, measured by H_2 pulsed chemisorption. Assuming hemispherical catalyst particle geometry, this corresponds to an average Rh nanoparticle diameter of 19 nm, in close agreement with the particles observed by scanning electron microscopy (Fig. 2.2). Such high Rh dispersions are appealing for high catalyst performance at low Rh loadings.

The application of catalyst washcoats and promoters are often used to enhance the performance of Rh-based catalysts. Applying a metal washcoat, namely γ-Al_2O_3 powder, to the catalyst support prior to catalyst deposition has been shown to increase the porosity and roughness of the support.[33] This enhanced porosity increases surface area for reactant contact with the rhodium catalyst and the increased roughness promotes mixing within the catalyst, improving transport properties. The addition of promoters, namely ceria, has been shown to increase water gas shift activity, driving the reaction more rapidly to chemical equilibrium.[28, 34] Additionally, ceria is thought to increase surface oxidation activity, increasing conversion of surface carbon to CO and CO_2.

All experiments presented in this thesis used Rh-based catalysts with one of the two aforementioned α-Al_2O_3 supports. Some of these catalysts also had a γ-Al_2O_3 washcoat or a cerium promoter. Details describing the synthesis of each catalyst are presented individually in the following chapters.

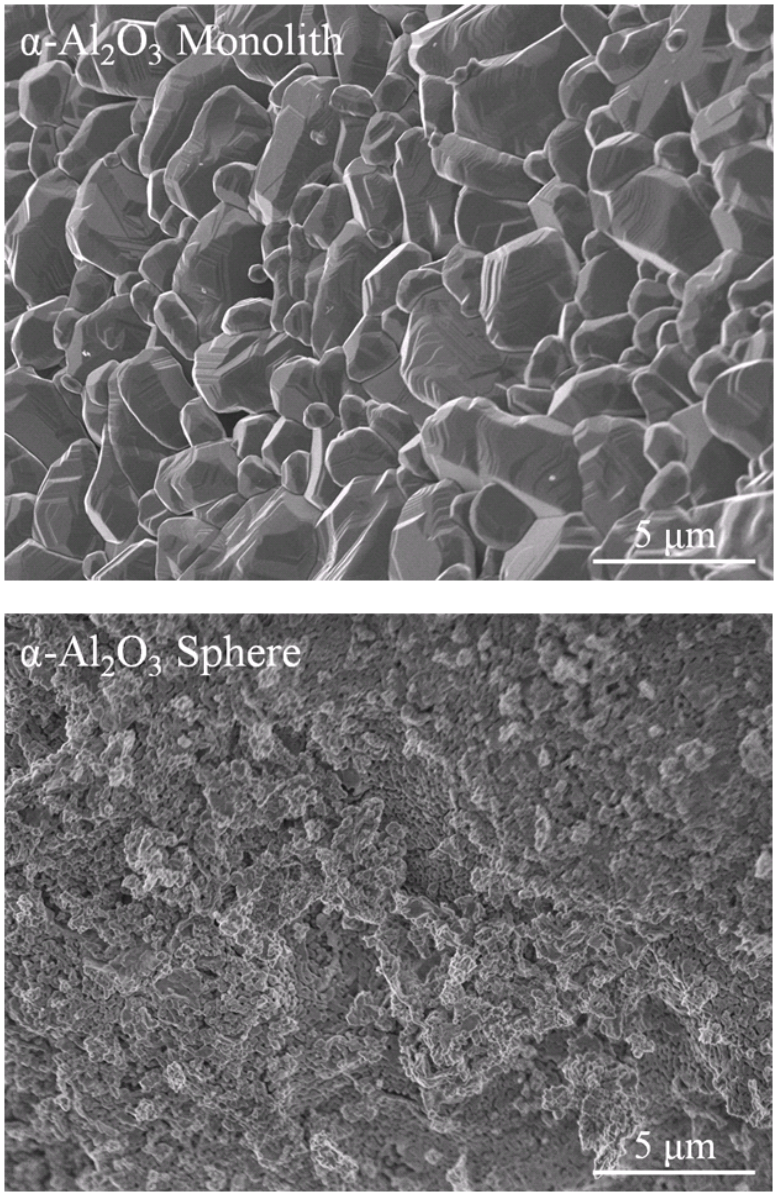

Figure 2.1: Top: Scanning electron micrograph of a 65 ppi α-Al_2O_3 foam monolithic support. The support has extremely low surface areas resulting in poor catalyst dispersions. Detector information: SEI, kV: 3.0, Mag.: 5,000, WD: 9.7 mm. Bottom: Scanning electron micrograph of a 1.3 mm diameter α-Al_2O_3 spherical support. The support has a significantly higher surface area than the monolithic foam support, resulting in significantly higher catalyst dispersions. Detector information: SEI, kV: 2.0, Mag.: 5,000, WD: 3.6 mm.

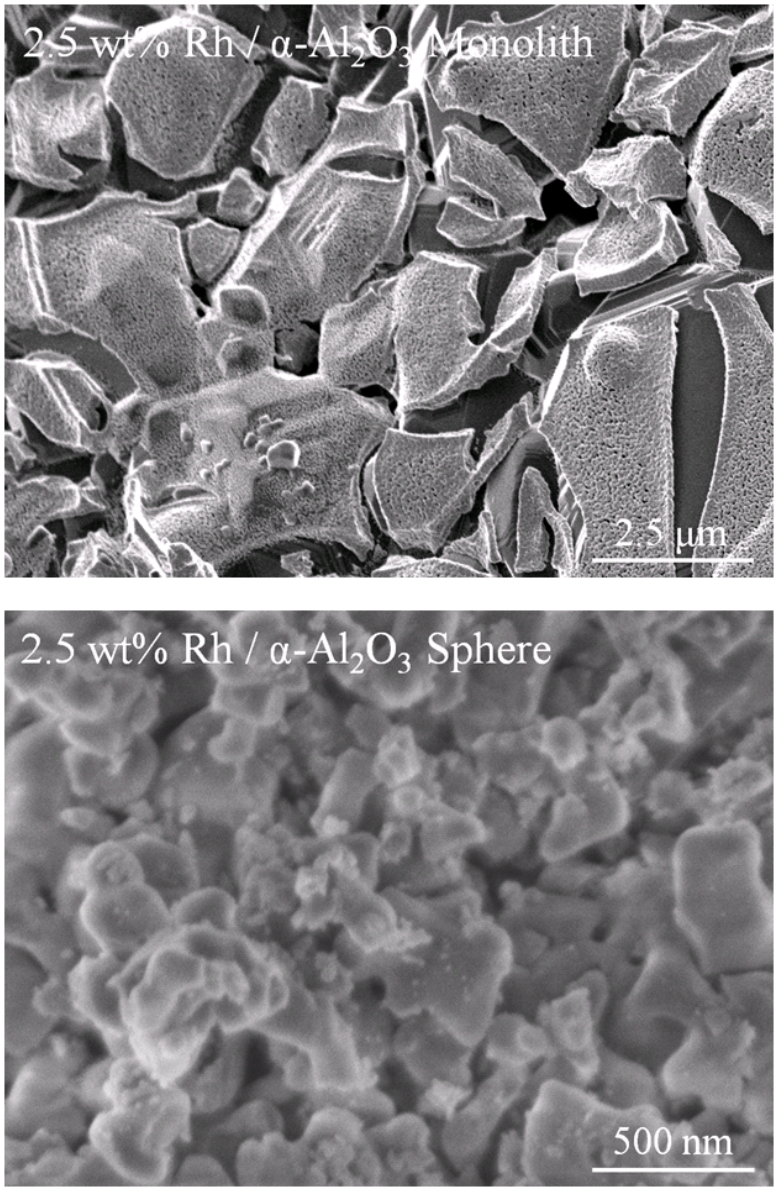

Figure 2.2: Top: Scanning electron micrograph of a 65 ppi α-Al_2O_3 foam monolithic with 2.5 wt% Rh. The low support surface area results in complete catalyst coverage by bulk Rh, leaving much of the Rh unutilized during reaction. Detector information: SEI, kV: 2.0, Mag.: 10,000, WD: 8.6 mm. Bottom: Scanning electron micrograph of a 1.3 mm diameter α-Al_2O_3 spherical support with 2.5 wt% Rh. The high support surface area results in high catalyst dispersion with an average Rh particle size of $\sim$20 nm. Detector information: SEI, kV: 2.0, Mag.: 50,000, WD: 3.5 mm.

Chapter 3

Millisecond Autothermal Steam Reforming of Cellulose for Synthetic Biofuels by Reactive Flash Volatilization[1]

Traditional biomass processing technologies suffer from the production of undesired chars and tars resulting from relatively slow reaction rates and heat transfer limitations. This chapter assesses the ability of the catalytic partial oxidation process to overcome these limitations by using a catalyst to increase reaction rates and through the internal generation of process heat in a compact, integrated process.

Three biomass-to-liquid process steps (volatilization of cellulose, tar-cleaning of organic products, and water-gas-shift of the gaseous effluent) have been integrated into a single autothermal catalytic reactor for the production of high quality synthesis gas

[1] **Parts of this chapter appear in: J.L. Colby, P.J. Dauenhauer and L.D. Schmidt, "Millisecond autothermal steam reforming of cellulose for synthetic biofuels by reactive flash volatilization,"** ***Green Chemistry*****, 2008, 10, 773-783 - Reproduced by permission of The Royal Society of Chemistry (RSC).**

at millisecond residence times (∼30 ms). Particles of cellulose (∼300 μm) were directly impinged upon the hot, catalytic bed of Rh-Ce/γ-Al_2O_3 catalyst on 1.3 mm α-Al_2O_3 spheres in the presence of O_2, N_2, and steam in a continuous flow fixed-bed reactor at 500-1100 °C. Complete conversion to gases was observed for all experimental parameters including N_2/O_2, S/C, the total flow rate of cellulose, and the fuel-to-oxygen ratio (C/O). The addition of steam increased the selectivity to H_2 and decreased the selectivity to CO in agreement with water-gas-shift equilibrium. Optimal conditions produced a clean gaseous effluent which exhibited ∼80% selectivity to H_2 at a synthesis gas ratio of H_2/CO=2.3 with no dilution from N_2 at a fuel efficiency of ∼75%. Carbon-free processing was explained by relating the domain of experimental parameters to the thermodynamic prediction for the formation of solid carbon, C_S.

3.1 Introduction

Lignocellulosic biomass in the form of trees, grasses, and agricultural residues provides a realistic source for sustainable production of carbon-based fuels and chemicals.[18, 35] Recent analysis by the U.S. Department of Agriculture estimates that annual production of lignocellulosic biomass could exceed one billion dry tons, providing sufficient energy to supplant a significant fraction of existing demand for fossil fuels.[12] The dominant structure in all non-food sources of biomass, lignocellulose, consists of the biopolymers cellulose, hemicellulose, and lignin in a design that provides optimal material properties to plant structures while resisting chemical degradation. These same properties also prevent the direct utilization of most conventional petroleum processing equipment thereby driving the development of new technology for handling and processing solid, carbonaceous materials.

Conversion of biopolymers to synthesis gas (H_2 + CO) and subsequent production of synthetic fuels is a major thermochemical processing route commonly called

biomass-to-liquid (BTL). The entire BTL process consists of a combination of unit operations including biomass preparation, gasification, synthesis gas cleaning, synthesis gas processing, synthetic fuel production, and synthetic fuels refining. The availability of technologies and number of process variables for each process step provides an enormous number of configurations and design options which must be evaluated as an integrated system for optimal process development.[10] The overall process competes economically with existing biological processes (e.g. corn to ethanol) as demonstrated by a recent process design analysis of the BTL process for the production of ethanol from wood.[36]

The efficacy of the BTL process can be enhanced by either improving the performance of any single process step or by eliminating or combining process steps. A significant opportunity for process improvement exists with synthesis gas production and preparation. The cost of conversion to clean, conditioned synthesis gas for a synthetic fuels reactor can dominate process economics as this equipment can comprise 60-75% of the total process investment.[37, 38] This chapter demonstrates that at least three BTL process steps (gasification, tar-cleaning, and water-gas-shift) can be combined as a one-step millisecond residence time reactor for continuous operation. Each of these steps provides a necessary process function and contributes a non-negligible capital and operating cost. Conventional biomass gasifiers (updraft, downdraft, and fluidized bed) partially oxidize biomass to a gaseous syngas-rich effluent that commonly contains impurities such as tars and aromatics, unconverted oxygenated organics, nitrogen-containing species such as NH_3 or HCN, and soot.[39] Organic impurities must be selectively removed to ppm levels by one of several technologies that can be categorized into wet scrubbing, dry scrubbing, or hot gas conditioning.[23] Existing techniques applicable to the integrated reactor considered here include steam reforming and partial oxidation of tars and organics using Ni, Pt, or Rh metal catalysts. Biomass-derived synthesis gas typically exhibits a $H_2/CO \sim 1.0$, and an additional process step must also be used to adjust the ratio of H_2 to CO by the water-gas-shift reaction for synthetic fuel reactors to

produce Fischer-Tropsch alkanes ($H_2/CO{\sim}2$), methanol for dimethyl ether ($H_2/CO{\sim}2$), or mixed alcohol fuel ($H_2/CO{\sim}1.2$).[36]

An extremely short residence time (milliseconds) reactor integrating at least three process steps provides the possibility for dramatic improvement in the utilization of biomass for synthetic fuels. Conventional gasifiers exhibit residence times on the order of seconds to minutes, while catalytic partial oxidation of organic compounds occurs in milliseconds permitting a reduction in biomass reactor size by at least an order of magnitude. Additionally, combined chemistries permit simpler overall processes by eliminating multiple process vessels and ancillary equipment. The capital costs of traditional BTL equipment has restricted the processes to large scales ($\sim$400 MW_{th}), demanding an abundant, local supply of biomass.[38] Small efficient processes allow for localized processing facilities, reducing costs associated with biomass transportation.

A highly integrated, millisecond biomass reactor operates faster and with more functionality than a large number of existing catalytic gasifiers. There exist numerous experimental examples of the integration of metal catalysts such as Ni, Co, and Rh with conventional fluidized bed gasifiers to reduce the production of char and tars *in situ*.[40, 41, 42] Most gasification catalysts exhibit deactivation and poisoning due to the development of surface carbon (coke) and char and the condensation of inorganic ash. Rh-based catalysts with the addition of Ce have exhibited significant resistance to the formation of coke in the oxidative reforming of tars and organics.[43, 44] Additionally, catalytic partial oxidation of highly oxygenated organic compounds such as ethylene glycol and glycerol on RhCe catalysts has selected for equilibrium concentrations of synthesis gas during steady, autothermal operation on millisecond time-scales.[28] The utilization of RhCe fluidized catalytic beds integrated with volatilization of carbohydrate-rich solids has demonstrated reduced tar formation, but has been restricted to indirectly heated processes and residence times on the order of one second.[45]

The direct impingement of solid particles of carbohydrate-rich biomass with a hot

(T>700 °C), catalytic surface in thermal contact with a catalytic bed provides an optimal situation for fast, integrated processing of nonvolatile feedstock material. We have recently demonstrated this technique, referred to as 'reactive flash volatilization,' on Rh-Ce catalytic beds for the air-blown reforming of soy oil, cellulose, and lignocellulose.[29, 30] Multiple zones of chemistry (volatilization, oxidation, and reforming) provide efficient chemical routes to synthesis gas. Particles contacting a hot surface volatilize to gases and volatile organic compounds (VOCs) which can flow into the catalyst bed and oxidize to synthesis gas and combustion species. The remaining gases and VOCs after ≥99% oxygen conversion can then steam reform to gases and equilibrate by the water-gas-shift (WGS) reaction. Autothermal processing is realized between endothermic zones (volatilization and reforming) and the exothermic oxidation chemistry through balanced heat transfer by conduction in the alumina catalyst support and convection forward by the process gases.

The adjustment of chemistry and heat transfer by the addition of steam and removal of feed N_2 provides the opportunity to reduce effluent synthesis gas dilution and fully integrate the water-gas-shift step within the millisecond reactor. RhCe catalysts have demonstrated strong activity for the water-gas-shift reaction on millisecond timescales.[34] In this study we demonstrate the tunability of the synthesis gas ratio by adjusting the feed S/C (steam-to-carbon) ratio, the C/O (carbon-to-oxygen) ratio, the N_2/O_2 (feed nitrogen/feed oxygen) ratio, and the total flow rate of solid material. Spatial temperature measurements were conducted along the axis of the catalyst bed to analyze system behavior and define process limitations. Additionally, system performance is analyzed through thermodynamic analysis, and the domain of operation is presented for considered feed parameters. Finally, the results lead to the development of an autothermal, steady-state operating configuration that permits integration of gasification, tar-cleaning, and water-gas-shift chemistry in the absence of nitrogen at high process feed rates and millisecond residence times.

3.2 Experimental

3.2.1 Reactor Design

The autothermal steam reforming of cellulose was performed in a 20 mm I.D., 22 mm O.D. quartz tube shown in Fig. 3.1. A 17 mm O.D. ceramic foam monolith, used to support the 30 mm bed of spherical catalysts, was inserted into the quartz tube from the bottom and held in place via friction fit against the reactor wall with ceramic cloth.

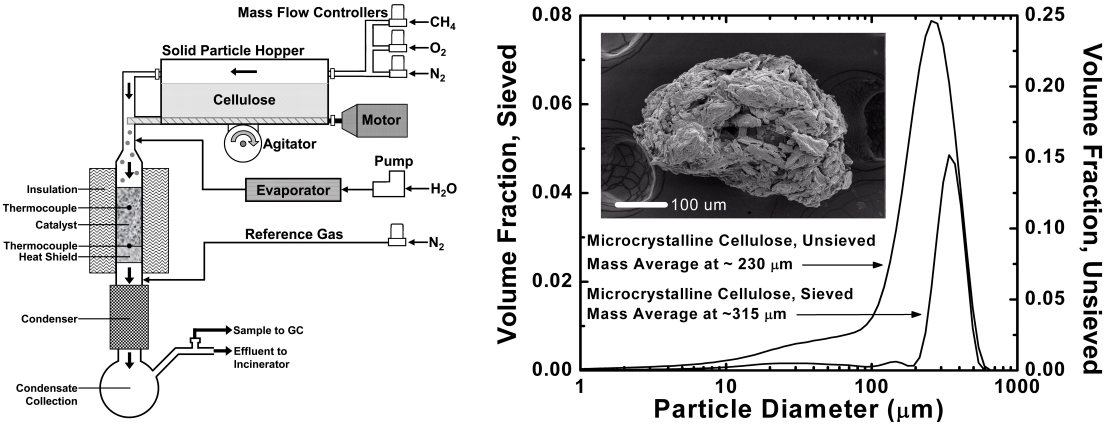

Figure 3.1: Left: the experimental apparatus consisted of an insulated quartz reactor tube supplied with N_2, O_2, CH_4, cellulose, or steam. Particles of cellulose were metered using a servo-motor powered auger passing through a sealed hopper. Reactor effluent gases passed through a condenser and were sampled for gas chromatography. Right: particle size distribution generated by light scattering of microcrystalline cellulose samples processed by reactive flash volatilization. Inlet micrograph shows a representative cellulose reactor feed particle with high porosity.

Cellulose was fed to the top of the reactor tube with a 0.25 in. auger, which was rotated by a small volume laboratory mixer to accuracies ±1 RPM. The auger functioned as a volumetric feeder, conveying cellulose from a gas-sealed acrylic hopper to the reactor. An unbalanced rotor vibrator was attached to the base of the hopper to ensure uniform and complete filling of the auger during operation, minimizing oscillation in fuel flow rates. Gases were fed through the hopper to the reactor using mass

flow controllers operated by LabVIEW software accurate to ±0.05 SLPM. Water was supplied by a syringe pump to a steam generator, where it was vaporized and fed ∼2 in. upstream of the catalyst bed via heated stainless steel tubing. Steam was fed in close proximity to the catalyst in order to avoid water condensation on the reactor walls and cellulose conglomeration prior to contact with the catalyst. The reactor effluent was directed through a laboratory condenser (maintained at 25 °C) to minimize throughput of condensible species, primarily water, to the sampling tube. Effluent was periodically sampled upstream of the condenser to verify the absence of condensible organic compounds.

3.2.2 Temperature Measurement

Experiments were primarily conducted with thermocouples placed at 10 mm and 30 mm from the front face of the catalyst bed. These thermocouples were inserted from the downstream side of the reactor tube during the placement of the foam monolith support. Axial temperature profile experiments were conducted using a reactor tube with 16 0.7 mm diameter holes placed in the quartz reactor tube along the length of the catalyst bed. Through these holes 16 K-type thermocouples were fed horizontally to the center of the catalyst bed as depicted in Fig. 3.5D. The quartz reactor tube was sealed using ultra high temperature ceramic adhesive. This apparatus facilitated the acquisition of steady state and transient reactor bed temperature profiles.

3.2.3 Reactor Operation

Reactor start-up involved pre-heating an isolated portion of the catalyst to ∼300 °C using an external heat source while passing methane and nitrogen gas through the reactor. Once hot, oxygen was added to the gas mixture at air stoichiometry and fuel-rich conditions necessary to avoid combustion. This procedure initiated the autothermal partial oxidation of methane in the catalyst bed, which heated the reactor bed to ∼900 °C. Cellulose was then added to the reactor at ∼30 g h^{-1}. Flow of methane was discontinued,

and the oxygen flow rate was adjusted to a fuel-rich regime for experimental trials.

The reactor was insulated to minimize heat loss to the surroundings. In order to accurately determine cellulose flow rate to the reactor, the system was initially operated at low C/O in order to heavily oxidize any carbon before being exhausted from the sphere bed. The effluent was then analyzed to quantify carbon content (i.e. the CO and CO_2 were measured with gas chromatography). Once a steady cellulose flow rate was observed, gases were adjusted to achieve the desired S/C, N_2/O_2, and C/O ratios, and the effluent was sampled. The system was then returned to a low C/O in order to verify that the cellulose flow rate had not changed. This procedure was used for determining the cellulose flow rate upon start-up, and for data obtained at operating conditions capable of producing condensible product species. The reactor was shut down by terminating cellulose, oxygen, and steam flows. Once the system was cooled, nitrogen flow was terminated.

All experiments performed without steam addition were operated at air stoichiometry ($N_2/O_2 = 3.76$). C/O is defined to be the molar ratio of carbon in the fuel to atomic oxygen fed as air. Complete cellulose combustion to CO_2 and H_2O therefore occurs at C/O=0.5. Experiments were carried out at C/O ratios of 0.6, 0.7, 0.8, and 0.9. These experiments were run in oxygen deficient environments in order to maximize selectivity to synthesis gas and hydrogen. Cellulose flow rates of 25-60 g h^{-1} were used for all data collection.

Steam addition experiments were performed by replacing nitrogen with steam in increments of 20% of the gaseous feed to maintain a constant gaseous co-feed flow rate. Gas feed compositions considered were (in mole percents): (1) 60% N_2, 21% O_2, 19% H_2O, (2) 40% N_2, 21% O_2, 39% H_2O, (3) 20% N_2, 21% O_2, 59% H_2O, and (4) 0% N_2, 21% O_2, 79% H_2O. S/C is defined to be the molar ratio of steam to carbon in the fuel. Experiments were run at C/O ranging from 0.6 to 0.9, depending on whether autothermal operation was sustainable.

3.2.4 Catalyst Preparation

All catalysts were prepared on Saint-Gobain NorPro Corporation 1.3 mm diameter α-Al_2O_3 spheres. The unmodified spheres have a surface area of 5.35 m^2 g^{-1} and a packing density of 64.1 lbs ft^{-3}. Prior to Rh-Ce deposition, a γ-Al_2O_3 washcoat was added to the spheres to increase surface area via incipient wetness technique.[33] A 5 wt% slurry of γ-Al_2O_3 in distilled water was added drop-wise to the spheres, which were then allowed to dry. Once dry, the spheres were calcined for 6 h at 600 °C. $Rh(NO_3)_3$ and $Ce(NO_3)_3{\cdot}6H_2O$ metal salts were then added to the spheres also using the incipient wetness technique. A 1 wt% Rh and 1 wt% Ce solution of metal salts in distilled water was added drop-wise to the spheres, which were then allowed to dry. Once dry, the spheres were calcined for 6 h at 600 °C. Catalysts were conditioned for ∼1 h under representative operating conditions before conducting experiments. Experiments were repeated on catalysts with no measurable differences in activity. Catalysts were generally used for no less than 10 h, during which there was no observable deactivation.

3.2.5 Feedstock Analysis

Microcrystalline cellulose used in all experiments was obtained from FMC BioPolymer. Samples of cellulose exposed to the air naturally absorbed ∼5 wt% moisture (S/C∼0.05). Moisture content was determined gravimetrically by drying in a vacuum oven. The particle size distribution in Fig. 3.1 was measured by light scattering. The raw cellulose sample was separated in a No. 50 mesh sieve to obtain a sample with fewer particles smaller than 200 μm to increase ease of handling by reducing particle conglomeration. Steam was produced from distilled water. The high purity gases, N_2 and O_2, were supplied separately with high pressure cylinders.

3.2.6 Product Analysis

Gas samples were sampled with a syringe downstream of the condenser, and injected into a gas chromatograph. The system was calibrated to measure permanent gases and higher hydrocarbon species. Species response factors and column retention times were determined using known concentrations of premixed gases. During standard operation the carbon, oxygen, and hydrogen mass balances typically closed to within ±5%.

Experiments were conducted several times, typically repeated on several identical catalysts, with no significant differences observed between experiments. Catalyst operating temperature and time ranged from 550-1100 °C and 10-30 h, respectively. Selectivity to product species was calculated on an atomic carbon basis, S_C(species), or an atomic hydrogen basis, S_H(species). The selectivity was defined as (atoms in the product species)/(atoms in the converted fuel). Co-fed steam was not considered fuel. The sum of all selectivities to product species based on the same element (C or H) should equal unity within experimental error. The residence time was calculated as the void volume of the catalyst bed divided by the volumetric flow of effluent gases at the exit temperature. Sphere beds exhibit smaller void fractions resulting in faster residence times than foams.

3.2.7 Equilibrium Calculations

Equilibrium calculations were performed by numerical minimization of Gibbs free energy using HSC Chemistry software.[46] Calculations were performed at 1 atm pressure and the temperature of the sphere bed 10 mm downstream of the front face (T_{10}). Back-face catalyst bed temperatures were not used due to significant temperature gradients, resulting from heat conduction to the monolith support. High (≥99%) conversion of fuel to C_1 products was expected at low S/C, facilitating the inclusion of the following species in the calculation: CO_2, CO, CH_4, O_2, H_2, H_2O.

The measured reactor process efficiency in Table 3.1 has been examined by calculating the fuel chemical flow availability (exergy), α_ι, of all non-cellulose species by eqn 3.1,

$$\alpha_i = (h_i - h_i^o) - T^o\,(s_i - s_i^o) + (\mu_i^o - \mu_i) \tag{3.1}$$

where h_i is the specific enthalpy of the species i, T is the temperature, s_i is the specific entropy of species i, and μ_i is the chemical potential of species i.[47] The values of h_i^o, s_i^o, and μ_i^o were calculated at the restricted dead state defined as T^o=298 K, P^o=1 atm, and the gaseous molar fractions X(O_2)=0.20, X(N_2)=0.76, X(H_2O)=0.03, and X(other)=0.01. The chemical availability of cellulose was calculated using a correlation developed by Szargut and Styrylska,

$$\beta = \frac{1.0438 + 0.1882\left(\frac{H}{C}\right) - 0.2509\left(\frac{O}{C}\right)\left(1 + 0.7256\frac{H}{C}\right)}{1 - 0.3035\frac{O}{C}} \tag{3.2}$$

where H, C, and O represent atomic mass fractions of feedstock cellulose, and β relates the chemical availability of cellulose, α_{cell}, to the lower heating value (LHV) of cellulose by α_{cell} = β*LHV(cellulose).[48] The lower heating value of cellulose, obtained from a correlation assuming C/H/O=6/10/5, was 15.7 kJ g^{-1}.[49] Process efficiency in Table 3.1 is defined as the flow availability of all products divided by the flow availability of all feed species.

3.3 Results and Discussion

The results demonstrate that reforming of cellulose with steam addition can produce equilibrium selectivity to synthesis gas with very little selectivity to minor products. By this method, the effluent syngas stoichiometry is tunable by adjusting the S/C ratio. Sustainable processing to a clean product stream maintains a significant fraction of the cellulose fuel value without observable formation of a solid carbon byproduct.

Table 3.1: Selected experimental data for the millisecond reforming of microcrystalline cellulose[a]

Experiment	1	2	3	4	5
Catalyst bed length/mm	30	30	30	30	60
C/O ratio	0.9	0.9	0.8	0.8	0.9
H_2O substitution for N_2	0	19	39	59	79
S/C ratio	0.05	0.55	1.21	1.81	2.14
N_2/O_2 ratio	3.76	2.86	1.91	0.95	0
Mass flow/g h^{-1}	30	30	30	30	60
Residence time/ms	33	31	24	25	29
Space velocity/mol h^{-1} L^{-1}	118	118	118	118	118
Mass velocity/h^{-1}	53	53	53	53	53
H selectivity/%					
H_2	48	63	58	71	79
H_2O	38	34	42	21	21
C selectivity/%					
CO	38	35	32	25	27
CO_2	60	64	68	72	72
CH_4	1.9	1.2	0.3	3	0.2
Temperature at 30 mm/°C	600	730	710	625	825
H_2/CO	1.1	1.4	1.5	3.0	2.3
Syngas dry mole fraction/%	18	24	22	25	42
Process efficiency/%	58	66	63	68	73

[a]All experiments were considered on a bed of 1.3 mm α-Al_2O_3 spheres with 5 wt% γ-Al_2O_3 washcoat and 2 wt% loading of Rh and Ce with >99% conversion of cellulose to C_1 products. The space velocity was defined as (molar flow of carbon)/(volume occupied by the catalytic spheres). The mass velocity was defined as the (mass flow of carbon)/(mass of RhCe). The process efficiency was defined in the experimental section of the text.

3.3.1 Thermodynamic Considerations

Fig. 3.2 shows representative equilibrium selectivity output data for the reaction of cellulose ($C_6H_{10}O_5$) with steam and oxygen at variable C/O and S/C. As the reaction feed becomes more carbon rich (increasing C/O), the selectivity to more oxygen deficient species such as $S_H(H_2)$ and $S_C(CO)$ increase. Additionally, as the reaction feed contains more steam (higher S/C), the selectivity to hydrogen, $S_H(H_2)$, increases and $S_C(CO)$ decreases. This behavior can be described very generally by an increased reaction of CO with steam to form hydrogen by the water-gas-shift reaction (WGS) (eqn 3.3) at higher S/C.

$$WGS : CO + H_2O \leftrightarrow CO_2 + H_2,\ \Delta H^\circ = -41\ kJ\ mol^{-1} \tag{3.3}$$

The gaseous products predicted in Fig. 3.2 are achievable, provided a chemical route exists to equilibrium. The formation of a second, solid phase of carbon, C_S, has the potential to develop on catalytic surfaces, blocking surface chemistry and preventing the reactor from operating sustainably. This inhibition can likely be eliminated if solid carbon or carbon-rich solid residue is not a favored thermodynamic product. The prediction of a solid carbon equilibrium product (C_S) is a function of the reaction feed stoichiometry (cellulose/oxygen/steam) and the reaction temperature. By calculating the stoichiometry for a set of temperatures (500, 700, and 900 °C) for which the activity of C_S goes to one, it is possible to define a boundary between a region for which C_S is unstable and not predicted by equilibrium. As shown in the ternary diagram of Fig. 3.3, this "no carbon" region is defined by a boundary (dashed lines) for which an increase in process temperature expands the operable "no carbon region" to nearly half of the possible reaction stoichiometry.[50, 51]

The relevance of this calculation to the processing of feedstocks can be determined by placing the internal atomic stoichiometry (*i.e.* cellulose: C/H/O$\sim$28.6/47.6/23.8 mol%) of each material on the ternary diagram (points). All considered feedstocks exist within the region for which solid carbon is a predicted thermodynamic product at T<900 °C.

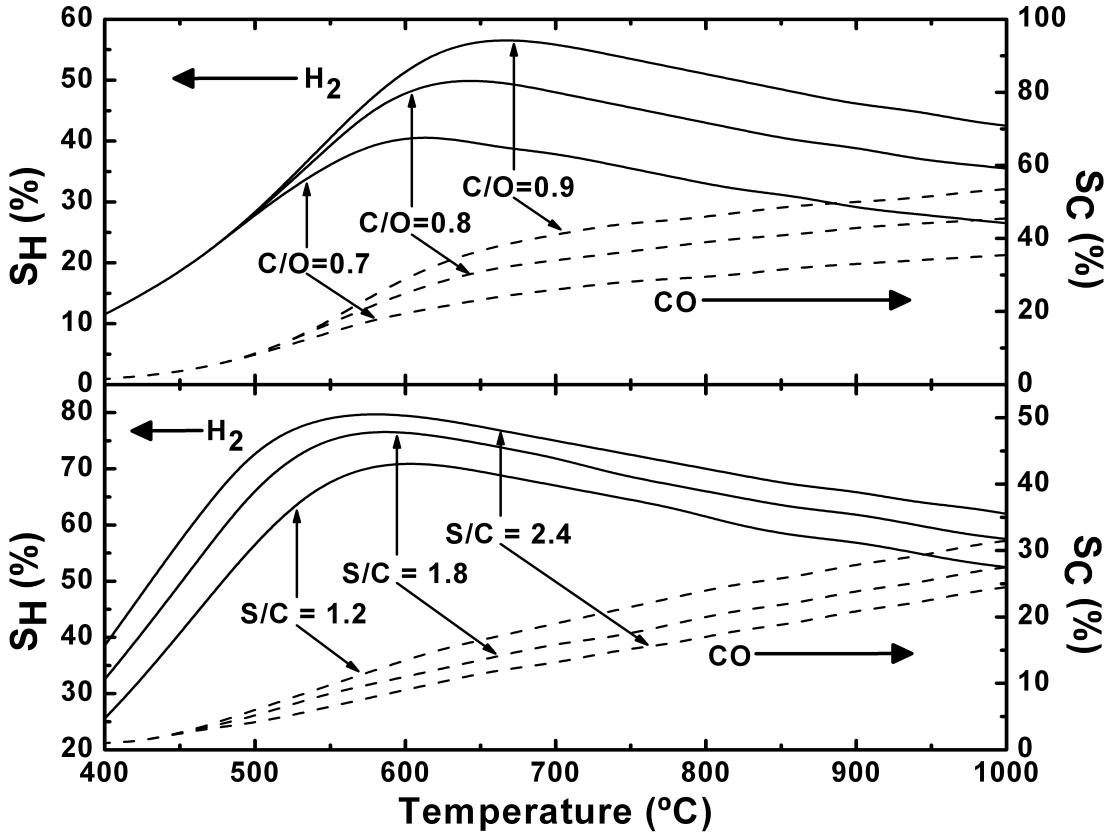

Figure 3.2: The conversion of cellulose $(C_6H_{10}O_5)_n$ to equilibrium products by dry oxidation (upper panel) at C/O=0.7, 0.8 and 0.9, and steam reforming at C/O=0.8 (lower panel) at S/C=1.2, 1.8 and 2.4, predicts 40-80% selectivity to H_2 (solid lines) and 0-50% selectivity to CO (dashed lines for the temperature range 400-1000 °C. C/O is defined as molar feed rate of carbon in the fuel relative to molar feed rate of oxygen atoms in the gaseous O_2. S/C is defined as molar feed rate of steam relatvie to molar feed rate of carbon in the fuel.

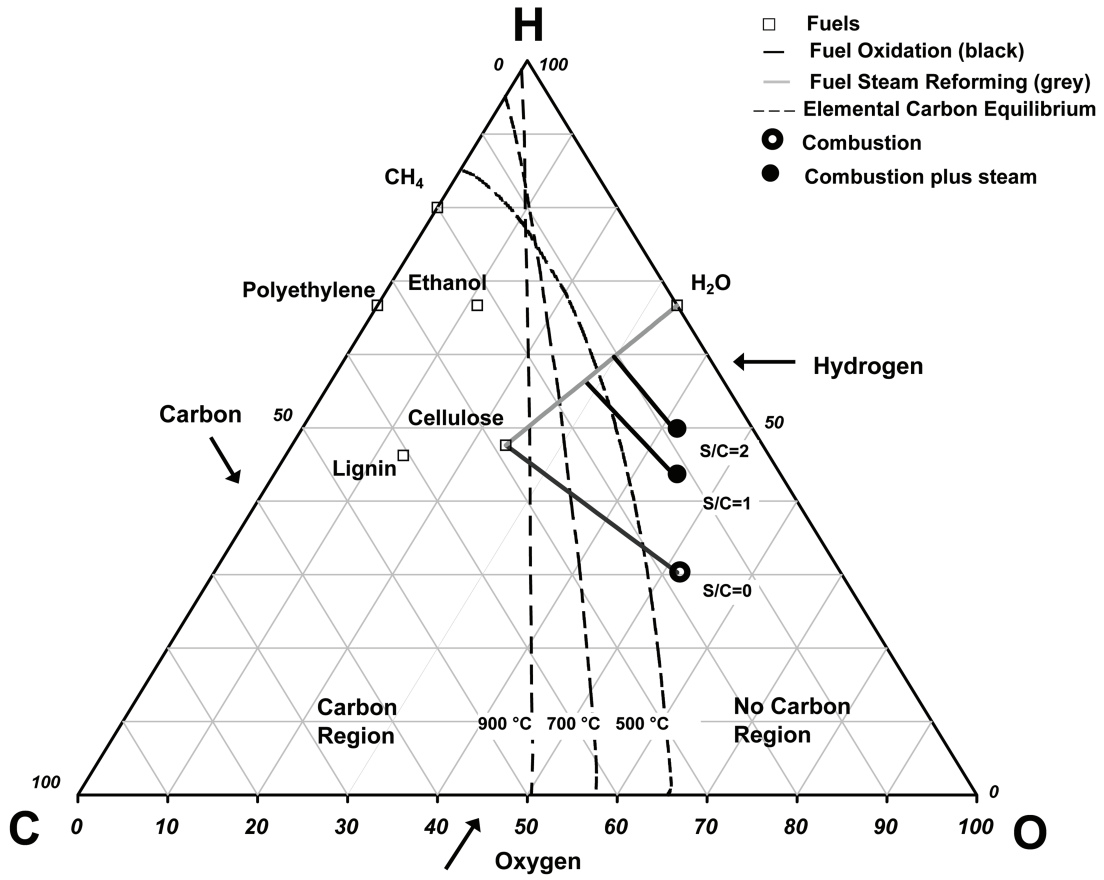

Figure 3.3: The formation of solid carbon, C_S, by processing of solid, organic feedstocks such as cellulose, lignin, polyethylene, or ethanol inhibits the use of catalysts due to surface poisoning. Dashed lines represent the interface between the region for which C_S is predicted as a thermodynamic product, and the region for which it is not, at 500, 700, and 900 °C. The stoichiometry of steam reforming (solid grey line) cellulose oxidation and autothermal steam reforming (solids black lines) demonstrate that conversion to combustion products or synthesis gas occurs near the interface of these two regions permitting autothermal carbon-free processing.

However, the addition of oxygen (solid black line) shifts the overall atomic stoichiometry across temperature boundaries such that no carbon is predicted at combustion stoichiometry (○). Processing at oxygen-deficient (syngas-producing) conditions occurs along the cellulose oxidation line and at lower adiabatic temperatures than combustion. The key implication for autothermal reforming is that there exists a specific oxidation feed stoichiometry around C/O=1.1 (C/O calculated as defined in the experimental section) for the considered reaction conditions for which carbon becomes a predicted product. The addition of steam provides a processing alternative (solid grey line) to extend the overall stoichiometry across the thermodynamic boundaries. By co-feeding steam with oxygen at S/C=1.0, nearly the entire oxidation stoichiometry exists within the no carbon region defined at 500 °C, and higher S/C offer an even more expansive range of feed stoichiometry.

3.3.2 Autothermal Catalytic Partial Oxidation of Cellulose

The production of gaseous products from the autothermal reforming of cellulose at S/C=0.05 (due to particle moisture) is described in panels A and B of Fig. 3.4. Steady operation was observed at all experimental conditions without oxygen breakthrough, and transient behavior due to a change in experimental operating conditions was resolved in 12 min. Carbon conversion to C_1 products is >99% for all C/O presented, and carbon selectivity to methane was <3% for all C/O. Selectivity to H_2 ranges from a minimum of 14% at C/O=0.6, to a maximum of 47% at C/O=0.9. The majority of the remaining hydrogen atoms were converted to water. Selectivity to carbon monoxide ranges from a minimum of 21% at C/O=0.6, to a maximum of 38% at C/O=0.9. The majority of the remaining carbon atoms were converted to CO_2. For C/O<1.0 at S/C=0.05, experimentally measured selectivity to gaseous products achieved equilibrium within experimental error. Complete conversion was attainable at residence times less than 40 ms.

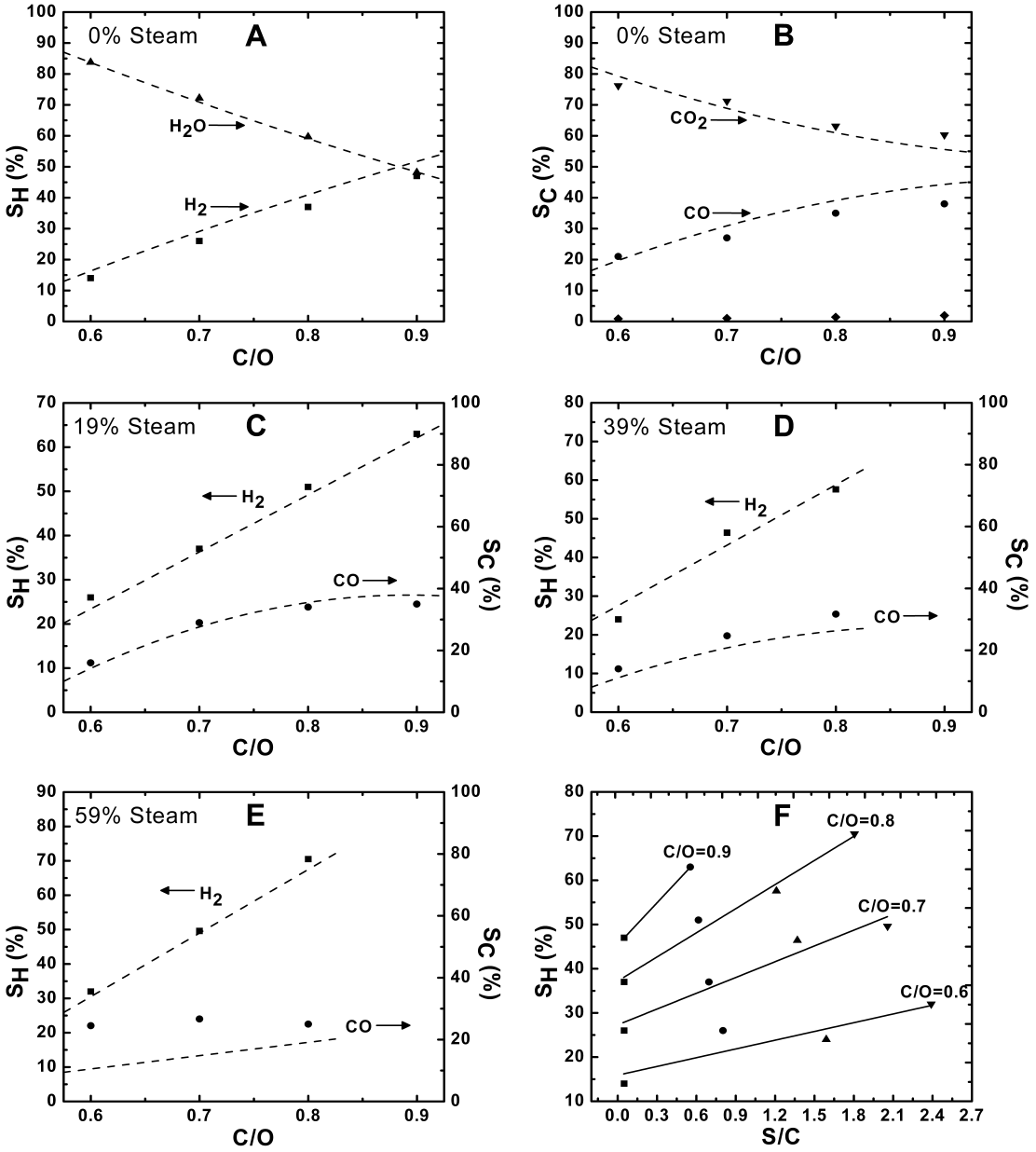

Figure 3.4: The selectivity to hydrogen (■), water (▲), carbon monoxide (●), carbon dioxide (▼) and methane (♦) achieves equilibrium in the reforming of cellulose at a flow rate of 30 g hr^{-1} with gaseous co-feed: (79% N_2 + 21% O_2) in Panels A and B, co-feed (60% N_2 + 21% O_2 + 19% H_2O) in Panel C, co-feed (40% N_2 + 21% O_2 + 39% H_2O) in Panel D, co-feed (20% N_2 + 21% O_2 + 59% H_2O) in Panel E, and at $0 \leq S/C \leq 2.4$ in Panel F. Dashed lines represent equilibrium concentrations and solid lines are fitted.

At C/O=1.0, production of organic species larger than C_1 was observed in the chromatogram. The incomplete decomposition to equilibrium products can be attributed to slower kinetics, resulting from the decreased temperature at C/O=1.0. For all C/O, the coldest part of the catalyst bed (T_{30}) never dropped below 500 °C. The experimentally measured temperatures are shown in Fig. 3.5, and will be discussed in the next section. Overall performance with alumina spheres as a support for the Rh-Ce catalyst was very similar to that of 80 ppi alumina foams.[30]

Panels C through E of Fig. 3.4 show selectivity to hydrogen and carbon monoxide as a function of C/O for the CPO of cellulose at varying concentrations of N_2, O_2, and H_2O feed gases. Steady operation was observed at all experimental conditions without oxygen breakthrough, and transient behavior due to a change in experimental operating conditions was resolved in 12 min. Carbon conversion to C_1 products is >99% for all C/O presented. Additionally, average methane selectivity with respect to carbon was <3% for all C/O. In panel C, 19% molar substitution of nitrogen with steam raised the selectivity to H_2 to 63% while lowering selectivity to CO to 35% at C/O=0.9. When the substitution for nitrogen with steam was raised to 39% in panel D, the overall operating temperature decreased (shown in Fig. 3.5), and the C_2 organic species were observed at C/O=0.90. However, at C/O=0.8, selectivity to H_2 was 58% and selectivity to CO was 32%. Further substitution of steam for nitrogen to 59% H_2O gaseous feed further cooled the operating temperature of the reactor (Fig. 3.5), but the addition of steam raised the observed selectivity of H_2 to 71% and lowered the selectivity to CO to 25% at C/O=0.8. Panel F of Fig. 3.4 relates the observed species to the operating S/C ratio for each of the experimental trials.

3.3.3 Spatial Temperature Profiles

Measurements of the temperature within the fixed bed of catalyst spheres provide experimental insight to support the proposed mechanism detailed in the next section. By inserting thermocouples radially into the fixed bed of catalyst as shown in panel D of

Fig. 3.5, the temperature at which reforming chemistry is occurring is known with millimeter resolution. Panels A, B, and C describe the effect of cellulose flowrate, process C/O ratio, and magnitude of steam substitution for nitrogen, respectively.

Panel A of Fig. 3.5 shows that the spatial temperature profile is a very strong function of the flow rate of cellulose. Both flow rates, 25 g h^{-1} and 40 g h^{-1}, exhibit a rise in temperature between the top of the catalyst bed (0 mm) and the maximum temperature (∼5 mm). However, the magnitude of the temperature increase appears to be a function of the total flow rate with higher feedstock flow rates exhibiting higher thermal gradients within the oxidation zone. This can be partially explained by an increased distance between the endothermic chemistry at the catalyst front face and exothermic chemistry taking place in the oxidation zone. In contrast, both flow rates of cellulose exhibit the same rate of temperature decline after the temperature maximum (∼5-30 mm). The difference in exit temperature (T_{30}) for differing flow rates can be attributed to heat loss from the reactor.

Panel B of Fig. 3.5 details the effect of C/O ratio on the spatial temperature profile for a cellulose feed rate of 25 g h^{-1} at S/C=0. More oxygen feed (lower C/O) exhibits an overall hotter profile due to more overall exothermic chemistry. Panel C of Fig. 3.5 shows the effect of substituting steam for nitrogen at 0 mol%, 19 mol%, 39 mol%, and 59 mol% on the spatial temperature profile for a cellulose feed rate of 40 g h^{-1} and C/O=0.7. The initial substitution (0→19 mol%) has the effect of slightly raising the temperature from ∼5-30 mm likely due to the temperature of steam (100 °C). However, further substitution (19→39 mol%, and 39→59 mol%) monotonically decreases the overall temperature profile 10-15 °C. A likely explanation is the increased heat capacity of steam over nitrogen.

3.3.4 Process Chemistry

The process by which solid particles of cellulose ∼315 μm in average diameter are reduced to C_1 products (Fig. 3.6) at millisecond time scales must account for particle

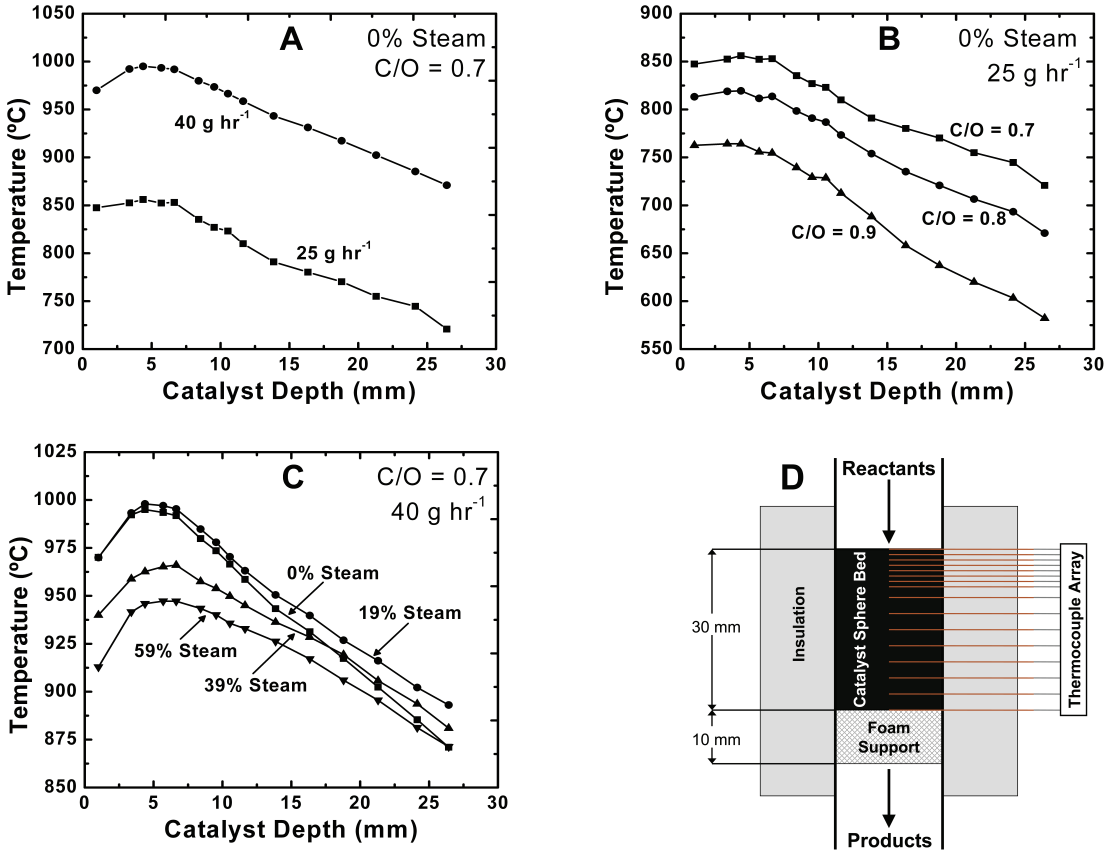

Figure 3.5: Measured axial temperature profile within the 30 mm fixed bed of Rh-Ce/γ-Al_2O_3 spheres was examined as a function of total solid cellulose particle flow rate (A), C/O ratio (B), and magnitude of steam substitution for nitrogen (C). In Panel A, the temperature profile was measured with C/O=0.7, S/C=0.05, and at cellulose flow rates of 25 g hr^{-1} (▼) and 40 g hr^{-1} (●). In Panel B, the temperature profile was measured at S/C=0.05, cellulose flow rate of 25 g hr^{-1}, and C/O=0.7 (■), C/O=0.8 (●), and C/O=0.9 (▲). In Panel C, the temperature profile was measured at a cellulose flow rate of 40 g hr^{-1}, C/O=0.7, and steam substitution of N_2 with steam in the gaseous feed of 0 mol% (■), 19 mol% (●), 39 mol% (▲), and 59 mol% (▼). The temperature at each axial position (catalyst depth) was measured simultaneously by inserting and sealing multiple thermocouples radially into the reactor (D).

volatilization in the presence of oxygen integrated with the catalytic partial oxidation of volatilized products on a noble metal surface. Each process (particle volatilization or catalytic reforming) consists of complex multi-phase chemical mechanisms and multiple modes of heat transfer for which the current understanding by computer modeling does not even extend to the individual process.[52, 53] The chemical and heat integration of the two processes expands the complexity of the overall reaction such that mechanistic observations are currently only available through effluent data and experiments considering more simple fuel species.

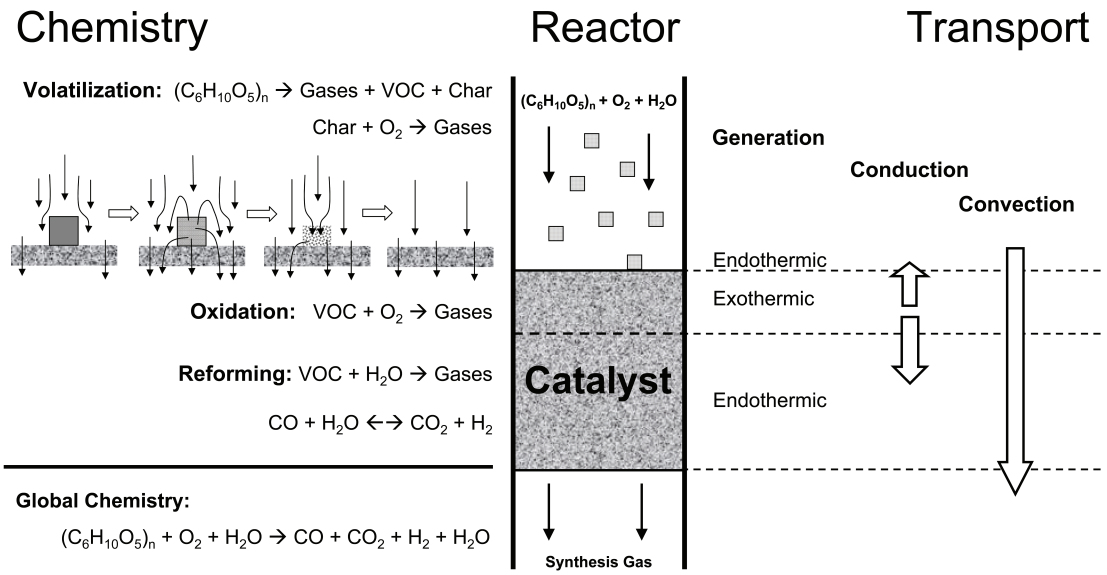

Figure 3.6: The proposed chemical and thermal integration of millisecond particle reforming on a fixed bed of noble metal catalyst permits rapid conversion of organic solid materials to synthesis gas. Particles undergo rapid endothermic volatilization upon impact with a hot, catalytic surface, producing gases (*e.g.* H_2 and CO) and volatile organic compounds (VOCs). Volatile species flow into the catalyst and produce gases by exothermic surface and gaseous oxidation chemistry. Thermal energy generated in the oxidation zone conducts upward to the volatilization zone, and down to the reforming zone where remaining VOCs and gases undergo steam reforming and water-gas-shift to achieve equilibrium selectivity to synthesis gas.

The impact of the cellulosic particle with the hot catalytic surface likely initiates

the process chemistry. The extent of particle conversion occurring within the gaseous region 3-10 mm above the catalytic bed is likely limited, because previous examination has measured the gas-phase temperature of this region less than 300 °C severely limiting particle conversion by pyrolysis.[30, 54] Fig. 3.5B shows that T=700-800 °C for C/O=0.9 at the leading edge of the catalyst, providing sufficient conductive heat transfer from catalyst support to particle for volatilization.

Particle volatilization is likely a complex convolution of heat transfer and reaction chemistry. Complete particle conversion must account for at least (1) the drying of the particle (∼5 wt% moisture), (2) cellulose pyrolysis to gases (*e.g.* CO, H_2), volatile organics, and chars, (3) volatile organic cracking to gases, and (4) oxidation of gases, volatile organics, and chars. Multiple cellulose pyrolysis lumped kinetic models exhibit some form of competitive pathways to either gases (*e.g.* H_2O) and char, volatile organics (*e.g.* acetic acid, methanol), or just gases.[55, 56, 57, 58, 59] Fluidized bed fast pyrolysis reactors maximize selectivity (∼70 wt%) to volatile organics around 500 °C for ∼1.2 s with millimeter sized particles.[1] Lower temperatures favor char production, while higher temperatures exhibit higher selectivity to gases with the lower kinetic limit for char production of ∼3 wt% at 700-800 °C.[60]

The application of cellulose pyrolysis kinetics to spherical geometry to account for heat and mass transport has considered particle degradation in an inert atmosphere extensively.[61, 62, 63] Under optimal fast pyrolysis conditions, organic particles as large as 1 mm usually exhibit heat transport control, while particles with diameters less than ∼200 μm exhibit chemical kinetic control.[61] The experiment considered here examines a related situation of direct impingement of a ∼315 μm particle with a hot surface. One-dimensional transport/kinetic models considering solid cellulose rods contacting isothermal hot surfaces has shown superior selectivity to volatile organics due to higher particle heating rates.[60] In an inert atmosphere with solid surface temperatures of 700-800 °C, models predict cellulose pyrolysis of particles on the order of millimeters to exhibit selectivity to volatile organics as high as ∼90 wt% and char less than 5 wt%.[64]

The applicability of these simulations to the particle volatilization of the considered experiment depends greatly on the magnitude of oxidation chemistry occurring within the particle by interaction with the gaseous feed. The considered microcrystalline cellulose, depicted in Fig. 3.1, exhibits high porosity permitting an initial internal supply of oxygen. However, the evolution of gases and volatile organics that must be transported to the particle surface due to a difference in density must significantly hinder diffusion of oxygen into the particle. Alternatively, the oxidation of evolved species at the particle surface can only be elucidated through the consideration of a flow boundary layer as has been considered for particle combustion in a methane flame.[52]

Evolved species from the solid particle likely mix with the bulk gas ($O_2 + N_2 + H_2O$) and flow into the fixed catalyst bed of RhCe/γ-Al_2O_3/α-Al_2O_3 spheres. Likely devolatilized species include the same species observed in bio-oil samples that are derived from carbohydrate pyrolysis such as methanol, hydroxyacetaldehyde, acetic acid, or several furan-based compounds.[65] Highly oxygenated species such as polyols (ethylene glycol and glyercol) have exhibited continuous, steady-state processing to synthesis gas with high conversion (>99%) and equilibrium selectivity to synthesis gas.[28] Similar behavior has also been observed from the reforming of other species classes including esters and acids, ethers, and sugars.[29, 66, 67] However, the role of competition existing within mixtures for surface chemistry is unknown, and limited research exists examining the catalytic partial oxidation of mixtures of organics.[68]

The conversion of oxygenated species by catalytic partial oxidation is likely to occur by the general mechanism observed with methane reforming. Internal species measurements of methane have shown that conversion of fuel occurs in two distinct zones: oxidation and reforming.[69] In the oxidation zone, volatile fuel species premixed with bulk gases enter the fixed bed of catalyst spheres at high velocity and undergo exothermic surface oxidation chemistry. Greater than 99% of oxygen is consumed (by definition) within this region likely producing a significant fraction of the thermodynamic species (H_2, H_2O, CO, and CO_2) by surface chemistry. At low C/O ratios (more oxygen rich),

the oxidation zone converts a large fraction of the fuel.

At higher C/O, a more significant fraction of fuel passes through the oxidation zone to the reforming zone. Endothermic surface chemistry between fuel and oxidation products such as H_2O (steam reforming) or CO_2 (dry reforming) provide chemical routes to equilibrium. Additionally, the gas temperature is sufficiently high to permit endothermic cracking of fuel to smaller fuel species. Both of these chemistries are likely occurring simultaneously, effectively lowering both the surface and gas phase temperature as shown in Fig. 3.5. The performance of the reforming zone ultimately determines the conversion of volatile fuel species. By selecting a sphere bed (small pores) with a γ-Al_2O_3 washcoat, the reactor is tuned in favor of the surface chemistries to the desired C_1 species. For high conversion of fuel, this zone must remain sufficiently hot to permit chemistries at millisecond time-scales. As C/O increases, less thermal energy is generated in the oxidation zone, and the endothermic chemistry of the reforming zone critically cools denying complete conversion of volatile organics. By this mechanism, volatile organics are initially produced at C/O>1.0 for fuel flow rates of 25-40 g h^{-1} on the considered fixed bed catalytic reactor (L=30 mm).

3.3.5 Process Limitations

The combination of solid conversion chemistry with the autothermal reforming of gaseous compounds introduces a greater number of process variables and prevents a clear definition of the limits of the process. If the objective of the process is steady long-term reforming to synthesis gas, then selected sets of process parameters which result in either incomplete conversion to C_1 products, catalyst deactivation, or upstream combustion of particles are outside of the domain of sustainable parameters. The incomplete conversion of cellulose to C1 was observed when the temperature 30 mm into the catalyst bed was at or below about 500 °C. Table 3.1 (Experiments 1-4) lists a set of performance specifications that permit operation relatively close to this requirement. Catalyst deactivation can occur if the maximum in temperature observed at ∼5 mm within the

catalyst bed exceeds ∼1200 °C, permitting conversion of γ-Al_2O_3 to α-Al_2O_3 or sintering of Rh. This high temperature is accessible at any flow rate (25-60 g h^{-1}) provided the C/O is low enough to generate sufficient heat. The third major process restriction is the ignition of solid particles above the catalyst which can propagate up the feed stream in an unsafe, unsustainable manner. The minimum ignition temperature of small (1 μm-1 mm) organic particles is a function of at least particle size and concentration, with smaller particles igniting at lower temperatures.[70] The precise characteristics describing the ignition of particles approaching a hot surface are unknown. However, we have demonstrated that sets of process parameters exist for which processing can occur without dilution with N_2 on particles as small as 300 μm.

3.3.6 Process Performance

Using the knowledge gained from the experiments described in Fig. 3.4 and 3.5, experimental trials were executed to demonstrate the conversion of solid cellulose to an optimal synthesis gas stream. By selecting a fixed sphere-bed catalyst 6 cm in length and a process flow rate of 60 g h^{-1} at a C/O=0.9 with steam addition of S/C=2.14 and 0% nitrogen addition, it was possible to completely convert cellulose to a synthesis gas rich stream with a synthesis gas ratio of H_2/CO=2.3 comprising a dry mole fraction of 42%. Under these conditions the reactor exhibited steady autothermal reforming with no oxygen breakthrough at a gaseous residence time less than 30 ms. Additionally, ∼80% of the atomic hydrogen provided by the feedstock cellulose was converted to molecular H_2.

Analysis of the conversion from a solid fuel to a gaseous fuel must account for the loss in fuel value. Using the method described in the experimental section, the maximum theoretical work that could be achieved from the feedstock cellulose (availability) was ∼18 MJ kg^{-1}. By millisecond reforming, nearly 75% of this potential was maintained as the gaseous effluent in the optimal experiment (trial 5 of Table 3.1). Most of the retained fuel availability existed within the synthesis gas (75-80%) with the remaining

fraction occurring with the high temperature (600-800 °C) steam, carbon dioxide or nitrogen. The loss in ∼25% of the fuel value of cellulose can be attributed process irreversibilities such as the generation of a large number of moles from cellulose. The primary benefit offsetting the one quarter loss in fuel value is an improvement in ease of fuel handling. Relative to gases, the transportation of solids within a chemical process remains a demanding, energy intensive technique requiring significant maintenance.

Comparison of the autothermal steam reforming of cellulose with other catalytic gasification techniques will ultimately determine the benefit of small, fast chemistry. While a complete process design and economic analysis is ultimately the best technique for determining the optimal process, an analysis of the operation of the gasification reactor provides an alternative metric that can be realistically assessed within this report. Fig. 3.7 details the performance of four different biomass gasification reactors containing multiple catalysts with the goal of relating the rate of biomass processing to both the size of the reactor and the use (mass) of the catalyst. The carbon space velocity has been defined as the ratio of the molar flow rate of biomass carbon to the volume necessary for reaction chemistry. By this definition, higher carbon space velocities result in smaller reactors. The carbon mass velocity has been defined as the ratio of the mass flow of biomass carbon to the mass of catalyst such that higher mass velocities result in lower use of catalyst. Full details of all data points and calculations are located in Appendix B.

As shown in Fig. 3.7, the existing technology for the BTL process of fluidized (circulating and bubbling) bed gasifiers with downstream gas cleaning in fixed bed catalytic reactors exhibit carbon space velocities of ∼0.5-8.0 mol L^{-1} h^{-1} and carbon mass velocities of ∼0.8-9.0 h^{-1}. By applying catalysts directly to the fluidized bed, the use of catalyst (mass velocity) remains about the same, but the volume can be reduced as the space velocity increases to 8.0-30 mol L^{-1} h^{-1}. An alternative process to produce synthesis gas produces volatile organics (bio-oil) in fluidized bed reactors which can be steam reformed to synthesis gas. Because this process still uses a fluidized bed, the

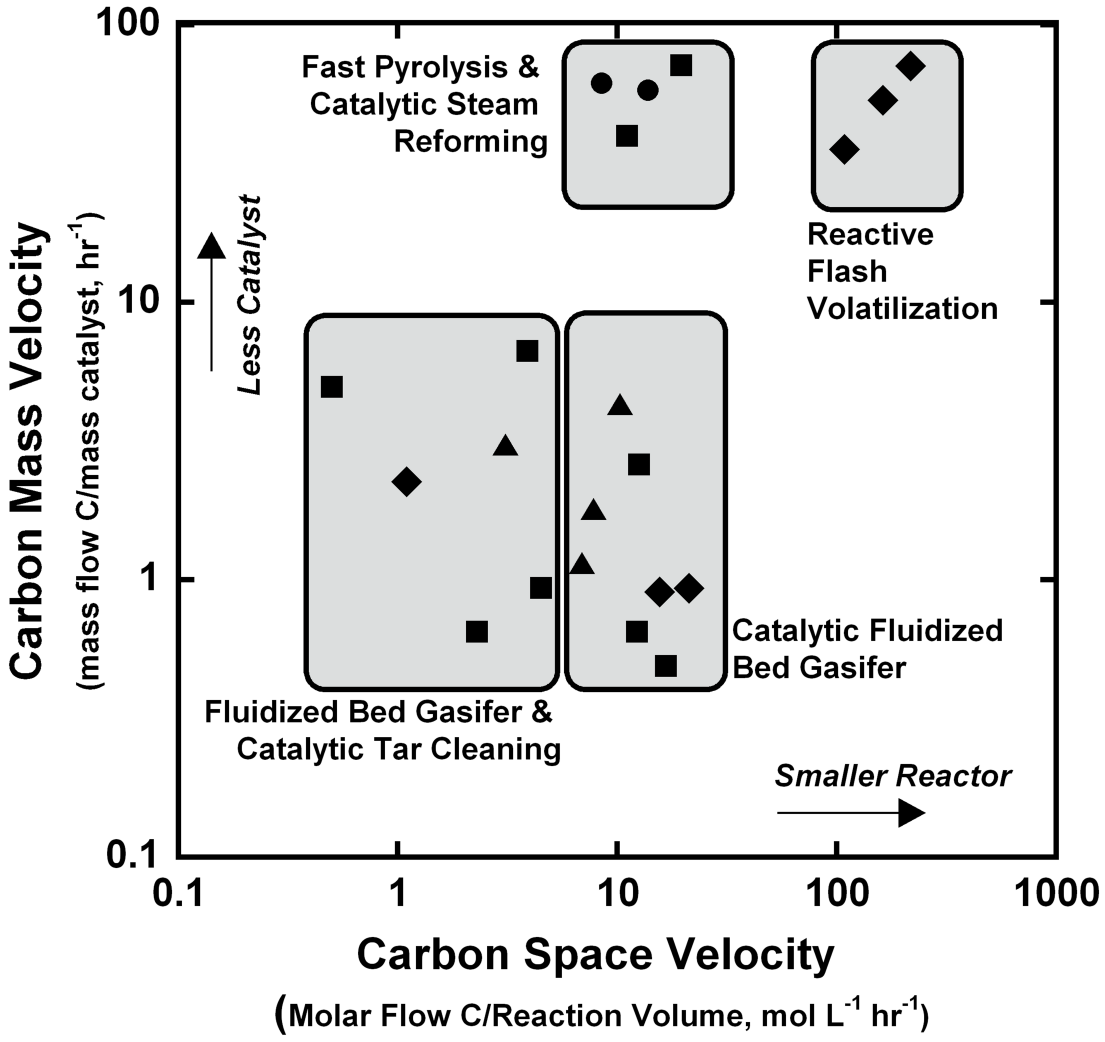

Figure 3.7: Various processes to convert organic solids to synthesis gas exhibit operational performance grouped by process type despite utilizing several different catalysts: dolomite (▲), Ni (■), Rh (⧫), Ru (•). The carbon space velocity provides a measure of the reactor volume by relating the molar processing of carbon to the volume necessary for chemical conversion. The carbon mass velocity provides a measure of catalyst usage by relating the molar processing of carbon to the mass of the catalyst. Complete details and references are located in Appendix B.

space velocity remains in the 8.0-30 mol L^{-1} h^{-1} range, but the high throughput of bio-oil steam reformers has permitted very high utilization of the Ni and Ru catalysts corresponding to high mass velocities in the range of 50-80 h^{-1}. Millisecond reactors further improve the carbon space velocity to 100-300 mol L^{-1} h^{-1} by carrying out the solid conversion to reformable species directly on the reforming catalyst. In general, millisecond reactors are at least an order of magnitude smaller and use less catalyst than most conventional catalytic gasification schemes.

3.4 Conclusions

We show that three sets of chemistries necessary for the biomass-to-liquids process (volatilization of cellulose, tar-cleaning of organic compounds, and the water-gas-shift of the gaseous effluent) can be integrated into one continuous flow catalytic reactor by reactive flash volatilization. Complete conversion of microcrystalline cellulose particles ($\sim$300 μm) to only C_1 products can occur faster than 30 milliseconds with the use of Rh-Ce/γ-Al_2O_3 catalysts over a wide range of S/C, C/O, and N_2/O_2. Steady, autothermal reforming without the presence of a diluent such as N_2 produces a more synthesis gas rich effluent. Additionally, the effluent synthesis gas ratio is tunable ($1.0<H_2/CO<3.0$) by manipulating the S/C of the reactor feed. The process appears to occur by the thermal integration of endothermic particle volatilization driven by heat conducted from an exothermic oxidation zone within the catalyst bed. Sufficient heat transfer from the oxidation zone to the entire fixed catalytic bed is thought to maintain the temperature above that at which coke is predicted by equilibrium. By this method, optimal processing conditions permit conversion such that $\sim$75% of the fuel value of the cellulose is maintained in the synthesis gas effluent.

3.5 Acknowledgements

This work was supported by the U.S. Department of Energy (DOE), Office of Basic Energy Sciences and the Initiative for Renewable Energy (IREE) at the University of Minnesota - Twin Cities.

Chapter 4

Improved Utilization of Biomass-Derived Carbon by Co-Processing with Hydrogen-Rich feedstocks in Millisecond Reactors[1]

No commercial process capable of converting biomass into useful fuels and chemicals without significant carbon losses to char or CO_2 exists presently because of process or thermodynamic constraints.[1, 2]. This chapter focuses on the development of a reactor capable of improving the utilization of biomass-derived carbon during thermochemical conversion to synthesis gas. By co-processing hydrogen-deficient biomass (H/C$\sim$2) with hydrogen-rich feedstocks (H/C$\geq$4) through catalytic partial oxidation over Rh based

[1] **Parts of this chapter appear in: J.L. Colby, P.J. Dauenhauer, Brian C. Michael, Aditya Bhan and L.D. Schmidt, "Improved utilization of biomass-derived carbon by co-processing with hydrogen-rich feedstocks in millisecond reactors," *Green Chemistry*, 2010, 12, 378-380 - Reproduced by permission of The Royal Society of Chemistry (RSC).**

catalysts, 100% of the fuel carbon atoms fed to the reactor can be converted to CO.

4.1 Introduction

Liquid hydrocarbons are appealing for their high energy density and ease of storage. Collectively, these characteristics are unique to carbon-rich liquid fuels produced almost entirely from petroleum. Biomass, the only source of renewable carbon, represents the only sustainable feedstock for the production of carbon-rich fuels.[7] It will, therefore, become important to develop processes that effectively utilize all of the biomass-derived carbon. No commercial process capable of converting biomass into useful fuels and chemicals without significant carbon losses to char or CO_2 exists presently because of process or thermodynamic constraints.[1, 2]

Thermochemical conversion of biomass to synthesis gas, a mixture of H_2 and CO, is a route for the production of synthetic carbon-rich liquid fuels. Gasification of biomass by partial oxidation, used commercially to make synthesis gas, produces some combustion products in an overall exothermic, char-free reaction,

$$(CH_2O)_n + mO_2 \rightarrow wH_2 + xCO + yH_2O + zCO_2 \tag{4.1}$$

With existing technology only ∼50% of biomass carbon is converted to carbon monoxide, and the remainder is emitted as CO_2.[12] Ideally, gasification would convert 100% of the carbon in biomass to CO, eliminating the generation of CO_2.

Carbon monoxide yields can be improved by co-feeding carbon dioxide with biomass and oxygen. The addition of CO_2 favors reverse water-gas-shift (RWGS), increasing CO production at the expense of molecular hydrogen,

$$H_2 + CO_2 \leftrightarrow H_2O + CO \tag{4.2}$$

However, CO_2 addition under typical biomass gasification conditions does not provide the thermodynamic driving force necessary to convert all biomass-derived carbon to CO.

To overcome this thermodynamic limitation hydrogen must be co-fed to the reaction, supplying energy needed to drive the RWGS reaction, as discussed in greater detail by Xiaoding et al.[71]

The addition of molecular hydrogen to traditional biomass processes has been considered for improving product quality and yield by improving carbon utilization and increasing product H_2/CO ratios.[72, 73, 74] It has also been considered as a method for mitigating CO_2 emissions by chemical reduction, rather than sequestration.[71, 75] With advancing technologies hydrogen may ultimately be obtained from alternative sources such as electrochemical or photochemical conversion of water.[7, 76] However, until more efficient technologies are developed for producing H_2, inexpensive hydrocarbons rich in hydrogen, such as natural gas or biogas, may be exploited as a cheap hydrogen source.

We hypothesize that biomass partial oxidation with CO_2 addition can be exploited to recover all fuel carbon atoms as CO by generating molecular hydrogen in situ from hydrogen rich sources (Fig. 4.1). Previously, we have shown that through a process called reactive flash volatilization, cellulose can be rapidly converted to synthesis gas by catalytic partial oxidation over Rh-based catalysts without the formation of char.[29, 30] Results presented here suggest that biomass reforming, methane reforming, and water-gas-shift reactions can be integrated into one catalytic reactor stage. Our results show that a mixture of cellulose (a biomass surrogate), CO_2, and CH_4 can be converted to synthesis gas with no char formation and >100% yield of CO, defined here to be the ratio of moles of CO produced to moles of carbon in the fuel feed.

4.2 Experimental

The reactor setup and operation, effluent characterization, and catalyst preparation methodology are described in this section. Further experimental details for similar systems can also be found elsewhere.[30, 77]

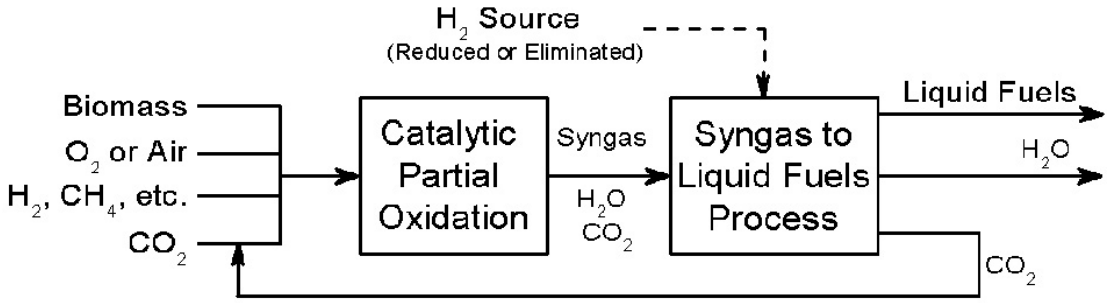

Figure 4.1: One possible schematic of the proposed process. Optimum process design would require, among other things, a coupled economic and process analysis, and detailed product specifications. Furthermore, depending on the CO_2 source, recycle may not be preferred.

4.2.1 Reactor Setup

Experiments were performed in a 20 mm I.D., 22 mm O.D. vertical quartz reactor tube. A 17 mm O.D., 10 mm deep γ-Al_2O_3 foam was used to support a 60 mm bed of 1.3 mm diameter catalyst spheres. The ceramic foam was inserted through the bottom of the reactor tube and held in place via friction fit against the quartz wall using ceramic cloth. The catalyst spheres were then charged from the open top of the quartz tube, before sealing the reactor for use.

Temperatures were measured at 20 mm and 40 mm from the front (top) face of the catalyst by 0.25 mm O.D. type K thermocouples. The thermocouples were inserted from the bottom of the reactor tube while loading the foam catalyst support, and held in place via friction fit between the quartz wall and ceramic cloth. The thermocouples were bent at an angle to place their tips at the middle of reactor tube and desired depth prior to catalyst loading.

Cellulose feed was controlled using a custom laboratory scale auger/hopper system. A 0.25 in. auger functioned as a volumetric feeder, moving cellulose from a sealed acrylic hopper to the reactor at constant rates. The auger was controlled by a laboratory mixer

accurate to 1 RPM, allowing for accurate control of cellulose mass feed rate. Lattice NT 200 microcrystalline cellulose purchased from FMC Biopolymer was used for these experiments. The cellulose was sieved to eliminate particles <300 μm to prevent small particles from adhering to the reactor wall before reaching the catalyst and to ensure uniform flow rates by facilitating flow into the auger. The cellulose was mixed with feed gases before entering the quartz tube for reaction.

N_2, O_2, CH_4, and CO_2 gas flow rates were controlled using mass flow controllers operated by LabVIEW software, accurate to 0.05 SLPM. Feed gases were fed through the hopper prior to being mixed with the cellulose and entering the reactor to equilibrate the gas mixture within the hopper to the desired feed concentration.

4.2.2 Reactor Operation

The reactor was started by first flowing a fuel-rich mixture of methane and oxygen diluted in nitrogen through the catalyst bed. An isolated portion of the catalyst was then heated by applying a butane torch flame to the exterior of the quartz reactor tube. Once the isolated portion of the catalyst reached ~300 °C the autothermal partial oxidation of the methane was initiated raising the entire bed temperature to ~900 °C. Insulation was then added to the exterior of the quartz reactor tube to minimize heat loss to the surroundings. Once the catalyst bed temperature reached steady state, cellulose was added at the desired flow rate. After the cellulose flow rate reached steady state the CH_4, O_2, N_2, and CO_2 flow rates were set to their desired values.

Gravimetric measurements were taken prior to reactor assembly to determine cellulose flow rate as a function of auger turn rate.

4.2.3 Measurement

Effluents were quantified and identified using an HP 5890 gas chromatograph (GC) equipped with a Plot Q capillary column and a thermal conductivity detector, which was calibrated to detect permanent gases and higher hydrocarbon species. Gas samples

(0.5 mL) were taken with a syringe through a sampling port downstream of the catalyst bed and injected into the GC. Products were quantified using predetermined response factors (using nitrogen as the internal standard) found using known quantities of premixed gases. Products were identified based upon their retention time in the column. Balances for H, O, and C generally closed within 5%.

A N_2 gas stream was added downstream of the catalyst bed and upstream of the sampling port to provide an internal standard for experiments with no N_2 in the gas feed. This was only necessary for experiments with feed gas ratios $CO_2/O_2>3.5$ and $N_2/O_2=0$. Under these conditions the CO_2 concentration in the effluent was very high causing increased variance in the carbon balances, requiring closure of the carbon balance around CO_2. All experiments were repeated at least three times, usually over multiple catalyst beds with no observable differences.

4.2.4 Catalyst Preparation

Catalysts used in these experiments were prepared on Saint-Gobain NorPro Corporation 1.3 mm diameter γ-Al_2O_3 spheres, details for which can be found elsewhere.[77] A 5 wt% γ-Al_2O_3 washcoat was deposited on the γ-Al_2O_3 spheres using the incipient wetness technique, which likely increases surface area and stabilizes the catalyst.[33] Once dry, the spheres were calcined in stagnant air for 6 hrs at 600 °C. The process was then repeated to add 1 wt% Rh and 1 wt% Ce catalyst to the γ-Al_2O_3 using a solution of $Rh(NO_3)_3$ and $Ce(NO_3)_36H_2O$ in distilled water. The catalysts were run under representative operating conditions in the reactor for at least 1 hr prior to data acquisition, and all catalysts were used for >25 hrs with no observable deactivation.

4.3 Results and Discussion

The relevant feed ratios for experimental consideration were predicted by calculating adiabatic equilibrium for all possible feed combinations of carbohydrates (cellulose),

methane, air (oxygen), and carbon dioxide (the calculation algorithm is presented in Appendix C of the supplementary information). Under the considered carbon fuel feed ratios of 0.25< $C_{(C_6H_{10}O_5)_n}/C_{CH_4}$ <1.00, there exists a distinct division (Fig. C.1 of Appendix C) between operating conditions that generate carbon dioxide and a region for which there is no net generation of carbon dioxide from fuel.

This complex chemistry can only occur rapidly with heterogeneous catalysts at high temperatures near adiabatic reactor conditions where there is no steady build-up of surface coke. There also exists a distinct set of reactor feed ratios for which no solid graphitic or amorphous carbon is predicted at equilibrium (Fig. C.2 of Appendix C).

Under feed conditions where fuel carbon is not converted to CO_2 or solid carbon, the carbon is converted to CO. Therefore, the overlap of these two regions on a ternary diagram in Fig. 4.2 depicts a narrow region of feed conditions that will permit CO yields >100% through catalytic biomass and CH_4 co-processing. These inlet concentrations minimize complete fuel combustion and result in temperatures higher than those at which methanation and carbon formation occurs (∼500 °C). Details describing the calculations that went in to constructing Fig. 4.2 can be found in Appendix C.

The results predicted by these equilibrium calculations were tested in experiments conducted with 300 μm cellulose particles with CH_4, O_2, CO_2, and N_2 in a 20 mm ID quartz reactor tube over a Rh-Ce/γ-Al_2O_3 catalyst supported on a 6 cm bed of 1.3 mm diameter α-Al_2O_3 spheres (inset, Fig. 4.3, described in detail elsewhere[77]). The Rh-Ce/γ-Al_2O_3 catalyst was selected for its high WGS and reforming activity, and stability.[78] Temperatures measured at 20 mm and 40 mm below the front catalyst surface ranged from 850-1125 °C depending on operating conditions and position in the catalyst bed. Complete conversion to synthesis gas and combustion products with no observable char or tar formation was observed at <30 ms gas residence time under continuous operation for all experiments reported.

The selectivity to CO in the reactor effluent shows that increasing the concentration of CO_2 in the absence of CH_4 co-feed has a weak effect on CO yield, consistent with

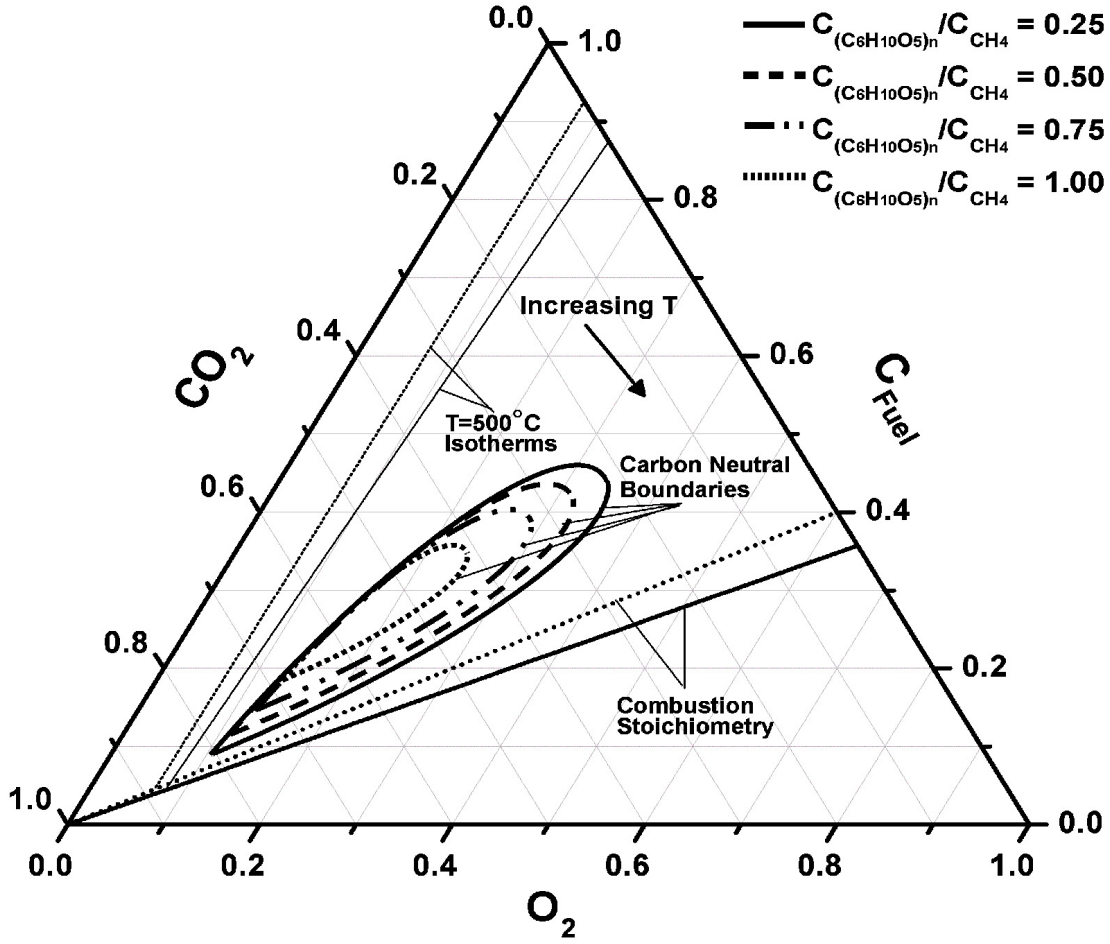

Figure 4.2: Operating diagram derived from adiabatic equilibrium calculations for CPO of cellulose and CH_4 at four constant feed ratios in air with no preheat, varying ratios Air/Fuel and Air/CO_2 over all possible concentrations. Results (renormalized without nitrogen) describe a regime of operation where solid carbon is not a thermodynamic product and there is zero net generation of CO_2, corresponding to CO yields $\geq$100%. Details on calculations and assembly of this figure can be found in Appendix C.

thermodynamic calculations represented by the dashed lines in Fig. 4.3. Alternatively, increasing concentrations of CH_4 in the absence of CO_2 co-feed significantly improves CO yield, increasing selectivity to CO from 19% to 62% for $C_{(C_6H_{10}O_5)_n}/C_{CH_4}$ feed ratios of ∞ and 1, respectively. Furthermore, increasing concentrations of CO_2 with high concentrations of CH_4 increases the CO yield by as much as 34% at $C_{(C_6H_{10}O_5)_n}/C_{CH_4}$=1. At CO_2/O_2=3.76 and CH_4/O_2=0.6 the system approaches a CO yield of 100%, indicating zero net generation of CO_2 in the reactor.

Selected experimental (Experiments 1-5) and theoretical (Calculations 1-5) results are presented in Table 4.1. Results from experiment 5 show a condition with >100% CO yield in the laboratory reactor, indicating complete conversion of carbon in cellulose and CH_4, and partial conversion of CO_2 carbon to CO.

Table 4.1: Selected experimental and theoretical (italics) data for the millisecond CPO of cellulose and CH_4 with CO_2 addition.[a]

Experiment/*Calculation*	1	2	3	4	5	*1*	*2*	*3*	*4*	*5*
Parameters										
Catalyst Bed Length (mm)	60	60	60	60	60	-	-	-	-	-
C/O Ratio	0.6	0.6	0.6	0.6	0.6	*0.82*	*0.79*	*1.00*	*0.91*	*0.70*
$C_{(C_6H_{10}O_5)_n}/C_{CH_4}$	∞	5	2	1	0.5	*0.5*	*0.25*	*0.75*	*0.25*	*0.5*
CH_4/O_2 Ratio	0	0.2	0.4	0.6	0.8	*1.09*	*1.27*	*1.14*	*1.45*	*0.93*
CO_2/O_2 Ratio	0	0.91	1.86	2.81	3.76	*1.81*	*1.59*	*0.57*	*0.31*	*2.6*
N_2/O_2 Ratio	3.76	2.86	1.91	0.95	0	*3.76*	*3.76*	*0*	*0*	*0*
Cellulose Flow (g hr^{-1})	50	50	50	50	50	-	-	-	-	-
Results										
Temperature (°C)										
20 mm	1061	1108	1040	1056	1139	-	-	-	-	-
40 mm	1018	965	897	916	985	-	-	-	-	-
Adiabatic	-	-	-	-	-	*652*	*643*	*895*	*892*	*953*
H Selectivity (%)										
H_2	14.9	27.4	26.3	23.7	29.6	*63.9*	*66.4*	*74.9*	*83.6*	*36.6*
H_2O	85.1	72.6	72.9	74.1	68.8	*33.7*	*29.3*	*25.0*	*16.2*	*63.3*
C Selectivity (%)										
CO (Yield[b])	19.5	43.0	71.3	94.5	107.6	*100.9*	*101.6*	*101.6*	*101.4*	*131.4*
CO_2	80.5	57.0	28.2	3.9	-8.7	*-2.8*	*-5.4*	*-1.7*	*-1.5*	*-31.4*
CH_4	0	0	0.5	1.6	1.1	*1.8*	*3.7*	*0.0*	*0.1*	*0.0*
Residence Time (ms)	28.1	23.4	19.1	13.7	9.3	-	-	-	-	-
Mass Velocity (hr^{-1})	43.0	51.6	64.5	86.1	129.1	-	-	-	-	-
H_2/CO	0.74	0.55	0.46	0.40	0.41	*1.02*	*1.15*	*1.11*	*1.46*	*0.45*
Syngas Yield (%)	6.5	16.1	27.5	40.0	51.1	*41.6*	*42.8*	*85.1*	*89.6*	*65.1*

[a] Details describing the calculations and assumptions that went into the assembly of this table can be found in Appendix D.
[b] Results for CO selectivity are identical to CO yield, because there is always 100% conversion of cellulose to C_1 products in the reactor.

Theoretical data presented in Calculation 4 of Table 4.1 show a condition with ~100% CO yield and H_2/CO ratio of 1.46, compared to H_2/CO~1 for traditional biomass gasification. Theoretical data presented in Calculation 5 show >130% CO yield compared to ~50% for traditional biomass gasification, which can be achieved at

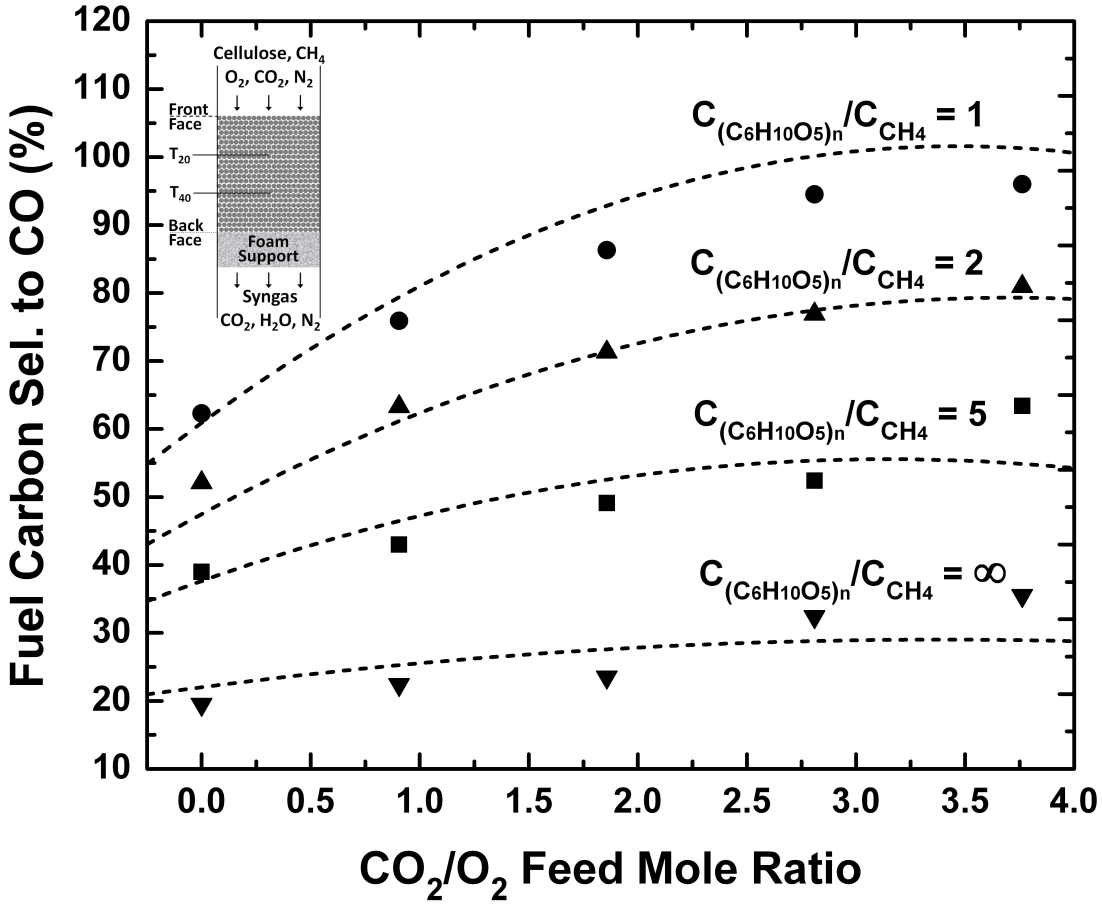

Figure 4.3: Fuel carbon selectivity to CO rapidly approaches equilibrium predicted concentrations (dashed lines) in the reforming of cellulose at constant flow rate 50 g hr^{-1} and fuel carbon to oxygen from O_2 ratio (C/O)=0.6, while varying ratios of the two fuels (cellulose and CH_4), N_2/O_2, and CO_2/O_2. At CO_2/O_2=3.76 and CH_4/O_2=0.6 the system approaches CO yields of 100%.

a cost to the product H_2/CO ratio.

This process works by co-reforming carbohydrate pyrolysis vapors with CH_4 and CO_2 in one heat-integrated catalyst bed. High temperatures generated in the oxidation zone allow for rapid heat conduction through the catalyst support, powering endothermic pyrolysis at the front of the catalyst, reforming within the catalyst bed, and eliminating char generation.[77, 79] CPO of methane in similar reactors has been shown to readily form CO and H_2, a crucial step that provides the hydrogen necessary to drive the reverse water-gas-shift reaction (Eqn. 4.2).[80]

Experiments show a rapid approach to equilibrium with minimal heat loss, validating the use of adiabatic equilibrium calculations to model reactor operation as noted by experiments and calculations presented in Fig. 4.3. Calculations indicate at least 20% lower CO selectivities are achieved for certain feeds with independent carbohydrate and CH_4 reforming, showing the importance of co-reforming CH_4 and biomass in one integrated reaction system (Table E.1 of Appendix E). Similar results could be achieved with three reactors individually undergoing methane CPO, carbohydrate reforming, and product gas equilibration by water-gas-shift. However, this arrangement is considerably more complex, and increases overall process cost.

4.4 Conclusions

Our research demonstrates for the first time that equilibrated, adiabatic, char-free biomass processing through co-feeding CH_4 at specific concentrations produces 100% carbon recovery as CO. Future research will focus on the mechanisms for reverse water-gas-shift in the presence of biomass-derived oxygenate CPO as well as hydrogen-coupling by methane decomposition, which are currently unknown. Additionally, utilizing the benefit of this reactor scheme requires considerable process design in conjunction with full biomass life-cycle and economic analysis. Finally, although lignocellulosic biomass has been experimentally shown to yield similar results to a pure cellulose feedstock[30],

in depth experiments assessing the long-term effect of ash on catalyst site deactivation must be performed.

4.5 Acknowledgements

This research was partially supported by the Initiative for Renewable Energy and the Environment (IREE) at the University of Minnesota, the US Department of Energy (DOE), the National Renewable Energy Laboratory (NREL), and the 3M Corporation.

Chapter 5

Steam Reforming of Benzene As a Model for Biomass-Derived Syngas Tars over Rh-Based Catalysts[1]

As described in Chapters 3 and 4, biomass catalytic partial oxidation proceeds in three primary steps: 1) homogeneous carbohydrate pyrolysis at the front face of the catalyst, 2) convection of pyrolysis vapors and co-feeds into the catalyst bed for oxidation, and 3) reforming of the syngas, combustion, and undesired tar products to chemical equilibrium. This chapter focuses on the reforming zone of the reactor, examining in depth the ability of Rh based catalysts to convert undesired tars to equilibrium synthesis gas products.

The ability of Rh based catalysts to remove undesired tars from biomass-derived

[1] **Parts of this chapter appear in: J.L. Colby, T. Wang, and L.D. Schmidt, "Steam Reforming of Benzene As a Model for Biomass-Derived Syngas Tars over Rh-Based Catalysts," *Energy and Fuels*, 2010, 24, 1341-1346 - Reproduced by permission of ACS Publications.**

syngas was examined under realistic operating conditions. Experiments were performed in a fixed bed reactor at temperatures of 650-850 °C and atmospheric pressure using C_6H_6 as a model tar compound. Benzene conversion exhibited a strong dependence on temperature and H_2O concentration in the feed. Significantly better catalyst performance was observed upon addition of Ce to the catalyst, which increased Rh dispersion and stability. The concentration of C_6H_6 in the feed had very little effect on catalyst performance. CO_2, H_2, and CO co-feeds had positive, neutral, and negative effects, respectively, on C_6H_6 conversion. A representative biomass-derived syngas mixture of N_2, H_2, CO, CO_2, H_2O, and C_6H_6 was tested on the Rh-Ce catalyst at 850 °C and 2 SLPM total flow rate, resulting in almost complete C_6H_6 conversion to a near equilibrium product stream.

5.1 Introduction

Gasification of biomass to synthesis gas, a mixture of H_2 and CO, is one process being pursued as a possible method for converting carbohydrates into power, fuels, and chemicals. In addition to H_2 and CO, a typical biomass gasifier effluent contains N_2, H_2O, CO_2, CH_4, and approximately 5 wt% tars.[81] These tars, composed largely of benzene, toluene, and other aromatic or polyaromatic compounds, are harmful to downstream processing equipment, condensing on pipes, filters, and other equipment, and causing catalyst deactivation.[82] Removal of tars is generally considered the single greatest technical barrier to the large scale development of biomass gasifiers.[83] For this reason, there is significant ongoing research to minimize or eliminate undesired tars from biomass gasifier product streams.

Tars can be removed from gasification processes through primary processes, where tars are eliminated within the gasifier, or secondary processes, which occur in a separate reactor or unit operation downstream of the gasifier. The more common methods for removing tars include physical means such as filtration, or chemical processes such

as thermal cracking or catalytic destruction.[23] Filtration generally requires multiple expensive downstream unit operations, while thermal cracking demands extremely high temperatures, requiring large energy inputs. Catalytic destruction of tars is advantageous because it requires more moderate temperatures of approximately 650-850 °C, similar to those observed in typical biomass gasifiers, and only one additional unit operation.[82]

Many research groups have examined the reforming of model tar compounds on a variety of metal and nonmetal catalysts. An in depth review was published in 1998 by Milne and Evans examining the current literature on biomass-derived syngas cleanup.[23] More recently, two reviews by Dayton and Yung have focused on literature addressing the catalytic conditioning of biomass-derived syngas.[82, 84] To date, studies focused largely on catalyst metal, support, and synthesis, and it was observed that metal-based catalysts, namely Rh, more rapidly remove tar compounds from gasification processes than other metal catalysts.

Addition of catalysts to the primary process unit, such as fluidized bed gasifiers, has been shown to reduce tar yields but not eliminate them.[23, 85, 86, 87] However, in recent papers we have shown that fuels such as cellulose and aspen wood can be completely gasified in a single reactor unit to tar free synthesis gas over Rh-based catalysts by autothermal partial oxidation. [30, 77] This process integrates pyrolysis, oxidation, and reforming chemistries into one monolithic foam reactor. The reforming zone of this reactor assists in chemical species progression toward equilibrium through reforming chemistry. Additional research elucidating the phenomena in this portion of the catalyst may be useful for further developing the catalytic partial oxidation process and secondary clean up of biomass-derived syngas.

Here we study the activity of Rh and Rh-Ce catalysts supported on 65 ppi α-Al_2O_3 foam monoliths in the steam reforming of benzene, used as a model compound for biomass derived tars. C_6H_6 was selected for its abundance in biomass gasifier tars

(∼40 wt% of tars) and its stability in the gas phase, selecting almost entirely for heterogeneous reactions in the system.[88] Activity was measured as a function of temperature and H_2O concentration in the feed. H_2, CO, CO_2, and C_6H_6 concentrations were also varied holding temperature and H_2O concentration constant to determine their effect on catalyst performance. Product data was used to gain insight into the catalyst metal and support role in C_6H_6 reforming, and facilitate the construction of a reaction scheme. Finally, catalyst characterization by XRD was performed to help form conclusions about catalyst stability.

5.2 Experimental Section

5.2.1 Reactor Setup

Benzene reforming activity was studied over Rh-based catalysts in a 20 mm I.D., 22 mm O.D. quartz reactor tube (Figure 5.1). Catalysts were supported on 17 mm diameter, 1 cm length, and 65 ppi (pores per linear inch) α-Al_2O_3 foam monoliths wrapped in ceramic insulation and held in the reactor tube by friction fit. 65 ppi α-Al_2O_3 foam monoliths with no catalyst loading were placed on either side of the catalytic foam, acting as radiation heat shields. Two type K thermocouples were inserted from the downstream side of the reactor and placed at the center of the front and back face of the catalyst to monitor temperature during operation.

CO_2, CO, and H_2 gases were metered by mass flow controller and fed to the reactor tube through a quartz Y-piece. N_2 was metered by mass flow controller (accurate to ($\pm$0.02 SLPM) and fed to two Pyrex nebulizers (Precision Glassblowing of Colorado) at either end of the quartz Y-piece, used to facilitate vaporization of liquid feeds. H_2O and C_6H_6 were each fed to a nebulizer by Chrom Tech HPLC pump (accurate to 0.01 mL min^{-1}) and Isco syringe pump (accurate to 0.001 mL min^{-1}) respectively. The walls of the quartz Y-piece were heated externally with heating tape to ∼300 °C to vaporize the liquid feeds. A blank 45 ppi α-Al_2O_3 foam was placed at the start of

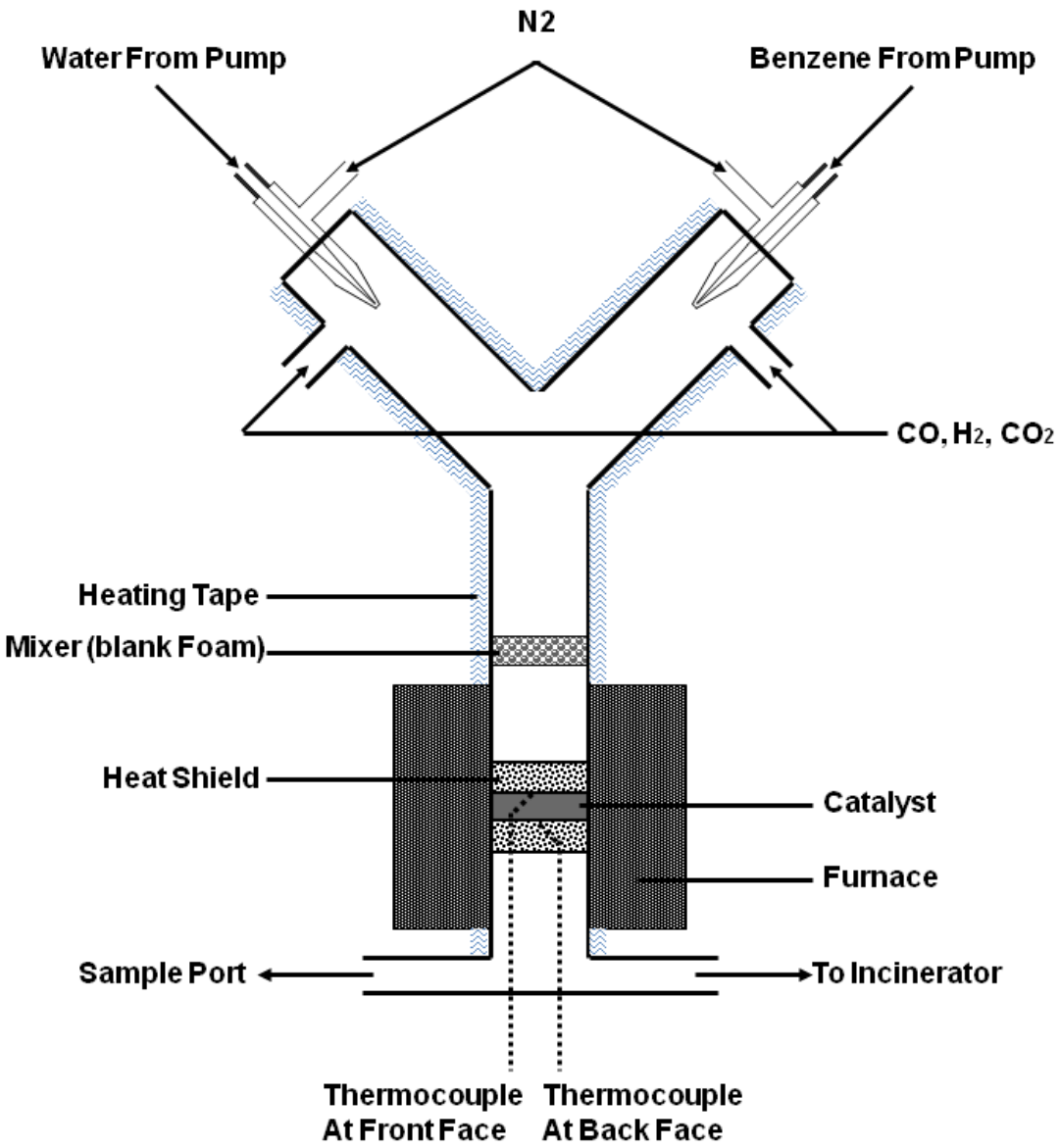

Figure 5.1: The primary reactor consisted of a 20 mm I.D. quartz reactor tube placed in a temperature controlled tube furnace. Liquid C_6H_6 and H_2O feeds were nebulized by N_2 at either end of a heated quartz Y-piece to facilitate vaporization. CO, H_2, and CO_2 were co-fed below the nebulizers for mixing prior to entering the catalyst bed.

the primary reactor tube for mixing.

The quartz reactor tube was placed in a tubular furnace powered by an Omega benchtop temperature controller, which monitored and maintained the front face catalyst temperature to ±1 °C in the range 650-850 °C.

5.2.2 Catalyst Synthesis

Catalysts tested were 0.5 wt% Rh and 0.5 wt% Rh with 1 wt% Ce, both prepared on 65 ppi α-Al_2O_3 foam monoliths by the incipient wetness technique.[33] Rh and Ce were dissolved in distilled water as $Rh(NO_3)_3$ (Alfa Aesar) and $Ce(NO_3)_3{\cdot}6H_2O$ (Sigma-Aldrich) respectively, before added dropwise to the α-Al_2O_3 foam. Once dry, the catalyst was calcined for 6 h at 600 °C. Catalysts were conditioned for ∼1 h under representative conditions before acquisition of performance data.

5.2.3 Product Analysis

Catalyst performance data was obtained by sampling reactor effluent directly to an HP 6890 gas chromatograph equipped with a 30 m long, 0.32 mm I.D. Plot-Q capillary column, thermal conductivity detector, and flame ionization detector. The GC was calibrated to quantify H_2, CO, CH_4, CO_2, and C_6H_6, with reference to N_2 as the internal standard. Mass balances for C, H, and O generally closed within ±5%for each sample analyzed, and at least three samples were taken (and results averaged) for each data point presented. Selected operating conditions were repeated on multiple catalysts of the same metal loading with no observable differences in performance.

Equilibrium calculations were performed by minimization of Gibbs free energy at 1 atm pressure and an average between the front and back face catalyst temperature using HSC Chemistry software.[46]

5.2.4 Catalyst Characterization

Catalyst crystallinity was measured by X-ray diffraction using a Bruker-AXS (Siemens) D5005 wide angle diffractometer with a 2.2 kW sealed Cu source. Data was first obtained for the intact monolithic foams, placed in a custom sample holder exposing only the front or back catalyst surfaces for measurement. The catalysts were then individually crushed to powder, well mixed, and measured again to check for consistency within each catalyst foam.

5.2.5 Temperature Considerations

Furnace temperature was controlled to hold the front face catalyst temperature constant at a specified value between 650 and 850 °C. The back face temperature diverged below set point with increasing endothermic reforming activity in the catalyst bed. The largest gradient observed between the front and back faces of the catalyst was 50 °C. For all data presented in the current work, temperature information is in reference to the front face catalyst temperature.

5.3 Results and Discussion

5.3.1 Product Selectivities

H_2, CO, CO_2, H_2O, N_2, and C_6H_6 were the primary species observed in the product stream for all experiments presented. Methane was also observed, generally in concentrations on the order of 10 ppm. Due to its extremely low concentrations and because CH_4 formation was not a primary reaction in the system, CH_4 will be omitted from discussions.

Selected feed and product information for C_6H_6 steam reforming over Rh/α-Al_2O_3 and Rh-Ce/α-Al_2O_3 catalysts are presented in Table 5.1. A C_6H_6 conversion of 9.7% was observed for S/C of 0.42 over the Rh catalyst at 750 °C (Table 5.1, Experiment 1).

All carbon from the reacted C_6H_6 was converted to CO. The absence of CO_2 in the product stream indicates zero net consumption of CO through the water-gas-shift (WGS) reaction (Equation 5.1). Furthermore, this suggests that all H_2 was generated through steam reforming according to Equation 5.2. According to the stoichiometry of this reaction the product H_2/CO ratio should be 1.5, in close agreement with the H_2/CO ratio of 1.76 observed in the product stream.

$$H_2O + CO \leftrightarrow H_2 + CO_2 \tag{5.1}$$

$$C_6H_6 + 6H_2O \rightarrow 6CO + 9H_2 \tag{5.2}$$

Table 5.1: Selected experimental data for the steam reforming of benzene over Rh/α-Al_2O_3 and Rh-Ce/α-Al_2O_3 catalysts.[a]

Experiment	1	2	3	4
Feed Information				
N_2 (mol%)	93	78	93	78
H_2O (mol%)	5	20	5	20
C_6H_6 (mol%)	2	2	2	2
S/C	0.42	1.67	0.42	1.67
Catalyst	Rh	Rh	Rh-Ce	Rh-Ce
Temperature (°C)	750	850	750	850
Product Information (Experiment/Equilibrium[b])				
C_6H_6 conversion (%)	9.7/*100*	49.8/*100*	29.0/*100*	99.8/*100*
Total flow rate (mol min^{-1})	0.083/*0.094*	0.088/*0.094*	0.086/*0.094*	0.094/*0.094*
Product concentration (mol%)				
N_2	91.5/*80.7*	72.2/*67.7*	88.9/*80.7*	67.7/*67.7*
H_2O	3.2/*0.1*	10.5/*4.9*	0.7/*0.1*	4.8/*4.9*
C_6H_6	1.8/*0.0*	0.9/*0.0*	1.4/*0.0*	0.0/*0.0*
H_2	2.3/*9.0*	10.5/*17.3*	5.5/*9.0*	17.3/*17.3*
CO	1.3/*3.9*	4.1/*8.1*	3.3/*3.9*	7.9/*8.1*
CO_2	0.0/*0.1*	1.8/*2.0*	0.2/*0.1*	2.2/*2.0*
C(s)	0.0/*0.6*	0.0/*0.0*	0.0/*6.2*	0.0/*0.0*

[a] All experiments were considered on 17 mm diameter, 1 cm length α-Al_2O_3 foam monoliths loaded with 0.5 wt% Rh or 0.5 wt% Rh and 1 wt% Ce. Total feed flow was held constant at 2 SLPM.
[b] Thermodynamic equilibrium was calculated at constant temperature by minimization of Gibbs free energy.

At a temperature of 850 °C and S/C of 1.67 a C_6H_6 conversion of 49.8% was observed over the same catalyst (Table 5.1, Experiment 2). The higher C_6H_6 conversion resulted in higher concentrations of CO and H_2 in the product stream. Additionally, 1.8 mol% CO_2 was present in the effluent, resulting from high concentrations of CO and unconverted H_2O driving the WGS reaction. The WGS activity explains the increased H_2/CO ratio of 2.56, higher than predicted by the stoichiometry of Equation 5.2.

These experiments were also performed over Rh-Ce catalysts, presented in Table 5.1, Experiments 3 and 4. The higher activities observed with the addition of Ce to the catalyst resulted in an increase in H_2 and CO concentrations in the product stream. Trends in H_2/CO ratio and CO_2 production were similar to those observed over Rh catalysts. At a temperature of 850 °C and S/C of 1.67, species concentrations in the system approach chemical equilibrium over Rh-Ce catalysts.

Chemical equilibrium data for the product streams, calculated by minimization of Gibbs free energy, are presented in italic font in Table 5.1. Benzene is not a thermodynamic product under any experimental conditions presented in this paper. At low S/C ratios such as that presented in Experiments 1 and 3, solid carbon is a stable thermodynamic product. Although it is possible that a steady-state layer of carbon was present on the catalyst during experiments, over tens of hours of reactor operation there was no observable accumulation of carbon on the catalyst surface. This may be explained by the fact that the system never reached chemical equilibrium at low S/C ratios. As C_6H_6 conversion approaches 100% (observed at high temperatures and H_2O concentrations over Rh-Ce catalysts) the system tends toward thermodynamic equilibrium, suggesting that C_6H_6 consumption through steam reforming is the rate limiting step. This observation agrees with previous works, which indicate the WGS reaction proceeds rapidly to equilibrium, remaining quasi equilibrated as reforming reactions proceed to completion.[78, 89]

5.3.2 Effect of Temperature and H_2O Concentration

Rh Catalyst

The effect of steam reforming activity on temperature and water concentration in the feed was studied on a Rh/α-Al_2O_3 catalyst at five different temperatures (Figure 5.2A). Benzene feed concentration and total flow rate were held constant at 2 mol% and 2 SLPM respectively for all data presented.

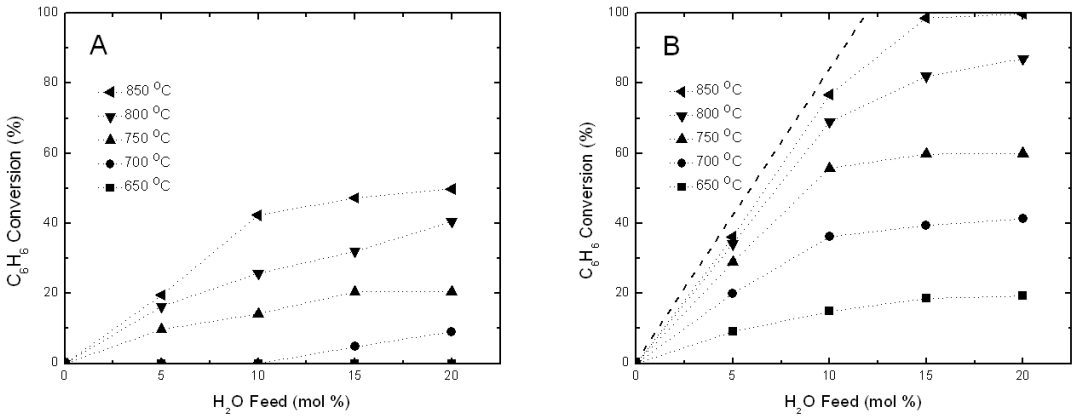

Figure 5.2: Benzene conversion as a function of H_2O concentration in the feed at five different catalyst front face temperatures. Results are shown for Rh/α-Al_2O_3 (A) and Rh-Ce/α-Al_2O_3 (B) catalysts at 2 SLPM total flow, 2 mol% C_6H_6, variable H_2O concentrations, and the balance N_2. The bold dashed line in panel B represents the expected benzene conversion for 100% stoichiometric consumption of feed H_2O through steam reforming.

At 850 °C and 20 mol% H_2O in the feed there is 50% C_6H_6 conversion. This value decreases with decreasing concentrations of water in the feed. Between 0 and 10 mol% H_2O in the feed, C_6H_6 conversion has a strong dependence on H_2O concentration increasing linearly from 0 to 42%. Between 10 and 20 mol% H_2O, C_6H_6 conversion has a weak dependence on H_2O concentration increasing from 42 to 50% over the entire range.

The conversion of C_6H_6 decreases with decreasing front face catalyst temperature. There is zero observable catalyst activity below 15 mol% H_2O at 700 °C, and for all H_2O concentrations at 650 °C. Additionally, at lower temperatures the increase in C_6H_6 conversion is relatively linear with increasing H_2O concentrations.

Rh-Ce Catalyst

The effect of temperature and water concentration in the feed on steam reforming activity was also studied on a Rh-Ce/α-Al_2O_3 catalyst under the same conditions presented in the previous section (Figure 5.2B). Ce was added to the catalyst for its ability to stabilize, disperse, and transfer oxygen to the Rh catalyst sites.[90, 91, 92]

At 850 °C and 15 mol% H_2O in the feed there is nearly complete conversion of C_6H_6, a 2-fold increase in activity compared to the Rh/α-Al_2O_3 catalyst. At this temperature, as the concentration of water in the feed is decreased the conversion of C_6H_6 decreases, closely matching the maximum conversion expected according to the stoichiometry of Equation 5.2 (represented by the bold dashed line in Figure 5.2B).

At high temperatures on the Rh-Ce catalyst, water is limiting in the reforming reaction below 12 mol% H_2O in the feed. This contributes to an increase in C_6H_6 conversion dependence on H_2O concentration. Above 12 mol% H_2O the stoichiometry of the feed does not prevent reforming from proceeding to completion, meaning surface reaction rates dictate the C_6H_6 conversion.

Similar to the Rh/α-Al_2O_3 catalyst, as the front face catalyst temperature decreases the activity of the catalyst decreases. However, the addition of Ce maintains catalytic activity at low temperatures and H_2O concentrations. This can be explained by the ability of Ce to increase rates of oxygen transfer by forming intermetallic compounds and storing oxygen, in addition to physically dispersing and supporting the Rh sites.[93]

5.3.3 Catalyst Stability

Rh Catalyst

Data were periodically repeated to test for catalyst deactivation. After more than 40 h on stream the Rh/α-Al_2O_3 catalyst exhibited no significant deactivation (C_6H_6 conversion remained within experimental error). XRD patterns are presented in Figure 5.3C for fresh and used Rh catalysts supported on α-Al_2O_3 monolithic foams. XRD patterns were also measured after crushing the catalysts into a powder to obtain a more averaged measurement over the entire catalyst (Figure 5.3A). Results were the same for both the monolith and powder measurements, and are presented normalized to the largest α-Al_2O_3 peak.

There is a clear increase in primary Rh peak height at 41.2° for the used catalyst (Figure 5.3, Panel A). The smaller peak for the fresh catalyst relative to the used one indicates that a higher fraction of the fresh Rh catalyst is in a more amorphous state, suggesting that the particles are smaller and more dispersed on the Al_2O_3 surface. The larger crystallites likely present in the used catalyst have low-index surface planes, reducing their activity relative to smaller clusters.[94]

Rh-Ce Catalyst

After more than 40 h on stream, the Rh-Ce/α-Al_2O_3 catalyst also exhibited no signs of deactivation. XRD patterns are presented in Figure 5.3C for fresh and used Rh-Ce catalysts supported on α-Al_2O_3 monolithic foams. XRD patterns for the ground Rh-Ce catalyst are also presented in Figure 5.3B. Results were the same in both the monolith and powder measurements, and are always presented normalized to the largest α-Al_2O_3 peak.

The lack of a significant Rh peak for the fresh and used catalyst indicates the Rh particles are highly amorphous, suggesting small particle sizes. Furthermore, there is

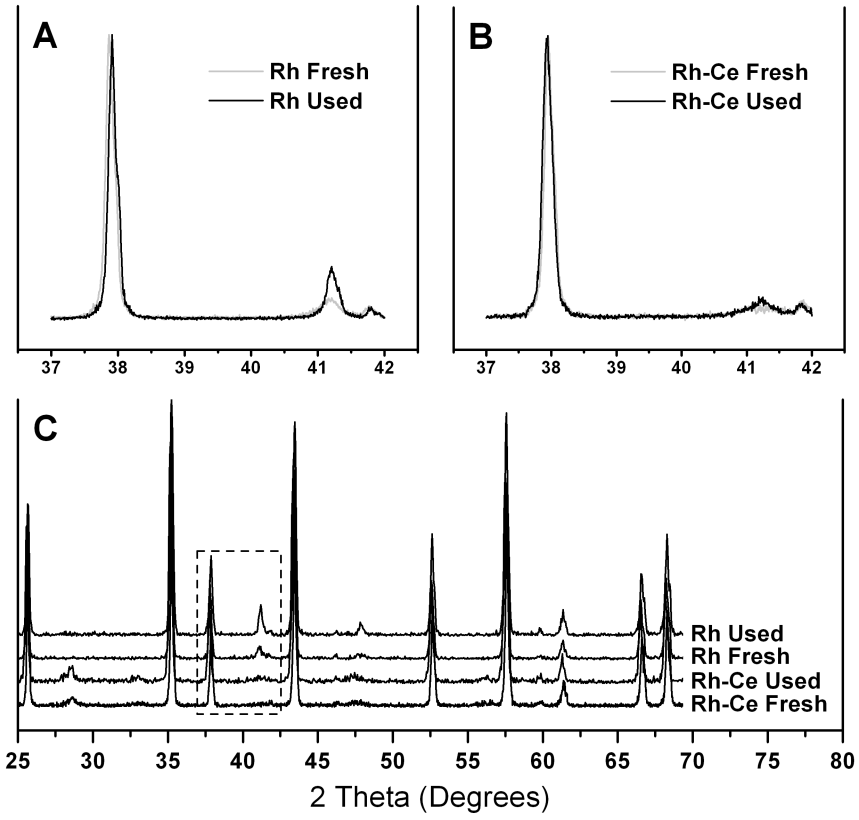

Figure 5.3: XRD patterns of Rh/α-Al_2O_3 and Rh-Ce/α-Al_2O_3 catalysts before and after use. All patterns are normalized to the largest peak (Al_2O_3 peak at 35°) to facilitate comparison of the primary Rh peak at 41.2°. Panel C contains the full patterns for both monolith catalysts, fresh and used, staggered relative to one another by 10% of maximum height. Panels A and B contain patterns for crushed Rh (fresh and used) and Rh-Ce (fresh and used) catalysts respectively. Results in Panel A indicate an increase in Rh crystallinity, suggesting an increase in crystallite size adn therefore particle size. Results in Panel B indicate no change in Rh crystallinity between fresh and used catalysts with Ce.

essentially no difference in Rh peak height between the used and new catalysts (Figure 5.3B), indicating that minimal catalyst sintering takes place during operation. The addition of Ce has been previously shown to physically stabilize and disperse Rh catalyst sites.[90, 91] These observations help to explain the increase in activity upon adding Ce to the catalyst.

5.3.4 Effect of Benzene Concentration

The effect of C_6H_6 concentration in the feed on reforming activity was studied on a Rh-Ce/α-Al_2O_3 catalyst (Figure 5.4). Temperature, steam concentration, and total flow rate were held constant at 750 °C, 10 mol%, and 2 SLPM, respectively, whereas C_6H_6 concentration was varied between 1 and 4 mol% in increments of 1 mol%.

At 1 mol% C_6H_6 in the feed there is 87% C_6H_6 conversion, corresponding to a C_6H_6 consumption rate of 7.2×10^{-4} mol min^{-1}. As the C_6H_6 concentration in the feed is increased to 4 mol%, the conversion drops to 20%. However, the total C_6H_6 consumption rate remains in a narrow range between 6.5×10-4 and 8.6×10-4 mol min^{-1}, exhibiting a weak dependence on C_6H_6 concentration under these conditions. This can be explained by the fact that C_6H_6 adsorption onto the catalyst surface is likely not rate limiting.[95]

5.3.5 Effect of H_2, CO, and CO_2 Cofeeds

The effect of H_2, CO, and CO_2 cofeeds on C_6H_6 steam reforming activity was studied on a Rh-Ce/α-Al_2O_3 catalyst (Figure 5.5). Temperature, steam concentration, benzene concentration, and total flow rate were held constant at 750 °C, 10 mol%, 2 mol%, and 2 SLPM, respectively, whereas H_2, CO, and CO_2 concentrations were independently fed and varied from 0 to 20 mol% in the feed.

Cofeeding CO_2 to the system increased C_6H_6 reforming activity. At high CO_2 concentrations C_6H_6 conversion was observed to increase by 7.6%. It is generally agreed that CO_2 has a strong positive influence on reforming activity. However, a debate still remains about whether CO_2 contributes through direct dry reforming according

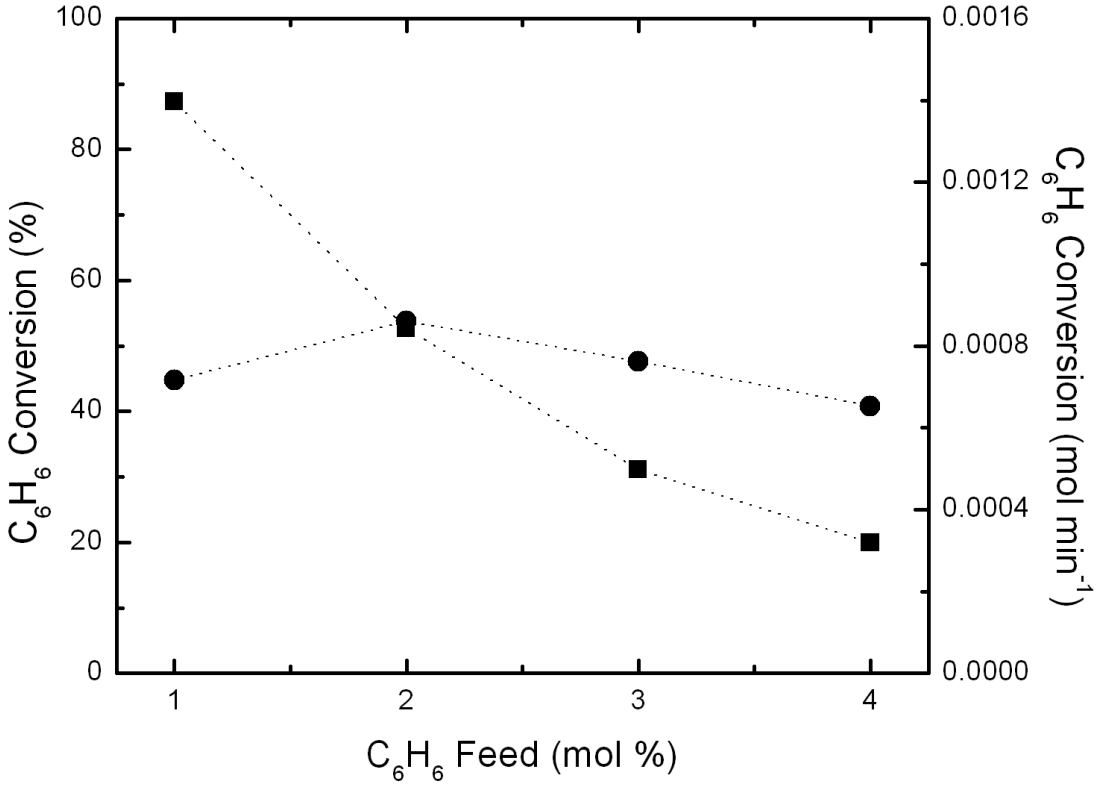

Figure 5.4: Benzene conversion rate and percent converted as a function of benzene concentration in the feed at 750 °C over a Rh-Ce/α-Al_2O_3 catalyst at 2 SLPM total flow, 10 mol% H_2O, variable C_6H_6 concentrations, and the balance N_2.

to Equation 5.3,[95] or through a combination of reverse water-gas-shift (RWGS) and steam reforming.[96]

$$C_6H_6 + 6CO_2 \rightarrow 12CO + 3H_2 \tag{5.3}$$

Cofeeding H_2 to the system had no observable effect on C_6H_6 reforming activity. From this it can be inferred that product inhibition through blocking of active sites by H_2 was negligible. Furthermore, due to small concentrations of CO_2 generated through C_6H_6 reforming, H_2 reaction with CO_2 through RWGS to generate additional H_2O for steam reforming was insignificant.

Cofeeding CO to the system decreased C_6H_6 reforming activity. At high CO concentrations C_6H_6 conversion was observed to decrease by 13%. There are two possible explanations for the observed decrease in activity. The first is that CO inhibits reaction by adsorption onto catalyst active sites.[97] The second is that dry reforming is a combination of RWGS and steam reforming[96] and the high concentrations of CO and H_2O in the feed drive the production of CO_2 and consumption of H_2O via WGS.

Previous works have shown that H_2 and CO coverages are negligible on Rh at operating temperatures above 600 °C.[98] This suggests catalyst active site inhibition by H_2 and CO is negligible in the current system. Therefore, the addition of CO to the system likely decreased C_6H_6 conversion by reducing H_2O concentrations via WGS. By this reasoning, CO_2 addition increased C_6H_6 conversion primarily through H_2O production by RWGS.

5.3.6 Simulated Biomass-Derived Syngas

Experiments were performed using a representative biomass-derived syngas mixture over a Rh-Ce/α-Al_2O_3 catalyst at 2 SLPM total flow and 850 °C. Feed and product information is presented in Table 5.2. Recommended feed concentrations[81] were reproduced as closely as possible within the limits of the experimental apparatus, using C_6H_6 as the model tar compound.

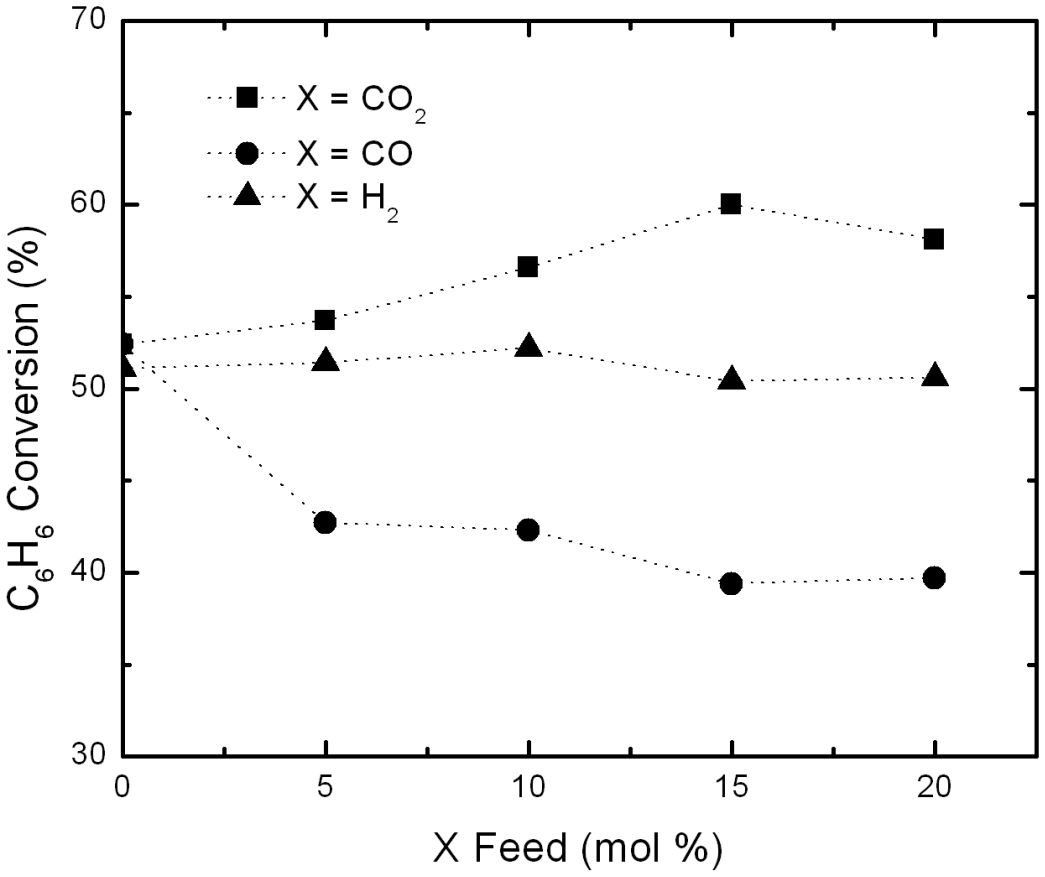

Figure 5.5: Benzene conversion as a function of CO, CO_2, and H_2 feed concentration at 750 °C over a Rh-Ce/α-Al_2O_3 catalyst at 2 SLPM total flow, 2 mol% C_6H_6, 10 mol% H_2O, variable CO, CO_2, or H_2 concentrations, and the balance N_2.

Results indicate nearly complete conversion of C_6H_6 in the reactor to a concentration of only 5 ppm. Products approached equilibrium at 2 SLPM total flow rate corresponding to a gas residence time of ∼40 ms, which demonstrates minimal inhibition of reforming by the syngas cofeeds. In addition to nearly complete tar removal, the product stream contained 23.1 mol% H_2 and 27.8 mol% CO, an increase of 3.1 and 7.8 mol% respectively. The observed high conversions at low residence times may make the process appealing for scale up. However, long-term experiments examining catalyst loss and deactivation are needed before considering such a process for commercialization.

Table 5.2: Experimental results for reforming of a typical biomass-derived syngas at 850 °C on Rh-Ce/α-Al_2O_3 catalysts.[a]

Syngas Species (mol%)	N_2	CO	H_2	CO_2	H_2O	Tars
Feed information						
Recommended by literature[81]	36.1	24.6	22.4	9.1	6.6	0.5-1.2
Experimental	43.3	20	20	9.1	6.6	1
Product information						
Predicted by equilibrium	40.1	27.8	23.1	4.6	4.3	0
Experimental	40.3	26.3	23.6	5.14	4.69	0.0005

[a]Benzene was used experimentally and in equilibrium calculations to represent the tar fraction of the syngas feed. Results indicate a near equilibrium product stream (ppm levels of benzene) using a representative biomass-derived syngas stream at 2 SLPM total flow corresponding to approximately 40 ms contact time. Thermodynamic equilibrium was calculated at constant temperature by minimization of Gibbs free energy.

5.3.7 Reaction Scheme

Benzene reforming leads primarily to the production of H_2, CO, H_2O, and CO_2. The process likely begins with the adsorption of C_6H_6 onto Rh catalyst sites to undergo C-H or C-C bond cleavage.[99] At temperatures typical in biomass-derived syngas, C_6H_6 has been shown to experience rapid and complete dehydrogenation to form surface carbon (C∗) and H_2.[100] The C∗ formed is highly stable with a low probability of desorption, requiring further reaction (typically oxidation) before leaving the catalyst surface.

Reaction of C∗ likely takes place with hydroxyl groups derived from the dissociation

of H_2O on the support[89, 92, 94] to OH$*$ and H$*$.[89, 101] Alternatively, H_2O can react with ceria in its reduced state, donating oxygen to the ceria lattice to form H_2.[102] Once formed, the hydroxyl groups can then be transferred to the Rh metal for reaction with C$*$.

The OH$*$ groups transfer from the oxide support to the Rh catalyst to react with C$*$ to form CO. Increasing temperature can improve the rate of hydroxyl transfer in the system. The addition of ceria to the system has also been shown to increase the rate of hydroxyl transfer between the oxide support and metal.[92, 102] The C$*$ on the metal surface can be oxidized through a redox cycle in which ceria is oxidized by an oxygen containing species on the surface and then transfers oxygen to the metal catalyst.[103, 104] This, in addition to its role as a physical stabilizer, may contribute to the large improvement in catalyst performance observed experimentally upon adding Ce to the Rh-based catalyst.

5.4 Conclusions

It was demonstrated that C_6H_6, used as a model for biomass-derived syngas tars, can be efficiently converted to CO, CO_2, H_2O, and H_2 by steam reforming over Rh-based catalysts supported on α-Al_2O_3 monolithic foams. Benzene conversion was shown to exhibit a strong dependence on temperature and H_2O concentration in the feed. Significantly better catalyst performance was observed upon adding Ce to the Rh-based catalyst. Addition of Ce appeared to physically stabilize the Rh, maintaining smaller more amorphous catalyst sites as demonstrated through XRD analysis.

The concentration of C_6H_6 in the feed had very little effect on its rate of conversion. Addition of CO_2, H_2, and CO cofeeds was examined and it was found that (1) CO_2 increases C_6H_6 conversion primarily through RWGS reaction combined with steam reforming, (2) H_2 had little effect on the system, and (3) CO reduces C_6H_6 conversion likely through H_2O consumption by WGS, reducing steam reforming activity.

Finally, a representative biomass-derived syngas stream was tested in the reactor system. At 850 °C and 2 SLPM total flow rate (corresponding to ∼40 ms gas contact time) the mixture proceeded almost entirely to equilibrium with only 5 ppm C_6H_6 remaining in the product stream, demonstrating the reactor's effectiveness as a syngas cleanup stage.

5.5 Acknowledgment

This work was supported by General Electric Global Research under United States Department of Agriculture Award No. DE-FG36-OBGO18085. This work was also partially supported by the China Scholarship Council. We acknowledge Dr. Ke Liu and Dr. Lingzhi Zhang of GE Global Research and Professor Yuan Kou of Peking University.

Chapter 6

Reactive Boiling of Cellulose for Integrated Catalysis Through an Intermediate Liquid[1]

As described in Chapters 3 and 4, biomass catalytic partial oxidation proceeds in three primary steps: 1) homogeneous carbohydrate pyrolysis at the front face of the catalyst, 2) convection of pyrolysis vapors and co-feeds into the catalyst bed for oxidation, and 3) reforming of the syngas, combustion, and undesired tar products to chemical equilibrium. This chapter focuses on first step of the process, examining how the system is able to run continuously without the formation of undesired chars during homogeneous carbohydrate pyrolysis, a problem hindering the development of traditional biomass processing techniques. A more detailed discussion of experimental setups and calculations used in this chapter can be found in Appendix F.

Advanced biomass processing technology integrating fast pyrolysis and inorganic

[1] **Parts of this chapter appear in: P.J. Dauenhauer, J.L. Colby, C.M. Balonek and L.D. Schmidt, "Reactive Boiling of Cellulose for Integrated Catalysis Through an Intermediate Liquid," *Green Chemistry*, 2009, 11, 1555-1561 - Reproduced by permission of The Royal Society of Chemistry (RSC).**

catalysis requires an improved understanding of the thermal decomposition of biopolymers in contact with porous catalytic surfaces. High speed photography (1000 frames per second) reveals that direct impingement of small microcrystalline cellulose particles with rhodium-based reforming catalysts at high temperature (700 °C) produces an intermediate liquid phase that reactively boils to vapors. The intermediate liquid maintains contact with the porous surface permitting high heat transfer (MW m^{-2}) generating an internal thermal gradient visible within the particle as a propagating wave of solid to liquid conversion. Complete conversion to liquid yields a fluid droplet on the catalyst surface exhibiting a linear decrease in droplet volume with time leaving behind a clean surface absent of solid residue (char). Under specific interfacial conditions, conversion with large cellulosic particles on the length-scale of wood chips (millimeters) occurs continuously as generated liquid and vapors are pushed into the porous surface.

6.1 Introduction

The search for advanced processing technologies capable of efficiently converting biomass to fuels and chemicals has led to the combination of solid biomass pyrolysis and catalytic processes. Direct utilization of catalysts with biomass requires the large biopolymers of lignocellulose to be broken down to species capable of interacting with catalytic active sites while maintaining catalyst integrity.[7] Emerging technologies have shown that high temperature decomposition (e.g. fast pyrolysis) pairs well with the use of inorganic catalysts due to similar processing rates, occurring orders of magnitude faster than existing biological processes (e.g. enzymatic hydrolysis).[75, 105, 106] Recently, Huber et al. demonstrated mixed pyrolysis/catalysis by rapid heating of cellulose particles in the presence of aluminosilicates (e.g. ZSM-5), which both cracked large biopolymers and converted the organic intermediates to highly desirable gasoline-like aromatic species.[107] Additionally, Schmidt et al. demonstrated that alumina-supported reforming catalysts combined with cellulose pyrolysis efficiently produce synthesis gas (H_2 +

CO) and allow for selective tuning of product ratios.[30, 77]

However, the mechanism by which cellulose thermally decomposes to volatile organic compounds (VOCs) on catalytic surfaces for downstream processing is unknown, hindering advancement of catalytic biomass reactors. The process generally occurs by cellulose particles impacting a high temperature surface, driving endothermic pyrolysis of the polymer structure to VOCs. These products are then convected from the particle to the neighboring solid, interacting chemically with the catalyst surface. Unknowns within this complex set of interacting phenomena are the dominant method of heat transfer to particles (convection, radiation, or conduction), the state of the cellulose particle over the course of conversion (solid or liquid), the extent of particle homogeneity, the physical interaction between the particle and surface, and the rate limiting phenomenon (pyrolysis or some mode of heat transfer). The complex nature of the system prevents substantial understanding by transport models integrating particle, surrounding gas, and surface chemistry.

This paper examines the conversion of cellulose particles in direct contact with high-temperature catalytic reforming catalysts in the presence of oxygen. Small, pure particles of cellulose on the length scale of 10-400 μm are observable under significant optical and temporal magnification (1000 frames per second). Variation of the catalytic surface between realistic porous foam supports and experimental flat surfaces permits a clear observation of the particle/surface interaction. Additionally, dimensional tracking of particles with time reveals the extent of conversion from solid cellulose to intermediate phases, and it permits an indirect measurement of surface-to-particle heat transfer.

The results show that micron- to millimeter-scale particles decompose to an intermediate liquid droplet before further decomposing and boiling completely to volatile species. The intermediate particle predominately exists as a heterogeneous mixture of solid and liquid with linear reduction in height with respect to time indicating a potential for continuous processing of larger particles. Therefore, additional experiments consider high temperature reforming catalysts in contact with large particles (rods,

7×7×500 mm)that extend away from the surface permitting examination of continuous catalytic processing of cellulose. The processing rate was measured as a function of the interfacial temperature and the applied pressure between the cellulose feedstock and the catalytic surface.

6.2 Experimental

Catalytic reforming of cellulose particles was examined in three separate experimental apparatuses due to the significant difference in cellulose feedstock dimensions (micron- versus centimeter-scale) and catalyst supports (foam versus flat surfaces).

6.2.1 Catalyst Preparation

The catalyst in Fig. 6.1a was supported on an 80 pores per inch (ppi) α-Al_2O_3 foam cylinder 17 mm in diameter and 10 mm in length with visible struts and tortuous pores. The flat catalytic surface (wafer) in Fig. 6.1b was prepared by compressing α-Al_2O_3 powder into a disk 2 mm thick and 22 mm wide, sintering at 800 °C for 30 hrs and 1180 °C for 8 hrs. Both catalysts were prepared by wet impregnation of Rh-Ce (2.5 wt% of the support each), drying, and calcination at 600 °C for 6 hrs.

6.2.2 Micron-Scale Particle Processing on Foam Supports

Small particle (<500 μm) autothermal conversion was examined in a 20 mm I.D. quartz reactor tube described previously.[30] Three foams were stacked on top of each other along with a fourth blank 80 ppi foam on the bottom, wrapped in ceramic paper (for friction fit), and slid into the reactor tube. A type K thermocouple was inserted 10 mm from the leading surface. A 1 cm Pyrex tube combined with a size 20 Pyrex reactor tube end cap provided the connection between the reactor and a cellulose hopper necessary for solid particle delivery. A quartz light pipe was inserted through the end cap and contacted the leading surface providing a light sample to an optical pyrometer. The

cellulose particles (avg. 315 μm) stored in an acrylic tube hopper ($\sim$10 cm diameter) were pushed into a feed tube (0.25 in I.D.) using a 0.25 in wood auger driven in reverse with a servo motor permitting variable feed rates. Air was supplied by a gas cylinder and metered by a flow control valve calibrated with a bubble column.

The quartz reactor was wrapped in a resistive heater controlled by a variac and wrapped in insulation. Autothermal operation was initiated with air flow of 1.5 standard liters per minute (SLPM) by heating the reactor externally to $\sim$400 °C at which point particles were continuously delivered to the surface. Steady autothermal operation was obtained within five minutes, and the heater was turned off. Varying surface temperatures were obtained by varying the air flow rate or cellulose flow rate. The high speed camera was placed $\sim$45° from the surface normal, obtaining light through the curved quartz reactor wall. Light for high-speed photography was provided to the front of the particles. Figure F.1 of Appendix F.1 depicts the experimental setup.

6.2.3 Micron-Scale Particle Processing on Flat Supports

Particles of cellulose and sucrose pyrolyzing on a flat catalytic wafer (Rh-Ce/α-Al_2O_3, 2.5 wt% each) were observed using a high speed camera. A quartz reactor tube was fixed in place 12 cm above the catalytic wafer by metal clamps. Air was supplied by a high pressure gas cylinder through a needle valve, and particles of solid material were applied down the reactor tube to the catalytic surface from a side tube sealed with a pushrod. A quartz fiber light pipe delivering light to an optical pyrometer was attached through the quartz reactor such that it contacted the catalytic surface. A butane torch was clamped directly below the catalytic wafer such that its distance was adjustable to control the surface temperature. The high speed camera was placed $\sim$80° from the surface normal, obtaining light through a flat Pyrex protector plate. Light for high-speed photography was provided from behind the particles. Figure F.8 of the Appendix F.4 depicts the experimental setup.

6.2.4 Centimeter-Scale Particle Processing

Large particles of cellulose (7×7×500 mm) were prepared by pulping a mixture of mainly hemicellulose and cellulose (79.8% glucan, 19.5% xylan, 0.3% lignin, 0.4% ash) in deionized water, drying the pulp in a mold (50×50×1 cm), and cutting the dried block to the desired dimensions.

Processing of large particles occurred on catalytic foams in a 20 mm I.D. reactor described above with the addition of a 1 cm I.D. Pyrex tube extending ∼1 m from the top of the reactor. Cellulose rods were pressed against the catalytic foam from above by weights placed within the sealed tube. The bulk surface temperature was varied from ∼600-900 °C by varying the dilution of methane and oxygen feed gas with the constraint that C/O=(fuel C)/(atomic oxygen from O_2)=0.8 and total gaseous flow rate was 5.0 SLPM. Gaseous reactor effluent was collected and measured by gas chromatography to validate rod conversion rates. Figure F.15 of Appendix F.6 depicts the experimental setup.

Experiments were setup such that a rod of cellulose, 500 mm in length, was suspended 5 cm above the foam catalysts by a pin extending out of the reactor through a sealed port. Nitrogen, oxygen and methane, flowing around the suspended cellulose and through the catalyst, were heated by an external torch applied to the reactor wall near the catalyst to initiate autothermal reforming. The experiment was initiated by removing the pin permitting the cellulose rod to fall to the catalyst surface while simultaneously adjusting the oxygen/nitrogen/methane flow rates to satisfy C/O=0.8. The rate at which the cellulose sample ablated on the catalyst was measured by recording the movement of the cellulose end as it passed graduations on the feed tube with time. Downstream gas samples were collected and analyzed by gas chromatography for carbon monoxide and carbon dioxide to verify carbon processing rates.

6.2.5 High-Speed Photography

Digital video was obtained by focusing a Photron Fastcam Ultima APX with color image through a curved quartz reactor or Pyrex plate. The four optical devices placed in series to obtain the presented magnification were: 1) a Micro-NIKKOR 105 mm lens by Nikon of Japan, 2) a Nikon PN-11 extension tube by Nikon of Japan, 3) a Kenko extension tube for Nikon/AF 36 mm by Kenko of Japan, and 4) a Kenko 2x Teleplus MC7 telephoto extension tube by Kenko of Japan. Light was provided to the catalyst necessary for high speed imaging by a Solarc Light LB- 50 by Welch Allyn, Inc. of New York, USA.

Visualization videos of particle conversion on catalytic foams were collected through the 2 mm thick quartz reactor tube, while particles on wafers were obtained through 0.5 cm Pyrex glass used to protect the camera. Particle sizes were obtained by relating the measured number of pixels within a frame to known sizes of objects (thermocouple or quartz light pipe).

6.3 Results and Discussion

In the integrated pyrolysis/catalysis process examined here, particles of cellulose in air impact a glowing (∼700 °C) Rh-Ce/α-Al_2O_3 foam catalyst in a quartz reactor tube and pyrolyze completely under extreme thermal gradients to VOCs at millisecond time-scales. The VOCs flow into the catalyst, react with oxygen exothermically, and generate sufficient heat to maintain the catalyst at 700-800 °C driving endothermic pyrolysis in an overall exothermic, autothermal process.[30] This arrangement has been shown to efficiently produce equilibrium selectivity to clean synthesis gas without detectable char formation.[77]

Through the use of ultra high-speed imaging (1000 frames per second) we definitively demonstrate the existence of a liquid intermediate during the rapid heating of cellulose particles. Fig. 6.1a shows the conversion of a single ∼300 μm diameter cellulose particle

on an operating foam catalyst at ∼700 °C from ∼45° relative to the catalyst surface. After coming to rest on the surface (0 ms), the particle appears to initially rotate (7 & 30 ms) before the appearance of a smooth liquid layer along the bottom right edge (66 ms) distinguishable by its specular highlight. The development of a liquid phase continues to progress from the bottom of the particle (89 & 107 ms) until the entire particle exists as a hemispherical liquid droplet (121 ms). Clearly visible within the liquid layer are gaseous bubbles developing within the liquid sphere (107, 121, and 130 ms) moving to the surface and eventually the surrounding gas until the entire particle volatilizes leaving a clean surface (171 ms).

In a different experiment (Fig. 6.1b) we examined the impact of cellulose particles in air on a flat Rh-Ce/α-Al_2O_3 surface heated from below by a butane torch to 700 °C. Viewed at 80° from the surface normal, the particle initially exhibits poor surface contact (0-7 ms) before forming a liquid clearly in intimate contact with the catalyst (66-107 ms). Conversion to a liquid at 130 ms produces a hemispherical shape, which fully volatilizes leaving a clean surface at 176 ms.

The existence of a liquid intermediate from cellulose, often referred to as 'active cellulose,' has elicited controversy.[108, 109, 110, 111] Several multi-step cellulose decomposition mechanisms include an intermediate cellulose-like biopolymer of reduced degree of polymerization to fit empirical data.[55, 57, 112, 113] Further depolymerization and fragmentation to organic liquids (e.g. methanol, hydroxyacetaldehyde, levoglucosan) dominates around 500 °C in seconds, while higher temperatures favor gases (e.g. CO, H_2, CO_2) and lower temperatures favor dehydration chemistry to solid char. Previous evidence for depolymerized liquid intermediate formation was observed by showing that cellulose rods, similar to ice or meltable polymers, can be ablated on hot surfaces.[114] A different set of experiments exposed small particles of cellulose to very short durations of applied heat and observed solid products with smooth surfaces, indicative of intermediate liquids.[109, 115] However, the present evidence clearly shows a liquid state forming spherical conformations and interacting with surfaces and other particles.

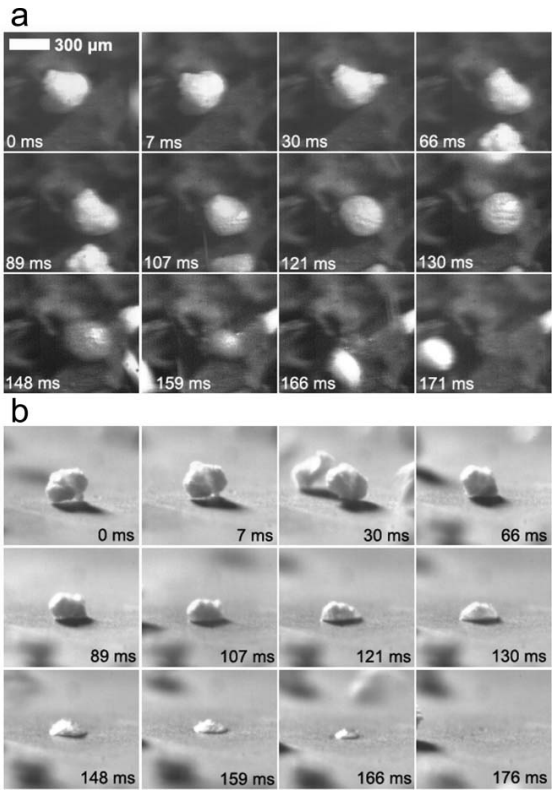

Figure 6.1: Millisecond visualization of cellulose particle decomposition. a) Microcrystalline cellulose particles (∼300 μm) reacting to form volatile species in air on 700 °C Rh-Ce/αAl_2O_3 have been visualized with high-speed photography (1000 frames/second) on an 80 ppi αAl_2O_3 foam support at C/O=1.15. b) A separate experiment examined cellulose decomposition on a smooth 700 °C Rh-Ce/αAl_2O_3 disk support. Particles exhibit poor surface contact (0-7 ms) before forming a liquid intermediate species capable of intimately contacting the catalytic surface (66-176 ms). The molten intermediate liquid appears to nucleate volatile species (107-130 ms) before completely converting without char formation (171-176 ms).

Dimensional tracking of several particles (Fig. 6.2a) on the catalytic foam shows that the conversion time is directly proportional to the square of the initial particle diameter, even for particles as small as 100 μm. Furthermore, measurements shown in Fig. 6.2b (height and width) depict the lifetime of both particles in Fig. 6.1 and reveal three stages in particle volatilization. In region A, the particle exhibits poor surface contact and no apparent change in size. In region B, intermediate liquid formation propagates up the particle, coinciding with a nearly linear reduction in height. Finally, in region C, the liquid droplet undergoes further pyrolysis to gases and volatile organics, exhibiting constant decrease in width and volume as shown in Figure F.11 of the Appendix F.4.

The nature of the intermediate liquid has enormous implications on the rate of heat transfer from catalytic surfaces for thermal conversion of cellulosic materials. Particle pyrolysis is categorized in two ways, according to the dominant mode of heat transfer (internal or external) and the rate limiting phenomenon (chemical conversion by pyrolysis, product gas mass transfer or heat transfer).[116] In this case, the thermal decomposition chemistry of cellulose above 400 °C is sufficiently fast to never be rate limiting for particles on the order of ten microns and larger.[61, 117] Additionally, the chemistry observed in Fig. 6.1 and the data in Fig. 6.2b clearly shows that solid to intermediate liquid conversion dominates the conversion time eliminating gas phase product mass transfer from being rate limiting. Therefore, conversion can only be limited by heat transfer to the particle by radiation, convection, conduction from the surface, or internal particle heat transfer (Fig. 6.2a).

The behavior of total conversion time as directly proportional to the square of the initial diameter has previously indicated internal heat transfer limitation, thereby requiring the ratio of external to internal heat transfer (described by the Biot number, Bi=hD/k) to be large (Bi>10) where k is the thermal conductivity of cellulose, D is the particle diameter, and h is the external heat transfer coefficient.[111, 118] Neither maximum radiation, ϵ=1 and T_{inf}=700 °C (10^{-2}<$Bi_{radiation}$<10^{-1}), nor gas convection calculated from the Ranz and Marshall correlation ($Bi_{convection}$∼1) are sufficiently large

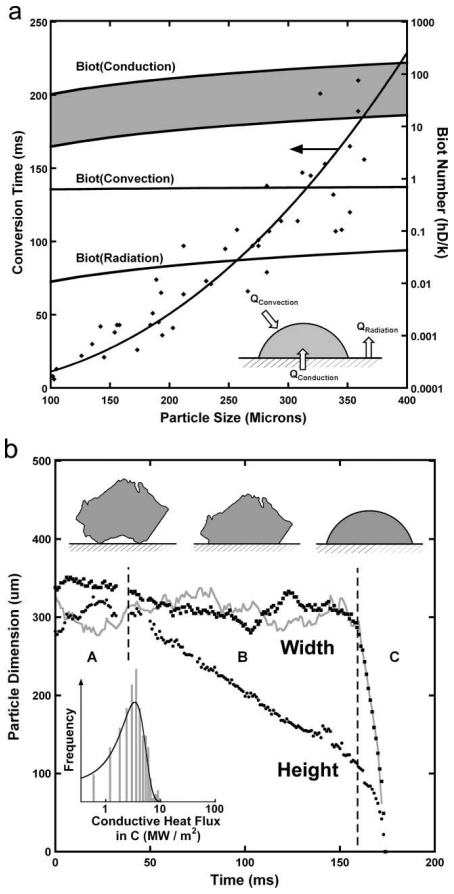

Figure 6.2: Dimensional tracking of cellulose particle conversion for surface heat flux estimation. a) The time for observed particles to completely convert was proportional to the square of the initial particle diameter (T_c=kD_o^2) consistent with internal particle heat transfer control thereby requiring the ratio of external to internal heat transfer (Biot Number) to be larger than ∼10. Only a conductive heat transfer coefficient of h=10^4-10^5 W m^{-2} K^{-1} (shaded region) can result in a Biot>>1 describing the thermal and reacting wave observed in Fig. 6.1. b) The conversion of a single cellulose particle (∼300 μm) on a 700 °C surface appears to occur in three phases (A, B, and C) shown as a cartoon and described by height and width for flat surfaces (data points) and foams (grey line). (A) Initial impact with a catalytic surface exhibits very poor surface contact and slow initial heating. (B) Particle surface contact points eventually pyrolyze to a biopolymer liquid (active cellulose) which can contact the surface and permit rapid pyrolysis with a linear decrease in height. Gas nucleation was observed in the height around 140-150 ms. (C) An active cellulose drop exhibits linear decrease in volume (and radius of curvature) with time and an enormous heat flux of 3.4±0.2 MW m^{-2} (inset).

to limit the system by internal particle heat transfer.[119] External heat transfer from the surface by conduction can be estimated from Eqn. 6.1.

$$q_{conduction} = \rho \frac{dV}{dt} \frac{\Delta H_{pyrolysis}}{A_{contact}} = h_{conduction} \left(\Delta T\right) \tag{6.1}$$

The volume of the liquid droplet, V, in each frame was calculated by assuming the droplet was a portion of a sphere as described in Appendix F.4. This method reveals that the change in volume, dV/dt, of the liquid droplet (Fig. 6.2, region C) is constant as shown in Figure F.11 of Appendix F.4. By calculating dV/dt from ∼200 measurements of several particles (Fig. 6.2, region C) and assuming $\Delta H_{pyrolysis}$=538 kJ kg^{-1}, ρ=650 kg m^{-3}, the heat flow, $q_{conduction}$, is 3.4±0.2 MW m^{-2} as shown by a histogram in the Fig. 6.2b inset of all experimental measurements.[120] Further assuming the intermediate liquid is approximately the fusion temperature described by Lede (739 K), then ΔT∼200 °C, and $h_{surface}$ must be (1.7±0.1)×10^4 W m^{-2} K^{-1}, satisfying Bi∼10 and concluding that surface heat transfer is overwhelming and dominant.[114] Convection and radiation are included by this method of estimating the heat transfer rate, but their magnitude is on the order of the experimental error or less.

The mechanism permitting high conductive heat transfer to the particle can be observed in Fig. 6.1. Droplets of volatile fluids such as glycerol, heptane, or dodecane commonly exhibit film boiling (the Leidenfrost effect) which lift them off very hot surfaces, slowing conductive heat transfer.[121, 122] However, experiments with cellulose (and additional experiments with sucrose) show that the liquid intermediate on a ∼700 °C catalytic surface maintains contact, dramatically improving conductive heat transfer to the particle.

High heat flux through an intermediate liquid species has unique implications for the chemistry of cellulose decomposition. As observed in Fig. 6.1, cellulose conversion occurs as a thermal wave passing through the particle. For small particles considered here (<500 μm), no portion of the particle exists sufficiently long at low temperature (∼300-400 °C) for char forming chemistry to occur appreciably. However, as a particle

increases in size to 1 mm or greater (e.g. wood chips), it becomes unavoidable that a portion of the solid biopolymer away from the hot surface will exist within the char-producing temperature range. One demonstrated solution to this fundamental problem utilizes high heat transfer rates between a large (thermally thick) particle and a hot non-catalytic surface moving relative to the sample to mechanically sweep away pyrolysis products.[64, 123, 124] However, more simple processing of cellulose can occur with a stationary surface utilizing a catalyst on a porous surface.

A different experiment with cellulose (Fig. 6.3a) demonstrates that high heat flux through the liquid intermediate on catalytic surfaces can also process (7×7×500 mm) rods rapidly. By pressing a cellulose rod directly onto a Rh-Ce/Al_2O_3 foam co-reforming methane, the rate of cellulose pyrolysis was measured as a function of applied pressure (12-36 kPa) and bulk catalyst surface temperature. Below a surface temperature of about 750 °C, the rod exhibited the expected behavior of intermediate char formation which permitted the rod to pass through the catalyst only as fast as the intermediate char gasification rate, ∼50 kg m^{-2} hr^{-1}. However, above approximately 750 °C, the rod processing rate was considerably higher (>300 kg m^{-2} hr^{-1}), linear in temperature, and a strong function of applied pressure, indicating that pyrolysis at the leading cellulose edge is the rate limiting step.[60]

Fig. 6.3b describes a qualitative temperature distribution consistent with experimental observations. As heat flow from the surface (Q_{flux}) increases, the thermal gradient within the solid cellulose particle increases and the length of cellulose ('a' in Fig. 6.3b) existing within the char-forming temperature region decreases ('b' in Fig. 6.3b). At heat fluxes present in the described experiments, the thermal gradient within the cellulose rod is sufficiently steep to result in negligible char formation.

The decomposition of cellulose at the rod tip in contact with the catalytic surface likely undergoes very complex multiphase rearrangement. As solid cellulose decomposes to intermediate liquid, it is pushed into the pores of the catalyst. Additionally, individually developed fluid droplets are likely to coalesce to larger ones.

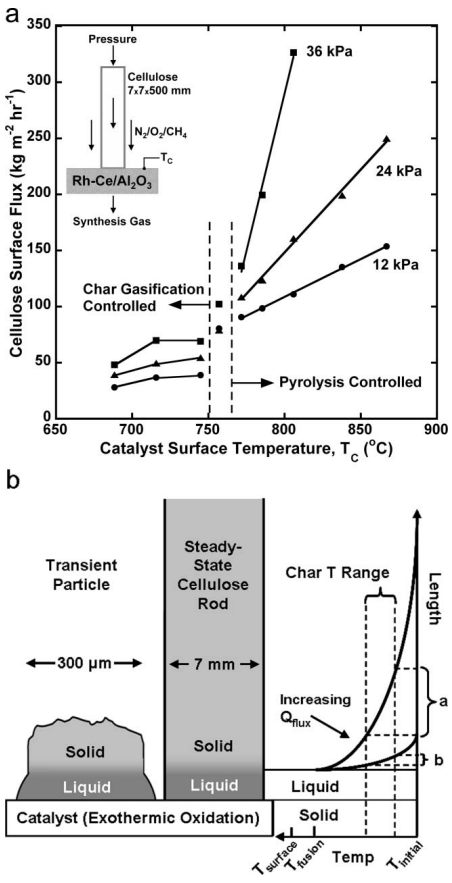

Figure 6.3: Large particle conversion on catalytic surfaces. a) Cellulose particles (7×7×500 mm) reacted to synthesis gas on a Rh-Ce coated alumina foam by direct impingement in the presence of oxygen. The interface pressure was varied from 12-36 kPa, and the catalyst surface temperature was controlled by methane catalytic partial oxidation at C/O=0.8 diluted with varying amounts of N_2 (total gas flow rate was a constant 5 SLPM). Cellulose conversion exhibited a distinct change in conversion rate (surface flux) between the char gasification rate control and linear pyrolysis rate control around 750 °C. Error bars (not shown) of ±21 kg m^{-2} hr^{-1} represent a 95% confidence interval. b) The form of the cellulose temperature profile is depicted as a function of the rod length. As heat flux, Q_{flux}, from the catalyst through cellulose increases, the thermal gradient increases (becomes sharper). At high heat flux from the surface, Q_{flux}, the sharp temperature gradient permits very little (length b) of the extended cellulose rod to exist within the char-forming temperature range (∼300-400 °C). However, as $T_{surface}$ decreases below ∼750 °C, Q_{flux} decreases and more of the extended rod (length a) forms char such that char removal by gasification becomes the rate-limiting process.

This phenomenon has been observed on catalyst foams when two small particles, each ∼300 μm, come to rest near each other and decompose to an intermediate liquid during the same period of time as shown in Fig. 6.4. Within 80 ms of the first particle landing, the particle on the right is fully liquid and the particle on the left is mostly liquid. Within a few milliseconds, the two liquid droplets combine to form a single particle. The most violent motion forming the bridge between the two particles occurs faster than a single millisecond and can only be inferred from the frames and video. The combined particle continues to form a spherical shape in the next 25 ms before completely volatilizing at 180 ms.

The existence of a processing regime capable of combining pyrolysis of biomass particles with catalysis facilitates the development of new reactor designs and chemistries. Many of the conclusions developed here regarding the liquid intermediate, high heat transfer rates, and large particle processing can be extended to previous non-catalytic biomass reactors (e.g. biomass ablative vortex reactor).[125] Additionally, new combinations of pyrolysis and catalysis become more viable, including mixed pyrolysis/ hydrogenation, pyrolysis/hydrodeoxygenation, or pyrolysis/cracking. However, additional research will be required to more fully describe the solid-nonvolatile fluid heat transfer mechanism as well as the operating parameters that control the large particle regime transition.

6.4 Conclusions

High speed photography reveals that direct impingement of microcrystalline cellulose particles with Rh-based reforming catalysts at 700 °C produces an intermediate liquid phase that reactively boils to vapors. The intermediate liquid maintains contact with the catalyst surface permitting high heat transfer (3.4 MW m^{-2}) generating an internal thermal gradient visible within the particle as a wave of solid to liquid conversion. During the period of solid to liquid conversion, the particle height decreased linearly

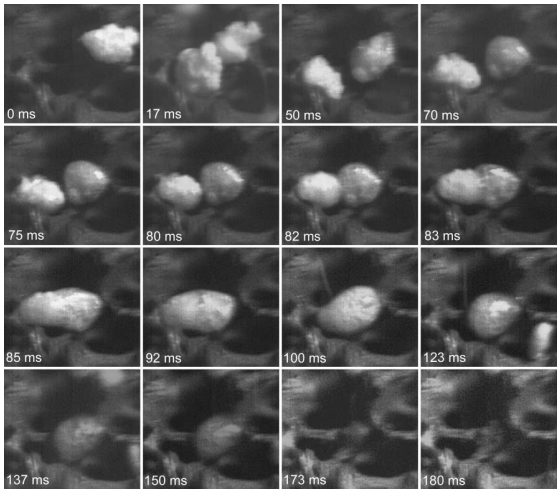

Figure 6.4: Millisecond coalescence of cellulose intermediate liquid droplets. Two microcrystalline cellulose particles ($\sim$300 μm each) reacting to volatile species in air on 700 °C Rh-Ce/αAl_2O_3 surface have been observed with high-speed photography on an 80 ppi α-Al_2O_3 foam support at C/O=1.15 from 45° from the surface normal with temporal resolution of one millisecond. Two particles (coming to rest at 0 and 17 ms) convert to a liquid. The liquid droplets coalesce rapidly (82-85 ms) to a single particle which reactively boils to volatile species observable as gaseous bubbles (100-137 ms) leaving a clean surface (180 ms).

with time. Complete conversion to liquid yields a fluid droplet on the catalyst surface exhibiting linear decrease in droplet volume with time leaving behind a clean surface absent solid residue (char). Under specific interfacial conditions, conversion with large cellulosic particles on the length-scale of wood chips occurs continuously as generated liquid and vapors are pushed into the porous surface.

6.5 Acknowledgements

We acknowledge funding from the U.S. Department of Energy and the Initiative for Renewable Energy and the Environment (IREE) at the University of Minnesota. We also acknowledge assistance from Professor Ulrike Tschirner in preparing and analyzing cellulose samples. We also thank Jennifer Dederich for photographic assistance.

Chapter 7

Summary and Future Directions

7.1 Summary

The global energy market currently supplies roughly 12 terawatts for human consumption annually, equivalent to a continuous demand of 2,000 barrels of oil every second.[3, 4] Liquid hydrocarbons are appealing for their extremely high energy density and ease of storage. Collectively, these characteristics are unique to carbon-rich liquid fuels currently produced almost entirely from oil. Biomass, the only source of renewable carbon, represents the only sustainable feedstock for the production of carbon-rich fuels referred to as 'biofuels'. Currently three primary routes exist for the production of liquid fuels from biomass: 1) biological routes for liquid fuel production, 2) fast pyrolysis for the production of bio-oil, and 3) gasification of biomass to synthesis gas for use as a heating gas or for further upgrading to liquid fuels. This thesis examined the use of catalytic partial oxidation to improve on traditional biomass gasification technologies, which are hindered by tar formation, carbon formation, sensitivity to water, and poor carbon utilization, making them inefficient on the small scales needed for biomass processes.

Results in Chapters 3 and 4 examined the ability of the catalytic partial oxidation process to convert solid biomass feedstocks to a clean synthesis gas stream, focusing

on overall process performance. Rh-based catalysts were shown to convert cellulose to a thermodynamic equilibrium synthesis gas stream at ∼30 ms contact times. No carbon, char, or undesired tar products were observed during steady-state operation, eliminating a number of the major technical barriers hindering commercialization efforts of traditional gasification reactors. It was also shown that by co-feeding steam to the process the H_2/CO ratio in the product stream could be adjusted anywhere between 1 and 3. The ability to adjust this ratio is important when the synthesis gas is to be used as a feedstock for the production of liquid fuels. Additionally, up to 50 wt% steam was co-fed with cellulose in the CPO process feed, demonstrating the systems ability to handle wet biomass feedstocks. Alternatively, by co-feeding hydrogen rich fuels with cellulose it was shown that the yield of CO could be improved, reducing the amount of carbon lost as undesired CO_2 and solid carbon. Under certain experimental conditions it was shown that 100% of carbon in the fuel feed could be converted to CO.

Results in Chapters 5 and 6 examined the mechanism by which biomass feedstocks are converted to synthesis gas in the catalytic partial oxidation process. Starting at the point of initial biomass contact with the catalyst, Chapter 6 examined the devolatilization of solid biomass particles to volatile organic compounds upon contacting the hot catalyst surface. The formation of a liquid intermediate before complete cellulose devolatilization was demonstrated conclusively for the first time under high heat fluxes. The high heat fluxes present when the cellulose particles make intimate contact with the hot catalyst surface are adequate to select for pyrolysis chemistry, essentially eliminating the formation of undesired char byproducts through dehydration reactions. The volatile organic compounds produced from cellulose decomposition are then convected into the catalyst bed where they undergo rapid oxidation on the Rh surface, providing the heat necessary to power endothermic pyrolysis and reforming reactions upstream and downstream of the oxidation zone, respectively. Any volatile organic compounds remaining after complete consumption of oxygen undergo reforming and water-gas-shift reactions in the reforming zone of the catalyst. This section of the catalyst, examined

in depth in Chapter 5 drives the system rapidly to thermodynamic equilibrium.

This thesis showed that by applying the catalytic partial oxidation process to biomass gasification high efficiencies can be realized even at small scales through heat integration and the use of Rh based catalysts. Such a technology could substantially improve gasification process economics by reducing both capital and operating costs.

7.2 Future Directions

The findings in this thesis have elucidated the existence of two related areas where further research is necessary: 1) the modeling of solid biomass particle decomposition and volatilization when in contact with a hot catalytic surface, and 2) the effect of biomass derived inorganic compounds on the performance of catalysts used in the catalytic partial oxidation process. Research in these areas could help improve the understanding and performance of the catalytic partial oxidation process, as well as other thermochemical biomass processes.

7.2.1 Biomass Particle Volatilization Model

The first step in converting biomass to pyrolysis or gasification products is decomposing the solid to volatile compounds. Many models have been developed to describe thermal biomass particle decomposition. These models primarily consider the influence of particle size, geometry, and rate of heat transfer on particle volatilization rate and product yields. Existing models use global reaction pathways to reduce the complexity of the system, which can generate 400 different intermediate compounds. These models generally include permanent gases, VOC's (also referred to as 'tars'), and char as the intermediate and final products.

Current models generally lack adequate experimental data necessary for model validation. Data presented in Chapter 6 of this thesis represents the state of the art in experimental biomass volatilization information. Using high speed photography, high

resolution images were obtained accurately describing the volatilization of cellulose and lignocellulosic particles when placed in intimate contact with hot surfaces.

Using the information presented in Chapter 6, an improved model can be developed that more accurately describes the conversion of cellulose and lignocellulosic biomass to product compounds. These models can then be used to determine ideal conditions for biomass devolatilization during thermochemical biomass conversion processes.

7.2.2 Effect of Biomass-Derived Inorganics on Rh-based Catalysts

Catalyst deactivation by inorganic components of biomass, generally referred to as "ash", remains one of the key challenges facing commercialization of catalyst based biomass gasifier systems. It is important to examine the effect of these inorganics on Rh-based catalytic partial oxidation catalysts. The key inorganic impurities that warrant in depth examination include Si, Ca, Mg, K, Na, P, Cl, and S.

In order to determine the effect of ash on catalyst activity, it is important to perform in depth performance testing and catalyst characterization comparing clean catalysts to catalysts that have been exposed to inorganic compounds typically found in biomass feedstocks. An initial survey determining the effect of common biomass-derived inorganics on catalyst performance gives significant insight into whether or not each inorganic will deactivate Rh-based catalysts.

Upon determining which inorganic impurities effect catalyst performance, in depth characterization must be performed to determine the mode of catalyst deactivation. More specifically, a combination of x-ray diffraction, x-ray photoelectron spectroscopy, scanning electron microscopy, and chemisorption can be used to determine whether the catalyst is being fouled (physically covered by the inorganic impurities) or deactivated by electronic interactions between the inorganic impurity and the Rh active sites.

Determining a list of inorganics that can effect CPO catalyst performance is important for determining ideal biomass feedstocks and assessing the overall process feasibility. Examining the mode of catalyst deactivation is important for designing catalysts

resistant to rapid deactivation.

Bibliography

[1] A.V. Bridgwater. Renewable fuels and chemicals by thermal processing of biomass. *Chemical Engineering Journal*, 91:87–102, 2003.

[2] C. Schubert. Can biofuels finally take center stage? *Nature Biotechnology*, 24:777–784, 2006.

[3] V.B.N. Armaroli. The future of energy supply: Challenges and opportunities. *Angewandte Chemie*, 46:52–66, 2007.

[4] C. Somerville. Biofuels. *Current Biology*, 17:115–119, 2007.

[5] Energy Information Administration. Forecasting. Technical report, U.S. Department of Energy, Washington D.C., 2006.

[6] EcoSystems. The coming global oil crisis. Technical report, Ecotopia, Santa Cruz, 2007.

[7] G.W. Huber, S. Iborra, and A. Corma. Synthesis of transportation fuels from biomass: Chemistry, catalysts, and engineering. *Chemical Reviews*, 106:4044–4098, 2006.

[8] C.M. Hamelinck and A.P.C. Faaij. Future prospects for production of methanol and hydrogen from biomass. *Journal of Power Sources*, 111:1–22, 2002.

[9] R.R. Davda, J.W. Shabaker, G.W. Huber, R.D. Cortright, and J.A. Dumesic. A review of catalytic issues and process conditions for renewable hydrogen and alkanes by aqueous-phase reforming of oxygenated hydrocarbons over supported metal catalysts. *Applied Catalysis B*, 56:171–186, 2005.

[10] M.J.A. Tijmensen, A.P.C. Faaij, C.N. Hamelinck, and M.R.M. can Hardeveld. Exploration of the possibilities for production of Fischer Tropsch liquids and power via biomass gasification. *Biomass and Bioenergy*, 23:129–152, 2002.

[11] S. Satyapal, J. Petrovic, C. Read, G. Thomas, and G. Ordaz. The U.S. department of energy's national hydrogen storage project: Progress towards meeting hydrogen-powered vehicle requirements. *Catalysis Today*, 120:246–256, 2006.

[12] R.D. Perlack, L.L. Wright, A.F. Turhollow, R.L. Graham, B.J. Stokes, and D.C. Erbach. Biomass as feedstock for a bioenergy and bioproducts industry: The technical feasibility of a billion-ton annual supply. Technical report, United States Department of Energy, Oak Ridge National Laboratory, Oak Ridge, TN, USA, DOE/GO-102005-2135, 2005.

[13] A. Corma, G.W. Huber, L. Sauvanaud, and P. O'Connor. Processing biomass-derived oxygenates in the oil refinery: Catalytic cracking (FCC) reaction pathways and role of catalyst. *Journal of Catalysis*, 247:307–327, 2007.

[14] M.F. Demirbas. Current technologies for biomass conversion into chemicals and fuels. *Energy Sources*, 28:1181–1188, 2006.

[15] G. Solomons and C. Fryhle. *Organic Chemistry*. John Wiley & Sons, NY, 2000.

[16] B. Monties. Plant cell walls as fibrous lignocellulosic composites: Relations with lignin structure and function. *Animal Feed Science and Technology*, 32:159–175, 1991.

[17] D.J. Cosgrove. Growth of the plant cell wall. *Nature Reviews: Molecular Cell Biology*, 6:850–861, 2005.

[18] K. Sanderson. Biofuels: A field in ferment. *Nature*, 444:673–676, 2006.

[19] Y. Lin and S. Tanaka. Ethanol fermentation from biomass resources: Current state and prospects. *Applied Microbiology & Biotechnology*, 69:627–642, 2006.

[20] C.S. Gong, J. Du, and G.T. Tsao. *Advances In Biochemical Engineering Biotechnology*. Springer-Verlag, Berlin, 1999.

[21] D. Mohan, C.U. Pittman, and P.H. Steele. Pyrolysis of wood/biomass for bio-oil: A critical review. *Energy and Fuels*, 20:848–889, 2006.

[22] Q. Zhang, J. Chang, T. Wang, and Y. Xu. Review of biomass pyrolysis oil properties and upgrading research. *Energy Conversion and Management*, 48:87–92, 2007.

[23] T.A. Milne and R.J. Evans. Biomass gasifier 'tars': Their nature, formation, and conversion. Technical report, U.S. Department of Energy, National Renewable Energy Laboratory, Golden, CO, USA, NREL/TP-570-25357, 1998.

[24] P.L. Spath. Preliminary screening–technical and economic assessment of synthesis gas to fuels and chemicals with emphasis on the potential for biomass-derived syngas. Technical report, National Renewable Energy Laboratory, Golden CO, 2003.

[25] R. Horn, K.A. Williams, N.J. Degenstein, A. Bitsch-Larsen, D. Dalle Nogare, S.A. Tupy, and L.D. Schmidt. Methane catalytic partial oxidation on autothermal Rh and Pt foam catalysts: Oxidation and reforming zones, transport effects, and approach to thermodynamic equilibrium. *Journal of Catalysis*, 249:380–393, 2007.

[26] R. Horn, N.J. Degenstein, K.A. Williams, and L.D. Schmidt. Spatial and temporal profiles in millisecond partial oxidation processes. *Catalysis Letters*, 110:169–178, 2006.

[27] G.A. Deluga, J.R. Salge, L.D. Schmidt, and X.E. Verykios. Renewable hydrogen from ethanol by autothermal reforming. *Science*, 303:993–997, 2004.

[28] P.J. Dauenhauer, J.R. Salge, and L.D. Schmidt. Renewable hydrogen by autothermal steam reforming of volatile carbohydrates. *Journal of Catalysis*, 244:238–247, 2006.

[29] J.R. Salge, B.J. Dreyer, P.J. Dauenhauer, and L.D. Schmidt. Renewable hydrogen from nonvolatile fuels by reactive flash volatilization. *Science*, 314:801–804, 2006.

[30] P.J. Dauenhauer, B.J. Dreyer, N.J. Degenstein, and L.D. Schmidt. Millisecond reforming of solid biomass for sustainable fuels. *Angewandte Chemie*, 46:5864–5867, 2007.

[31] J.B. Claridge. A study of carbon deposition on catalysts during the partial oxidation of methane to synthesis gasification. *Catalysis Letters*, 244:299–305, 1993.

[32] G.I. Garrido, F.C. Patcas, S. Lang, and B. Kraushaar-Czarnetzki. Mass transfer and pressure drop in ceramic foams: A description for different pore sizes. *Chemical Engineering Science*, 63:5202–5217, 2008.

[33] A.S. Bodke, S.S. Bharadwaj, and L.D. Schmidt. The effect of ceramic supports on partial oxidation of hydrocarbons over noble metal coated monoliths. *Journal of Catalysis*, 179:138–149, 1998.

[34] C. Wheeler, A. Jhalani, E.J. Klein, S. Tummala, and L.D. Schmidt. The water-gas-shift reaction at short contact times. *Journal of Catalysis*, 223:191–199, 2004.

[35] A.J. Ragauskas, C.K. Williams, B.H. Davison, G Britovsek, J Cairney, C.A. Eckert, W.J. Frederick, J.P. Hallett, D.J. Leak, C.L. Liotta, J.R. Mielenz, R. Murphy,

R. Templer, and T. Tschaplinski. The path forward for biofuels and biomaterials. *Science*, 311:484–489, 2006.

[36] S. Phillips, A. Aden, J. Jechura, D. Dayton, and T. Eggeman. Thermochemical ethanol via indirect gasification and mixed alcohol syntehsis of lignocellulosic biomass. Technical report, U.S. Department of Energy, National Renewable Energy Laboratory, Golden, CO, USA, NREL/TP-510-41168, 2007.

[37] J.R. Rostrup-Nielsen. Syngas in perspective. *Catalysis Today*, 71:243–247, 2002.

[38] C.N. Hamelinck, A.P.C. Faaij, H. den Uil, and H. Boerrigter. Production of FT transportation fuels from biomass: Technical options, process analysis and optimization, and development potential. *Energy*, 29:1743–1771, 2004.

[39] J.P. Ciferno and J. Marano. Benchmarking biomass gasification technologies for fuels. Technical report, National Energy Technology Laboratory, US Department of Energy, Pittsburgh, PA, USA, 2002.

[40] K. Tomishige, M. Asadullah, and K. Kunimori. Syngas production by biomass gasification using $Rh/CeO_2/SiO_2$ catalysts and fluidized bed reactor. *Catalysis Today*, 89:389–403, 2004.

[41] P. Lv, Z. Yuan, C. Wu, L. Ma, Y. Chen, and N. Tsubaki. Bio-syngas production from biomass catalytic gasification. *Energy Conversion Management*, 48:1132–1139, 2007.

[42] K. Tasaka, T. Furusawa, and A. Tsutsumi. Biomass gasification in fluidized bed reactor with Co catalysts. *Chemical Engineering Science*, 62:5558–5563, 2007.

[43] M. Asadullah, S. Ito, K. Kunimori, M. Yamada, and K. Tomishige. Biomass gasification to hydrogen and syngas at low temperature: Novel catalytic system using fluidized-bed reactor. *Journal of Catalysis*, 208:255–259, 2002.

[44] K. Tomishige, T. Miyazawa, M. Asadullah, S. Ito, and K. Kunimori. Catalyst performance in reforming of tar derived from biomass over noble metal catalysts. *Green Chemistry*, 5:399–403, 2003.

[45] M. Asadullah, K. Tomishige, and K. Fujimoto. A novel catalytic process for cellulose gasification to synthesis gasification. *Catalysis Communications*, 2:63–68, 2001.

[46] A. Roine. Outokumpu HSC Chemistry for Windows Ver. 4.0. Technical report, Outokupu Research Oy, Pori, Finland, 2007.

[47] M.J. Moran. Availability analysis: A guide to efficient energy use. *ASME Press, New York*, 1989.

[48] J. Szargut and T. Styrylska. Approximate evaluation of the exergy of fuels. *Waerme Kraft*, 16:589–596, 1964.

[49] M. Dietenberger. Update for combustion properties of wood componenets. *Fire Materials*, 26:255–267, 2002.

[50] S.R.F. Probstein and R.E. Hicks. Synthetic fuels. *Dover Publication Inc, Mineaola N.Y.*, 2006.

[51] K.J. Ptasinski, M.J. Prins, and A. Pierik. Exergetic evaluation of biomass gasification. *Energy*, 32:568–574, 2007.

[52] Y.B. Yang, V.N. Sharifi, J. Swithenbank, L. Ma, L.I. Darvell, J.M. Jones, M Pourkashanian, and A. Williams. Combustion of a single particle of biomass. *Energy & Fuels*, 22:306–316, 2008.

[53] A.B. Mhadeshwar and D.G. Vlachos. Hierarchical multiscale mechanism development for methane partial oxidation and reforming and for thermal decomposition of oxygenates on $Rh/CeO_2/SiO_2$. *Journal of Physical Chemistry B*, 109:16819–16835, 2005.

[54] C. Di Blasi. Comparison of semi-global mechanisms for primary pyrolysis of lignocellulosic fuels. *Journal of Analytical and Applied Pyrolysis*, 47:43–64, 1998.

[55] A.G.W. Bradbury, Y. Sakai, and F. Shafizadeh. A kinetic model for pyrolysis of cellulose. *Journal of Applied Polymer Science*, 23:3271–3280, 1979.

[56] A.G. Liden, F. Berruti, and D.S. Scott. A kinetic model for the production of liquids from the flash pyrolysis of biomass. *Chemical Engineering Communications*, 65:207–221, 1988.

[57] J.P. Diebold. A unified, global model for the pyrolysis of cellulose. *Biomass Bioenergy*, 7:75–85, 1994.

[58] Jr. M.J. Antal and G. Varhegyi. Cellulose pyrolysis kinetics: The current state of knowledge. *Industrial and Chemical Engineering Research*, 34:703–717, 1995.

[59] J.G. Reynolds and A.K. Burnham. Pyrolysis decomposition kinetics of cellulose-based materials by constant heating rate micropyrolysis. *Energy & Fuels*, 11:88–97, 1997.

[60] C. Di Blasi. The state of the art of transport models for charring solid degradation. *Polymer International*, 49:1133–1146, 2000.

[61] A.M.C. Janse, R.W.J. Westerhout, and W. Prins. Modeling of flash pyrolysis of a single wood particle. *Chemical Engineering Processes*, 39:239–252, 2000.

[62] D.R. Soravia and P. Canu. Kinetic modeling of cellulose fast pyrolysis in a flow reactor. *Industrial and Chemical Engineering Research*, 41:5990–6004, 2002.

[63] L.J. Curtis and D.J. Miller. Transport model with radiative heat transfer for rapid cellulose pyrolysis. *Industrial and Chemical Engineering Research*, 27:1775–1783, 1988.

[64] C. Di Blasi. Heat transfer mechanisms and multi-step kinetics in the ablative pryrolysis of cellulose. *Chemical Engineering Science*, 51:2211–2220, 1996.

[65] M. Garcia-Perez, A. Chaala, H. Pakdel, D. Kretschmer, and C. Roy. Characterization of bio-oils in chemical families. *Biomass and Bioenergy*, 31:222–242, 2007.

[66] D.C. Rennard, P.J. Dauenhauer, Sarah A. Tupy, and Lanny D. Schmidt. Autothermal catalytic partial oxidation of bio-oil functional groups: Esters and acids. *Energy & Fuels*, 22:1318–1327, 2008.

[67] S. Wang, T. Ishihara, and Y. Takita. Partial oxidation of dimethyl ether over various supported metal catalysts. *Applied Catalysis A*, 228:167–176, 2002.

[68] C. Rioche, S. Kulkarni, F.C. Meunier, J.P. Breen, and R. Burch. Steam reforming of model compounds and fast pyrolysis bio-oil on supported noble metal catalysts. *Applied Catalysis B*, 61:130–139, 2005.

[69] R. Horn, K.A. Williams, N.J. Degenstein, and L.D. Schmidt. Syngas by catalytic partial oxidation of methane on rhodium: Mechanistic conclusions from spatially resolved measurements and numerical simulations. *Journal of Catalysis*, 242:92–102, 2006.

[70] M. Mittal and B.K. Guha. Minimum ignition temperature of polyethylene dust: A theoretical model. *Fire Materials*, 21:169–177, 1997.

[71] X. Xiaoding and J.A. Moulijn. Mitigation of co_2 by chemical conversion: Plausible chemical reactions and promising products. *Energy & Fuels*, 10:305–325, 1996.

[72] R. Shinnar and F. Citro. A road map to U.S. decarbonization. *Science*, 313:1243–1244, 2006.

[73] R. Agrawal, N.R. Singh, F.H. Ribeiro, and W.N. Delgass. Sustainable fuel for the transportation sector. *Proceedings of the National Academy of Sciences*, 104:4828–4833, 2007.

[74] D. Hildebrandt, D. Glasser, B. Hausberger, B. Patel, and B.J. Glasser. Producing transportation fuels with less work. *Science*, 323:1680–1681, 2009.

[75] B.C. Gates, G.W. Huber, C.L. Marshall, P.N. Ross, J. Siirola, and Y. Wang. Catalysts for emerging energy applications. *MRS Bulletin*, 33:429–435, 2008.

[76] R. Agrawal and N.R. Singh. Synergistic routes to liquid fuel for a petroleum-deprived future. *AIChE Journal*, 55:1898–1905, 2009.

[77] J.L. Colby, P.J. Dauenhauer, and L.D. Schmidt. Millisecond autothermal steam reforming of cellulose for synthetic biofuels by reactive flash volatilization. *Green Chemistry*, 10:773–783, 2008.

[78] A. Donazzi, B.C. Michael, and L.D. Schmidt. Chemical and geometric effects of Ce and washcoat addition on catalytic partial oxidation of CH_4 on Rh probed by spatially resolved measurements. *Journal of Catalysis*, 260:270–275, 2008.

[79] P.J. Dauenhauer, J.L. Colby, C.M. Balonek, and L.D. Schmidt. Reactive boiling of cellulose for integrated catalysis through an intermediate liquid. *Green Chemistry*, 11:1555, 2009.

[80] D.A. Hickman and L.D. Schmidt. Production of syngas by direct catalytic oxidation of methane. *Science*, 259:343–346, 1993.

[81] A.K. Rajvanshi. *Alternative Energy in Agriculture*. CRC Press, 1986.

[82] D.A. Dayton. A review of the literature of catalytic biomass tar destruction. Technical report, NREL/TP-510-32815; National Renewable Energy Laboratory (NREL) Technical Report: Golden, CO, 2002.

[83] A.V. Bridgwater. The technical and economic feasibility of biomass gasification for power generation. *Fuel*, 74:631–653, 1995.

[84] M.M. Yung, W.S. Jablonski, and K.A. Magrini-Bair. Review of catalytic conditioning of biomass-derived syngas. *Energy & Fuels*, 23:1874–1887, 2009.

[85] L. Garcia, M.L. Salvador, J. Arauzo, and R. Bilbao. Conference communication. *Proceedings of the 3rd Biomass Conference of the Americas*, pages 373–382, 1997.

[86] J. Arauzo, D. Radlein, D. Piskorz, and D.S. Scott. Catalytic pyrogasification of biomass. Evaluation of modified nickel catalysts. *Industrial and Chemical Engineering Research*, 36:67–75, 1997.

[87] E.G. Baker, M.D. Brown, and R.J. Robertus. Catalytic gasification of bagasse for the production of methanol. Technical report, PNL-5100; Pacific Northwest National Laboratory (PNNL) Technical Report: Richland, WA, 1985.

[88] R. Coll, J. Salvado, X. Farriol, and D. Montane. Steam reforming model compounds of biomass gasification tars: conversion at different operating conditions and tendency towards coke formation. *Fuel Processing Technologies*, 74:19–31, 2001.

[89] M. Maestri, D.G. Vlachos, A. Beretta, G. Groppi, and E.J. Tronconi. Steam and dry reforming of methane on Rh: Microkinetic analysis and hierarchy of kinetic models. *Journal of Catalysis*, 259:211–222, 2008.

[90] J.S. Church and N.W. Cant. Stabilization of aluminas by rare earth and alkaline earth ions. *Applied Catalysis A*, 101:105–116, 1993.

[91] J.M. Schwartz and L.D. Schmidt. Microstructures of platinum-cerium and rhodium-cerium particles on alumina and silica. *Journal of Catalysis*, 138:283–293, 1992.

[92] T. Maillet, Y. Madier, R. Taha, J. Barbier, and D. Duprez. Spillover of oxygen species in the steam reforming of propane on ceria-containing catalysts. *Stud. Surf. Sci. Catal.*, 112:267–275, 1997.

[93] A. Trovarelli. Catalytic properties of ceria and CeO_2-containing materials. *Catalysis Reviews - Science and Engineering*, 38:439–520, 1996.

[94] J. Wei and E. Iglesia. Structural requirements and reaction pathways in methane activation and chemical conversion catalyzed by rhodium. *Journal of Catalysis*, 225:116–127, 2004.

[95] I. Tavazzi, A. Beretta, G. Groppi, and P. Forzatti. Development of a molecular kinetic scheme for methane partial oxidation over a Rh/α -Al_2O_3 catalyst. *Journal of Catalysis*, 241:1–13, 2006.

[96] A. Donazzi, A. Beretta, G. Groppi, and P. Forzatti. Catalytic partial oxidation of methane over a 4% Rh/α -Al_2O_3 catalyst. Part II: Role of CO_2 reforming. *Journal of Catalysis*, 255:259–268, 2008.

[97] P.A. Simell, J.O. Hepola, and A.O.I. Krause. Effects of gasification gas components on tar and ammonia decomposition over hot gas cleanup catalysts. *Fuel*, 76:1117–1127, 1997.

[98] D.G. Castner, B.A. Sexton, and G.A. Somorjai. LEED and thermal desorption studies of small molecules (hydrogen, oxygen, carbon monoxide, carbon dioxide, nitric oxide, ethene, ethyne and carbon) chemisorbed on the rhodium (111) and (100) surfaces. *Surface Science*, 71:519–540, 1978.

[99] L. Devi, K.J. Patasinski, and F.J.J.G. Janssen. Decomposition of naphthalene as a biomass tar over pretreated olivine: Effect of gas composition, kinetic approach, and reaction scheme. *Industrial and Chemical Engineering Research*, 44:9096–9104, 2005.

[100] B.E. Koel. Thermal decomposition of benzene on the rhodium(111) crystal surface. *Journal of Physical Chemistry*, 90:2949–2956, 1986.

[101] D. Wang, O. Dewaele, A.M. De Groote, and G.F. Froment. Reaction mechanism and role of the support in the partial oxidation of methane on Rh/Al_2O_3. *Journal of Catalysis*, 159:418–426, 1996.

[102] J. Thormann, L. Maier, P. Pfeifer, U. Kunz, O. Deutschmann, and KI. Schubert. Steam reforming of hexadecane over a Rh/CeO_2 catalyst in microchannels: Experimental and numerical investigation. *International Journal of Hydrogen Energy*, 34:5108–5120, 2009.

[103] S. Hilaire, X. Wang, T. Luo, R.J. Gorte, and J. Wagner. A comparative study of water-gas-shift reaction over ceria supported metallic catalysts. *Applied Catalysis A*, 215:271–278, 2001.

[104] T. Bunluesin, R.J. Gorte, and G.W. Graham. Studies of the water-gas-shift reaction on ceria-supported Pt, Pd, and Rh: Implications for oxygen-storage properties. *Applied Catalysis B*, 15:107–114, 1998.

[105] G.W. Huber. Breaking the chemical and engineering barriers to lignocellulosic biofuels: Next generation hydrocarbon biorefineries. Technical report, The National Science Foundation. Chemical, bioengineering, environmental, and transport systems division. Washington D.C., 2008.

[106] A.M. Hansgate, P.D. Schloss, A.G. Hay, and L.P. Walker. Molecular characterization of fungal community dymanics in the initial stages of composting. *FEMS Microbiol. Ecol.*, 51:209–214, 2005.

[107] T.R. Carlson, T.P. Vispute, and G.W. Huber. Green gasoline by catalytic fast pyrolysis of solid biomass derived compounds. *ChemSusChem*, 1:397–400, 2008.

[108] G. Varhegyi, E. Jakab, and M.J. Antal. Is the Broido-Shafizadeh model for cellulose pyrolysis true? *Energy & Fuels*, 8:1345–1352, 1994.

[109] J. Piskorz, P. Majerski, D. Radlein, A. Vladars-Usas, and D.S. Scott. Flash pyrolysis of cellulose for production of anhydro-sugars. *Journal of Analytical and Applied Pyrolysis*, 56:145–166, 2000.

[110] J. Lede, J.P. Diebold, G.V.C Peacocke, and J. Piskorz. *Developments in Thermochemical biomass Conversion*. London: Blackie Academic & Professional, 1997.

[111] C. Di Blasi. Modeling chemical and physical processes of wood and biomass pyrolysis. *Prog. Energy Combust. Sci.*, 34:47–90, 2008.

[112] A.G. Uden, F. Berruti, and D.S. Scott. A kinetic model for the production of liquids from the flash pyrolysis of biomass. *Chemical Engineering Communications*, 65:207–221, 1988.

[113] J. Piskorz, D. Radlein, and D.S. Scott. On the mechanism of the rapid pyrolysis of cellulose. *Journal of Analytical and Applied Pyrolysis*, 9:121–137, 1986.

[114] J. Lede, H.Z. Li, and J. Villermaux. Fusion-like behaviour of wood pyrolysis. *Journal of Analytical and Applied Pyrolysis*, 10:291–308, 1987.

[115] O. Boutin, M. Ferrer, and J. Lede. Radiant flash pyrolysis of cellulose - Evidence for the formation of short life time intermediate liquid species. *Journal of Analytical and Applied Pyrolysis*, 47:13–31, 1998.

[116] D.L. Pyle and C.A. Zaror. Heat transfer and kinetics in the low temperature pyrolysis of solids. *Chemcial Engineering Science*, 39:147–158, 1984.

[117] C. Di Blasi. Kinetics and heat transfer control in the slow and flash pyrolysis of solids. *Industrial and Chemical Engineering Research*, 35:37–46, 1996.

[118] A.M. Kanury. Combustion characteristics of biomass fuels. *Combust. Sci. Technol.*, 97:469–491, 1994.

[119] W.E. Ranz and W.R. Marshall. Evaporation from drops. *Chemical Engineering Progress*, 48:141–146, 1952.

[120] I. Milosavljevic, V. Oja, and E.M. Suuberg. Thermal effects in cellulose pyrolysis: Relationship to char formation processes. *Industrial and Chemical Engineering Research*, 35:653–662, 1996.

[121] S. Chandra and C.T. Avedisian. Observations of droplet impingement on a ceramic porous surface. *Int. J. Heat Mass Transfer*, 35:2377–2388, 1992.

[122] Y.M. Arifin, T. Furuhata, M. Saito, and M. Arai. Diesel and biodiesel fuel deposits on a hot surface. *Fuel*, 87:1601–1609, 2008.

[123] J. Lede, J. Panagopoulos, H.Z. Li, and J. Villermaux. Fast pyrolysis of wood: Direct measurement and study of ablation rate. *Fuel*, 64:1514–1520, 1985.

[124] G.V.C. Peacocke and A.V. Bridgwater. Ablative plate pyrolysis of biomass for liquids. *Biomass and Bioenergy*, 7:147–154, 1994.

[125] R.S. Miller and J. Bellan. Numerical simulations of vortex pyrolysis reactors for condensable tar production from biomass. *Energy & Fuels*, 12:25–40, 1998.

[126] T. Kimura, T. Miyazawa, J. Nishikawa, S. Kado, K. Okumura, T Miyao, S. Naito, K. Kunimori, and K. Tomishige. Development of Ni catalysts for tar removal by steam gasification of biomass. *Applied Catalysis B*, 68:160–170, 2006.

[127] J. Nishikawa, K. Nakamura, M. Asadullah, T. Miyazawa, K. Kunimori, and K. Tomishige. Catalytic performance of $Ni/CeO_2/Al_2O_3$ modified with noble metals in steam gasification of biomass. *Catalysis Today*, 131:146–155, 2008.

[128] E.G. Baker, L.D. Mudge, and M.D. Brown. Steam gasification of biomass with nickel secondary catalysts. *Industrial and Chemical Engineering Research*, 26:1335–1339, 1987.

[129] M.P. Aznar, J. Corealla, J. Delgado, and J. Lahoz. Improved steam gasification of lignocellulosic residues in a fluidized bed with commercial steam reforming catalysts. *Industrial and Chemical Engineering Research*, 32:1–10, 1993.

[130] P. Perez, P.M Aznar, M.A. Caballero, J. Gil, J.A. Martin, and J. Corella. Hot gas cleaning and upgrading with a calcined dolomite located downstream of a biomass fluidized bed gasifier operating with steam-oxygen mixtures. *Energy & Fuels*, 11:1194–1203, 1997.

[131] J. Arauzo, D. Radlein, J. Piskorz, and D.S. Scott. A new catalyst for the catalytic gasification of biomass. *Energy & Fuels*, 8:1192–1196, 1994.

[132] D.S. Scott and J. Piskorz. The flash pyrolysis of aspen-poplar wood. *Canadian Journal of Chemical Engineering*, 60:666–674, 1982.

[133] M. Asadullah, T. Miyazawa, S. Ito, K. Kunimori, and K. Tomishige. Demonstration of real biomass gasification drastically promoted by effective catalyst. *Applied Catalysis A*, 246:103–116, 2003.

[134] P. Lv, J. Chang, T. Wang, Y. Fu, and Y. Chen. Hydrogen-rich gas production from biomass catalytic gasification. *Energy & Fuels*, 18:228–233, 2004.

[135] J. Gil, M. Caballero, J. Martin, M. Aznar, and J. Corella. Biomass gasification with air in a fluidized bed: Effect of the in-bed use of dolomite under different operation conditions. *Industrial and Chemical Engineering Research*, 38:4226–4235, 1999.

[136] A. Olivares, M.P. Aznar, M.A. Caballero, J. Gil, E. Frances, and J. Corella.

Biomass gasification: Produced gas upgrading by in-bed use of dolomite. *Industrial and Chemical Engineering Research*, 36:5220–5226, 1997.

[137] D.S. Scott and J. Piskorz. The continuous flash pyrolysis of biomass. *Canadian Journal of Chemical Engineering*, 62:404–412, 1994.

[138] L. Garcia, R. French, S. Czernik, and E. Chornet. Catalytic steam reforming of bio-oils for the production of hydrogen: Effects of catalyst composition. *Applied Catalysis A*, 201:225–239, 2000.

[139] A.C. Basagiannis and X.E. Verykios. Steam reforming of the aqueous fraction of bio-oil over structured $Ru/MgO/Al_2O_3$ catalysts. *Catalysis Today*, 127:256–264, 2007.

Appendix A

Nomenclature

CPO	Catalytic partial oxidation
S/C	Steam to carbon ratio
C/O	Carbon (from fuel) to oxygen (from gas) ratio
C_S	Solid carbon
H/C	Hydrogen to carbon ratio
$SLPM$	Standard liters per minute
AMU	Atomic mass units
WGS	Water-gas-shift (reaction)
SEI	Secondary electron imaging
WD	Working distance
SEM	Scanning electron microscope
BTL	Biomass-to-liquids
RPM	Revolutions per minute
LHV	Lower heating value
S_H	Hydrogen selectivity
S_C	Carbon selectivity
X	Conversion

VOC	Volatile organic compound
$RWGS$	Reverse water-gas-shift (reaction)
GC	Gas chromatograph
XRD	X-ray diffraction
Bi	Biot number
CMV	Carbon mass velocity
CSV	Carbon space velocity
MV	Mass velocity
RT	Retention time
PPI	Pores per (linear) inch

Appendix B

Construction of Figure 3.7[1]

The supplementary material contains a description of the assumptions that went into the construction of figure 3.7.

The development of Figure 3.7 required the review of several gasification publications and the selection of processing parameters with the goal of comparing several technologies. Due to the heterogeneous feed used in gasification, the two operating criteria selected for comparison were the carbon mass velocity and the carbon space velocity.

The molar flow rate of carbon has been selected as the processing parameter for comparison for several reasons. The heterogeneous feedstock (air/oxygen and solid material such as biomass) of most gasifiers permits a wide range of total mass feed rate depending on parameters such as the C/O ratio of the solid, the S/C ratio of the gasifier feed, and equivalence ratio of the gasifier. However, the molar flow rate of atomic carbon is the common parameter to which many of these factors are related.

[1] **Parts of this chapter appear in: J.L. Colby, P.J. Dauenhauer and L.D. Schmidt, "Millisecond autothermal steam reforming of cellulose for synthetic biofuels by reactive flash volatilization," *Green Chemistry*, 2008, 10, 773-783 - Reproduced by permission of The Royal Society of Chemistry (RSC).**

The carbon mass velocity (CMV) has been defined,

$$CMV = \frac{Mass\ FLow\ C}{Mass\ Catalyst} \tag{B.1}$$

The carbon space velocity (CSV) has been defined,

$$CSV = \frac{Molar\ FLow\ C}{Reaction\ Volume} \tag{B.2}$$

The "reaction volume" is considered to be the volume necessary to complete the reaction chemistry for the conversion of biomass/cellulose to synthesis gas. Because the strict definition varies by reactor type, the reaction volume will be carefully defined for each technology.

The considered technologies include 1) fluidized bed gasifiers followed by catalytic tar cleaning, 2) integrated catalytic fluidized beds, 3) fluidized bed fast pyrolysis reactors and steam reforming of fast pyrolysis oils to synthesis gas, and 4) reactive flash volatilization of cellulose.

Each of these technologies can be operated over a wide range of process parameters. Therefore, experimental trials were selected from publications that both exhibited optimal performance (low selectivity to tars) and high throughput.

Technologies that require two separate reactors (sets 1 and 3) were reported from one publication if possible. Additionally, multiple catalytic metals including dolomite, rhodium, nickel, and ruthenium were considered, because these catalysts were well-represented in the gasification literature.

Figure B.1 and Figure 3.7 show the results of considering the process parameters for all of these considered technologies grouped by type.

Data and information for fluidized bed gasifiers and catalytic tar cleaning is presented in Table B.1. Data and information for catalytic fluidized bed gasifiers is presented in Table B.2. Data and information for fast pyrolysis and catalytic steam reforming is presented in Table B.3. Data and information for reactive flash volatilization is presented in Table B.4.

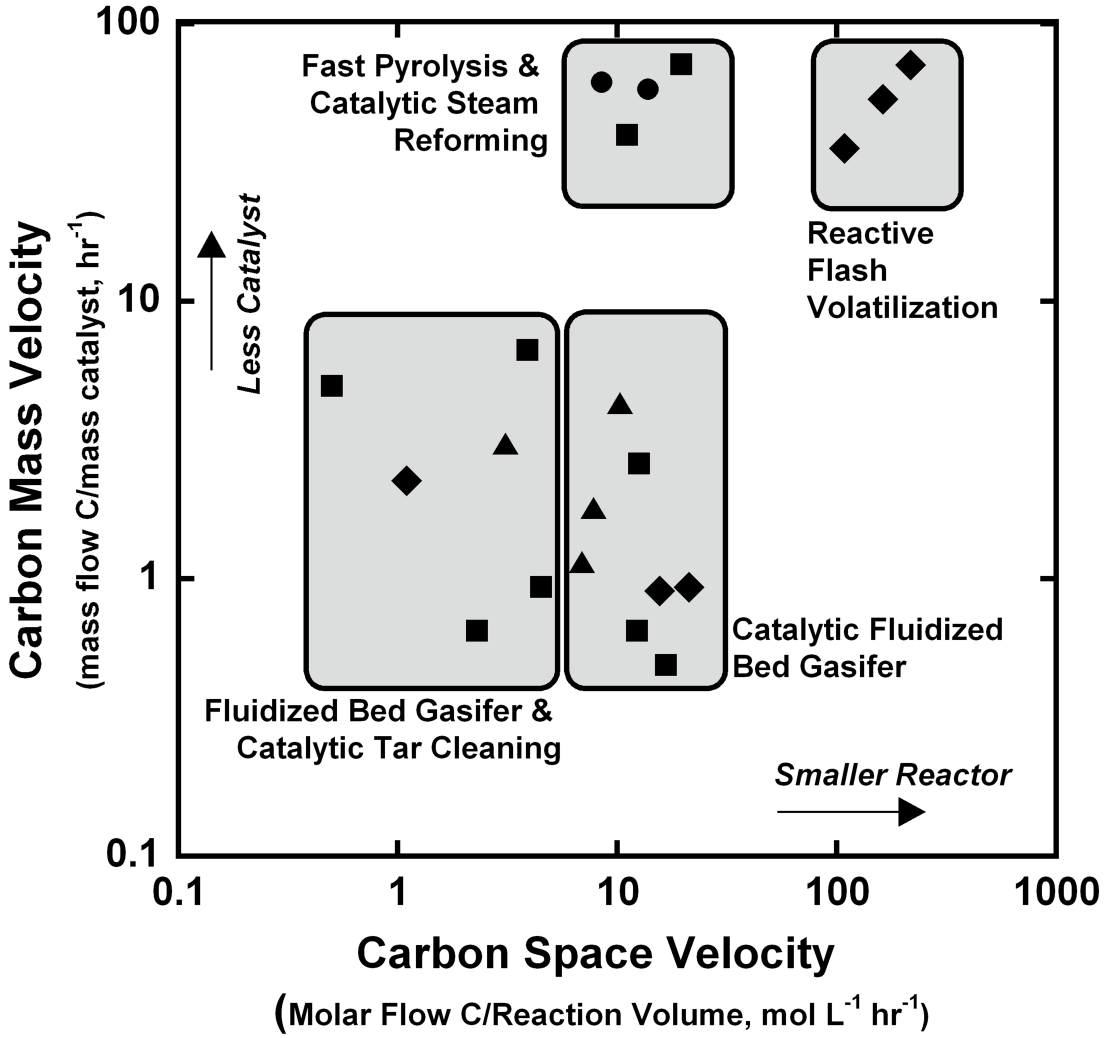

Figure B.1: Various processes to convert organic solids to synthesis gas exhibit operational performance grouped by process type despite utilizing several different catalysts: dolomite (▲), Ni (■), Rh (♦), Ru (•). The carbon space velocity provides a measure of the reactor volume by relating the molar processing of carbon to the volume necessary for chemical conversion. The carbon mass velocity provides a measure of catalyst usage by relating the molar processing of carbon to the mass of the catalyst.

Table B.1: Tabulated process parameters for fluidized bed gasifiers and catalytic tar cleaning.

Publication	[44]	[126, 127]	[128]	[129]	[41]	[130]
Feed Solid Material (g hr^{-1})	9	3.6	840	450	470	5000
Flow Carbon (g hr^{-1})	4.139	1.683	422.52	193.5	177.3	2300
Flow Carbon (mol hr^{-1})	0.345	0.140	35.210	16.125	14.78	191.7
Catalyst Type	Rh	Ni	Ni	NiO-Mg	Dolomite/Ni	Dolomite
All Catalyst Loading (g)	1.837	0.34	650	29	190	752
Reaction Volume (mL)	300	300	15260	4116	3313	61700
Temperature (°C)	650	650	750	780	700	840
Gasifying Medium	Oxygen	Oxygen	Steam	Steam	Steam/O_2	Steam/O_2
C Space Vel. (mol $hr^{-1}L^{-1}$)	1.1	0.5	2.3	3.9	4.5	3.1
Carbon Mass Velocity (hr^{-1})	2.253	4.951	0.650	6.673	0.933	3.059

The solid material for all cases was either wood or microcrystalline cellulose. The flow of carbon was determined based on the feedstock analysis of each publication. The total mass of catalyst loading does not include supports such as alumina or silica. The reaction volume for this technology was the sum of the gasifier total volume and the volume occupied by the tar cleaning catalysts (including void space between catalyst particles).

Table B.2: Tabulated process parameters for catalytic fluidized bed gasifiers.

Publication	[131, 132]	[40]	[133]	[128]	[126]	[134]	[135]	[136]
Feed Solid Material (g hr^{-1})	18.6	5.1	3.6	840	10.76	602	10550	9400
Flow Carbon (g hr^{-1})	8.923	2.264	1.656	422.52	5.19	308.6	5275	4700
Flow Carbon (mol hr^{-1})	0.7436	0.1887	0.1380	35.21	0.433	25.71	439.6	391.7
Catalyst Type	Ni	Rh	Rh	Ni	Ni-Mg	Dolomite	Dolomite	Dolomite
All Catalyst Loading (g)	18.23	2.437	1.837	650	2.0	72	2940	4100
Reaction Volume (mL)	44.5	8.84	8.84	2867	34.39	2490	56500	56500
Temperature (°C)	700	650	700	750	700	800	816	834
Gasifying Medium	Steam	Oxygen	Oxygen	Steam	Steam	Oxygen	Oxygen	Oxygen
C Space Vel. (mol $hr^{-1}L^{-1}$)	16.7	21.3	15.6	12.3	12.6	10.3	7.8	6.9
Carbon Mass Velocity (hr^{-1})	0.489	0.929	0.901	0.65	2.597	4.286	1.794	1.146

The solid material for all cases was either wood or microcrystalline cellulose. The flow of carbon was determined based on the feedstock analysis of each publication. The total mass of catalyst loading does not include supports such as alumina or silica. The reaction volume for catalytic fluidized bed gasifiers was defined as the volume occupied by the catalyst but does not include reactor volume not occupied by the catalyst such as freeboard.

Table B.3: Tabulated process parameters for fast pyrolysis and catalytic steam reforming.

Publication	[137, 138]	[132, 139]	[132, 138]	[137, 139]
Feed Solid Material (g hr^{-1})	1970	15	15	1970
Flow Carbon (g hr^{-1})	888.6	5.805	5.805	888.6
Flow Carbon (mol hr^{-1})	74.05	0.484	0.484	74.05
Catalyst Type	Ni	Ru	Ru	Ru
All Catalyst Loading (g)	12.44	0.094	0.146	15.3
Reaction Volume (mL)	3770	56.98	43.5	5350
Temperature (°C)	825	800	800	825
Gasifying Medium	Steam	Steam	Steam	Steam
Carbon Space Velocity (mol $hr^{-1}L^{-1}$)	19.6	8.5	11.1	13.8
Carbon Mass Velocity (hr^{-1})	71.43	61.56	39.76	58.07

The solid material for all cases was either wood or microcrystalline cellulose. The two separate reactors in each publication was scaled by the mass flow rate. The flow of carbon was determined based on the feedstock analysis of each publication. The total mass of catalyst loading does not include supports such as alumina or silica. The reaction volume for fast pyrolysis and catalytic steam reforming was defined as the sum of the volume occupied by the fast pyrolysis reactor tube and the volume occupied by the steam reforming catalyst (including void space between catalyst particles).

Table B.4: Tabulated process parameters for fast pyrolysis and catalytic steam reforming.

Publication	[30]	[30]	[30]
Feed Solid Material (g hr^{-1})	30	40	20
Flow Carbon (g hr^{-1})	13.32	17.76	8.88
Flow Carbon (mol hr^{-1})	1.11	1.48	0.74
Catalyst Type	Rh	Rh	Rh
All Catalyst Loading (g)	0.25	0.25	0.25
Reaction Volume (mL)	6.81	6.81	6.81
Temperature (°C)	833	850	750
Gasifying Medium	Oxygen	Oxygen	Oxygen
Carbon Space Velocity (mol $hr^{-1}L^{-1}$)	163	217	108.7
Carbon Mass Velocity (hr^{-1})	53.28	71.04	35.52

The solid material for all cases was microcrystalline cellulose. The total mass of catalyst loading does not include the support alumina. The reaction volume for reactive flash volatilization reactor was defined as the volume occupied by the catalyst (including void space between catalyst particles) but does not include reactor volume not occupied by the catalyst above and below the fixed bed.

Appendix C

Construction of Figure 4.2[1]

The numbers recorded/reported in Figure 4.2 (also Figure C.4) required adiabatic equilibrium information for the CPO of cellulose and CH_4 at four constant feed ratios in air with no preheat, varying the ratios Air/Fuel and Air/CO_2 over all possible concentrations. The results are presented as a ternary diagram with each axis representing a different reactor feed. The process of calculating the adiabatic equilibrium information and assembling the figure is described in this section.

C.1 Adiabatic Equilibrium Calculations

A large number of equilibrium calculations (on the order of tens of thousands) were required for the assembly of Figure 4.2. To allow for efficient acquisition of the desired data, a program was written in Python programming language and interfaced with Cantera, an open source equilibrium solver developed by Professor David Goodwin at Caltech. Cantera calculates the thermodynamic equilibrium of a system, in this case a two phase system, by using the method of element potential.

[1] **Parts of this chapter appear in: J.L. Colby, P.J. Dauenhauer, Brian C. Michael, Aditya Bhan and L.D. Schmidt, "Improved utilization of biomass-derived carbon by co-processing with hydrogen-rich feedstocks in millisecond reactors," *Green Chemistry*, 2010, 12, 378-380 - Reproduced by permission of The Royal Society of Chemistry (RSC).**

Cantera was used to calculate isothermal equilibrium concentrations for specified feed conditions holding preheat constant at 25 °C and pressure constant at 1 atm. Species included in the calculation were H_2, H_2O, CO, CO_2, N_2, O_2, CH_4, and a variety of higher hydrocarbons in the gas phase, and graphite in the solid phase. Results were used to calculate total heat capacity of the system and heat of reaction (using information available through the NIST Chemistry WebBook). The heat of formation of cellulose was obtained from Milosavljevic et al. who determined it to be -1020.1 kJ/equiv, "where '1 equiv' of cellulose corresponds to 1 formula weight equivalent of 162 g per cellulose repeat unit."[120] The bisection method was used to converge to the adiabatic equilibrium condition for each feed composition by determining the temperature at which the sum of all species heat capacities balanced with the heat of reaction.

To verify the results obtained using Cantera, equilibrium calculations were also performed for selected data points using HSC Chemistry software (commercially available), which calculates equilibrium by minimizing Gibbs free energy of formation for the system.[46] In addition to graphitic carbon, amorphous carbon was included in the solid phase for equilibrium calculations performed with HSC Chemistry software.

C.2 Assembly of Figure 4.2

Adiabatic equilibrium information was determined for approximately 10,000 equally spaced points covering the entire ternary diagram of Figure 4.2, which displays all possible feed ratios for the fuel, air, and CO_2 mixture. Data in Figures C.1, C.2, and C.3 are not equally spaced because data has been renormalized to exclude N_2. We assumed 100% conversion of cellulose for all calculations, consistent with experimentally observed behavior. Results were first analyzed to determine operating conditions where there was zero net generation of carbon dioxide, meaning there is no more CO_2 in the effluent of the reactor than in the feed. This region was determined by analyzing the

carbon selectivity to CO_2, where carbon selectivity to CO_2 was defined as:

$$S_{CO_2} = \frac{n_{CO_2,equil} - n_{CO_2,feed}}{n_{C,feed} - n_{CO_2,feed}} \tag{C.1}$$

where S_{CO_2} is the carbon selectivity to CO_2, $n_{CO_2,equil}$ is the number of moles of CO_2 at adiabatic equilibrium, $n_{CO_2,feed}$ is the number of moles of CO_2 in the feed, and $n_{C,feed}$ is the total number of moles of carbon in the feed (equal to the total number of moles of carbon in the effluent). As an example, all points where the selectivity to CO_2 is a negative value for $C_{(C_6H_{10}O_5)_n}/C_{CH_4}$=0.25 are presented in Figure C.1.

In CPO reactors it is important to operate under conditions free of stable solid carbon formation for two reasons: 1) carbon is an undesired product, and 2) carbon can shut down the reactor by covering active catalytic sites. A figure similar to Fig. C.1 was assembled describing a region of operation where graphitic and amorphous carbon are not thermodynamically predicted to exist in the solid phase. All points meeting these criteria at adiabatic equilibrium are presented in Figure C.2 for $C_{(C_6H_{10}O_5)_n}/C_{CH_4}$=0.25.

By overlaying Figures C.1 and C.2, a regime of operation where solid carbon is not a thermodynamic product and there is no net generation of CO_2 in the reactor (Figure C.3), corresponding to an area where ~100% yield of CO is expected.

The process described in Figures C.1-C.3 can be repeated for different ratios of $C_{(C_6H_{10}O_5)_n}/C_{CH_4}$. Results are presented for four different $C_{(C_6H_{10}O_5)_n}/C_{CH_4}$ ratios in Figure C.4, with the carbon neutral boundaries outlining the areas in which thermodynamic calculations predict zero net generation of CO_2 and no solid carbon formation. Additionally, to give an idea of temperature and fuel to oxygen ratio, selected isotherms and combustion lines were added to the figure based on adiabatic calculations. It should be noted that as the isotherms approach the O_2 axis they do not discontinue. Instead they turn towards the C_{Fuel} axis and continue until intersection. This portion of the isotherms was omitted from the figure for clarity.

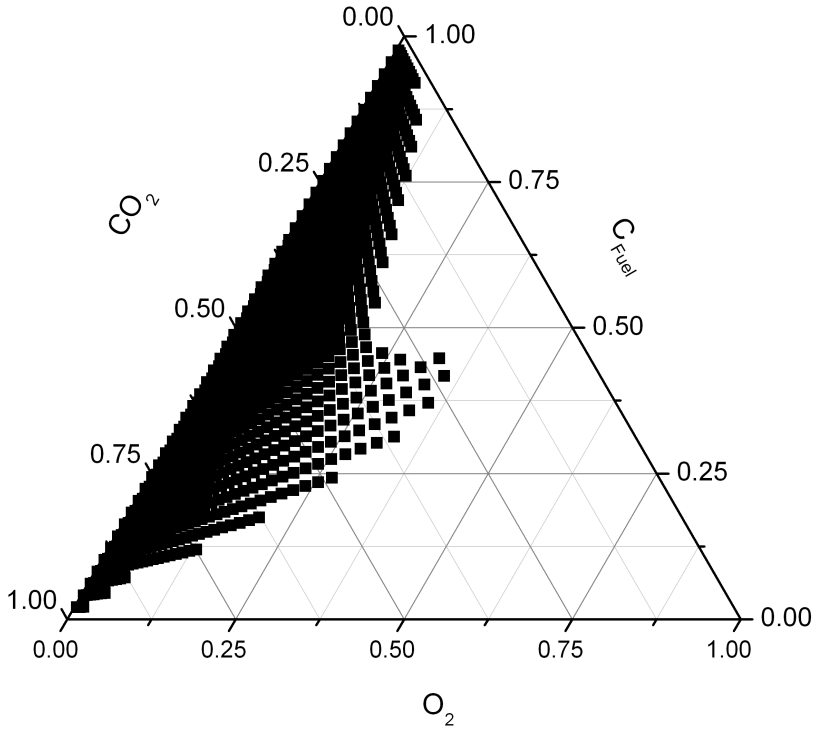

Figure C.1: Adiabatic equilibrium calculations for CPO of cellulose and CH_4 at $C_{(C_6H_{10}O_5)_n}/C_{CH_4}$=0.25 in air with no preheat and varying ratios of Air/Fuel and Air/CO_2 over all possible concentrations. Results (renormalized without nitrogen) describe a regime where the selectivity to CO_2 is less than zero, meaning there is less CO_2 in the effluent than in the feed. The boundary of this region represents operating conditions where there is zero net carbon dioxide generated, meaning the effluent contains the same amount of CO_2 as the feed.

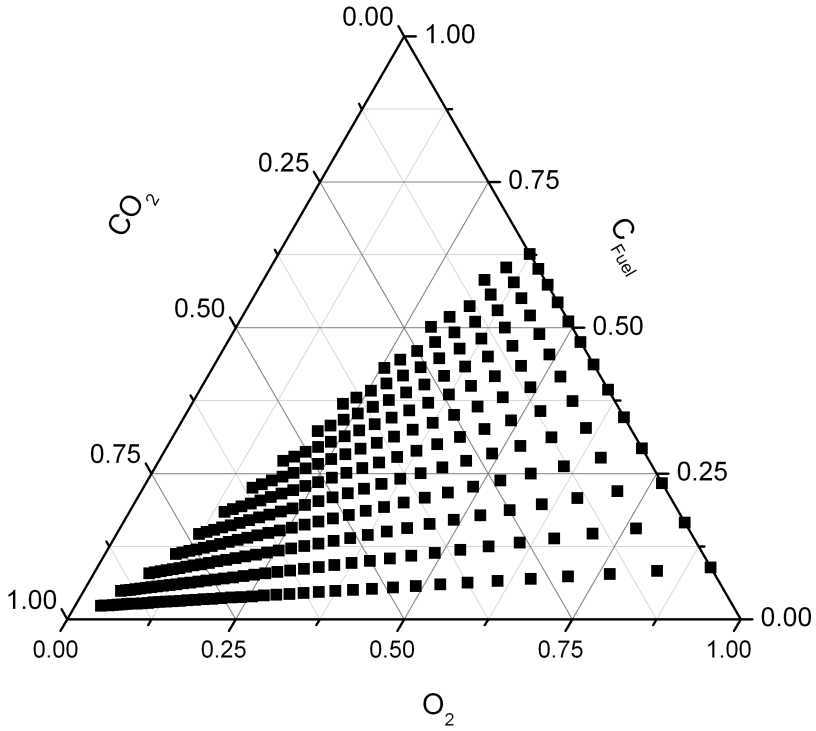

Figure C.2: Adiabatic equilibrium calculations for CPO of cellulose and CH_4 at $C_{(C_6H_{10}O_5)_n}/C_{CH_4}$=0.25 in air with no preheat and varying ratios of Air/Fuel and Air/CO_2 over all possible concentrations. Results (renormalized without nitrogen) describe a regime where no solid amorphous or graphitic carbon is predicted.

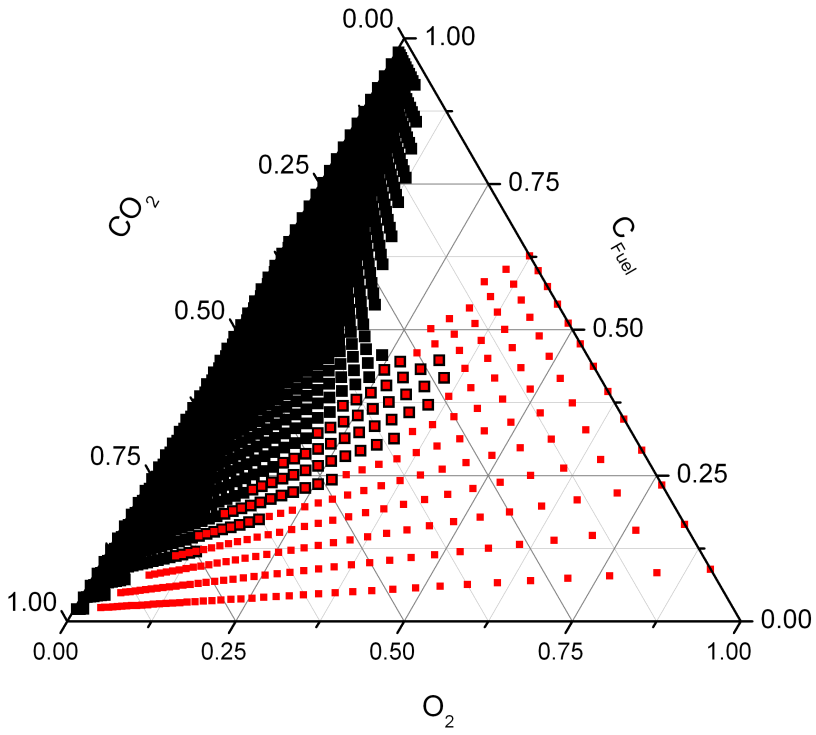

Figure C.3: Adiabatic equilibrium calculations for CPO of cellulose and CH_4 at $C_{(C_6H_{10}O_5)_n}/C_{CH_4}$=0.25 in air with no preheat and varying ratios of Air/Fuel and Air/CO_2 over all possible concentrations. Results (renormalized without nitrogen) overlap to describe a regime of operation where solid carbon is not a thermodynamic product and there is a net consumption of CO_2 in the reactor, corresponding to an area where >100% yield of CO is expected.

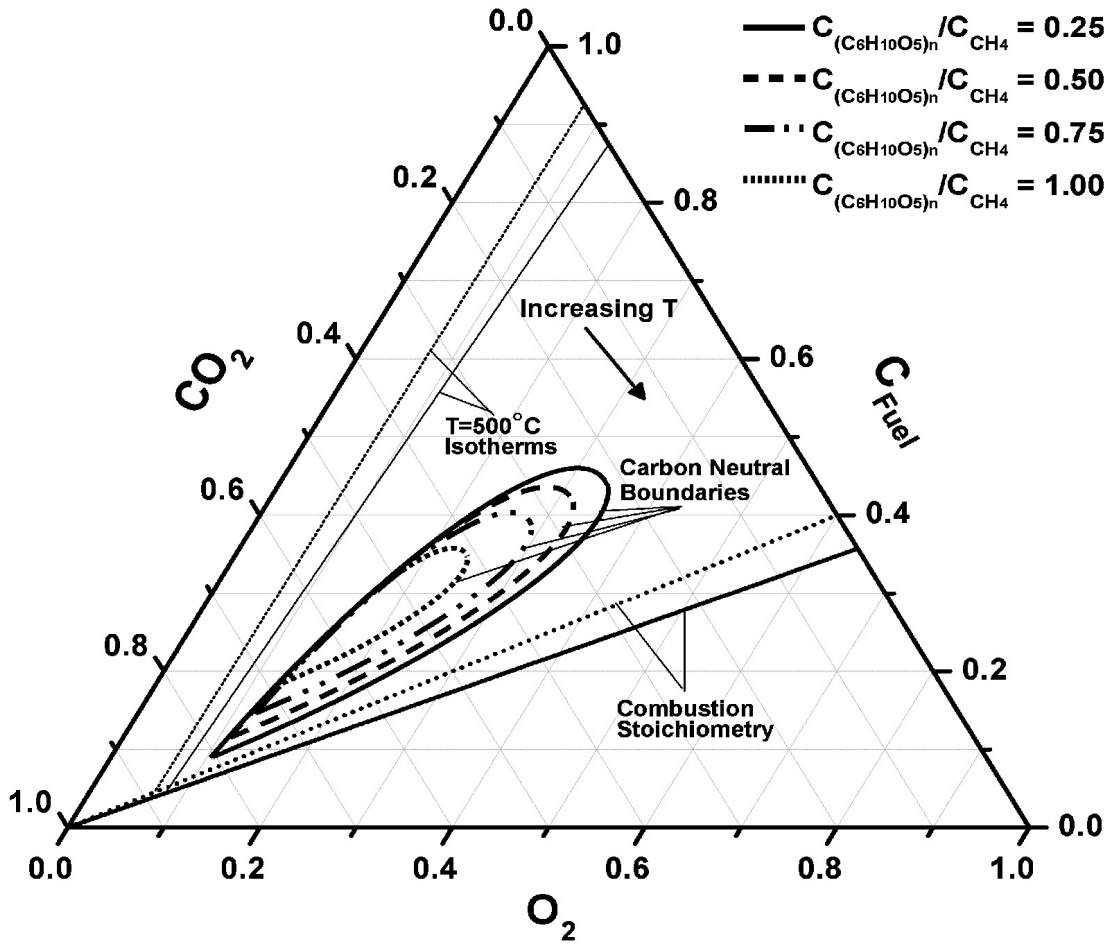

Figure C.4: Operating diagram derived from adiabatic equilibrium calculations for CPO of cellulose and CH_4 at four constant feed ratios in air with no preheat, varying ratios Air/Fuel and Air/CO_2 over all possible concentrations. Results (renormalized without nitrogen) describe a regime of operation where solid carbon is not a thermodynamic product and there is zero net generation of CO_2, corresponding to CO yields $\geq$100%.

Appendix D

Construction of Table 4.1[1]

The construction of Table 4.1 (also Table D.1) required the calculation of a variety of parameters and results. In this section details describing the calculation of C/O ratio, $C_{(C_6H_{10}O_5)_n}/C_{CH_4}$, H selectivity to H_2, H selectivity to H_2O, C selectivity to CO, C selectivity to CO_2, C selectivity to CH_4, residence time, mass velocity, H_2/CO, and syngas yield are presented.

The C/O ratio was defined to be:

$$C/O = \frac{n_{C,CH_4\ Feed} + n_{C,Cellulose\ Feed}}{n_{O,O_2\ Feed}} \tag{D.1}$$

where $n_{C,CH_4\ Feed}$ is the molar flow rate of carbon in methane in the feed, $n_{C,Cellulose\ Feed}$ is the molar flow rate of carbon in cellulose in the feed, and $n_{O,O_2\ Feed}$ is the molar flow rate of oxygen in molecular oxygen in the feed.

The ratio of $C_{(C_6H_{10}O_5)_n}/C_{CH_4}$ was defined to be:

$$C_{(C_6H_{10}O_5)_n}/C_{CH_4} = \frac{n_{C,Cellulose\ Feed}}{n_{C,CH_4\ Feed}} \tag{D.2}$$

[1] **Parts of this chapter appear in: J.L. Colby, P.J. Dauenhauer, Brian C. Michael, Aditya Bhan and L.D. Schmidt, "Improved utilization of biomass-derived carbon by co-processing with hydrogen-rich feedstocks in millisecond reactors," *Green Chemistry*, 2010, 12, 378-380 - Reproduced by permission of The Royal Society of Chemistry (RSC).**

The H selectivity to H_2 was defined to be:

$$S_{H_2} = \frac{n_{H,H_2\ Effluent}}{n_{H,\ Effluent}} \tag{D.3}$$

where $n_{H,H_2\ Effluent}$ is the molar flow rate of hydrogen in the molecular hydrogen product stream and $n_{H,\ Effluent}$ is the total molar flow rate of hydrogen in the product stream.

The H selectivity to H2O was defined to be:

$$S_{H_2O} = \frac{n_{H,H_2O\ Effluent}}{n_{H,\ Effluent}} \tag{D.4}$$

where $n_{H,H_2O\ Effluent}$ is the molar flow rate of hydrogen in the water product stream.

The C selectivity to CO was defined to be:

$$S_{CO} = \frac{n_{C,CO\ Effluent}}{n_{C,\ Effluent} - n_{C,CO_2\ Feed}} \tag{D.5}$$

where $n_{C,CO\ Effluent}$ is the molar flow rate of carbon in the carbon monoxide product stream, $n_{C,\ Effluent}$ is the total molar flow rate of carbon in the product stream, and $n_{C,CO_2\ Feed}$ is the molar flow rate of carbon in carbon dioxide in the feed. The values for carbon selectivity to CO are identical to CO yield because conversion is always 100% in the reactor system.

The C selectivity to CO_2 was defined to be:

$$S_{CO_2} = \frac{n_{C,CO_2\ Effluent} - n_{C,CO_2\ Feed}}{n_{C,\ Effluent} - n_{C,CO_2\ Feed}} \tag{D.6}$$

where $n_{C,CO_2\ Effluent}$ is the molar flow rate of carbon in the carbon dioxide product stream, and $n_{C,CO_2\ Feed}$ is the molar flow rate of carbon in carbon dioxide in the feed.

The C selectivity to CH4 was defined to be:

$$S_{CH_4} = \frac{n_{C,CH_4\ Effluent}}{n_{C,\ Effluent} - n_{C,CO_2\ Feed}} \tag{D.7}$$

where $n_{C,CH_4\ Effluent}$ is the molar flow rate of carbon in the methane product stream.

The residence time was defined to be:

$$RT = \frac{Void\ Space\ in\ Catalyst\ Bed}{Volumetric\ Flow\ Rate\ of\ Effluent\ Gases} \tag{D.8}$$

Note: Residence times were calculated using the effluent, which contains more moles of gaseous species than the feed. Residence times calculated using the feed varied by no more than 25% from the results presented in Table D.1.

The mass velocity was defined to be:

$$MV = \frac{Mass\ Flow\ Rate\ of\ C\ in\ Fuel\ Feed}{Mass\ of\ Catalyst\ (Rh\ +\ Ce)} \tag{D.9}$$

The H_2/CO ratio was defined to be:

$$H_2/CO = \frac{n_{H_2\ Effluent}}{n_{CO\ Effluent}} \tag{D.10}$$

where $n_{H_2\ Effluent}$ is the molar flow rate of molecular hydrogen in the product stream and $n_{CO\ Effluent}$ is the molar flow rate of carbon monoxide in the product stream.

The syngas yield was defined to be:

$$Syngas\ Yield = \frac{n_{CO\ Effluent} + n_{H_2\ Effluent}}{n_{Effluent} - n_{C,CO_2\ Feed}} \tag{D.11}$$

where $n_{Effluent}$ is the total molar flow rate of all molecules in the product stream.

Table D.1: Selected experimental and theoretical (italics) data for the millisecond CPO of cellulose and CH_4 with CO_2 addition.

Experiment/*Calculation*	1	2	3	4	5	*1*	*2*	*3*	*4*	*5*
Parameters										
Catalyst Bed Length (mm)	60	60	60	60	60	-	-	-	-	-
C/O Ratio	0.6	0.6	0.6	0.6	0.6	*0.82*	*0.79*	*1.00*	*0.91*	*0.70*
$C_{(C_6H_{10}O_5)_n}/C_{CH_4}$	∞	5	2	1	0.5	*0.5*	*0.25*	*0.75*	*0.25*	*0.5*
CH_4/O_2 Ratio	0	0.2	0.4	0.6	0.8	*1.09*	*1.27*	*1.14*	*1.45*	*0.93*
CO_2/O_2 Ratio	0	0.91	1.86	2.81	3.76	*1.81*	*1.59*	*0.57*	*0.31*	*2.6*
N_2/O_2 Ratio	3.76	2.86	1.91	0.95	0	*3.76*	*3.76*	*0*	*0*	*0*
Cellulose Flow (g hr^{-1})	50	50	50	50	50	-	-	-	-	-
Results										
Temperature (°C)										
20 mm	1061	1108	1040	1056	1139	-	-	-	-	-
40 mm	1018	965	897	916	985	-	-	-	-	-
Adiabatic	-	-	-	-	-	*652*	*643*	*895*	*892*	*953*
H Selectivity (%)										
H_2	14.9	27.4	26.3	23.7	29.6	*63.9*	*66.4*	*74.9*	*83.6*	*36.6*
H_2O	85.1	72.6	72.9	74.1	68.8	*33.7*	*29.3*	*25.0*	*16.2*	*63.3*
C Selectivity (%)										
CO (Yield[a])	19.5	43.0	71.3	94.5	107.6	*100.9*	*101.6*	*101.6*	*101.4*	*131.4*
CO_2	80.5	57.0	28.2	3.9	-8.7	*-2.8*	*-5.4*	*-1.7*	*-1.5*	*-31.4*
CH_4	0	0	0.5	1.6	1.1	*1.8*	*3.7*	*0.0*	*0.1*	*0.0*
Residence Time (ms)	28.1	23.4	19.1	13.7	9.3	-	-	-	-	-
Mass Velocity (hr^{-1})	43.0	51.6	64.5	86.1	129.1	-	-	-	-	-
H_2/CO	0.74	0.55	0.46	0.40	0.41	*1.02*	*1.15*	*1.11*	*1.46*	*0.45*
Syngas Yield (%)	6.5	16.1	27.5	40.0	51.1	*41.6*	*42.8*	*85.1*	*89.6*	*65.1*

[a]Results for CO selectivity are identical to CO yield, because there is always 100% conversion of cellulose to C_1 products in the reactor.

Appendix E

Comparison of Integrated vs. Independent Reforming of Cellulose via CPO With CH_4 and CO_2 Co-Feeds[1]

In order to compare theoretical results obtained by independently reforming cellulose and methane with results obtained by the simultaneous co-reforming of both fuels, adiabatic equilibrium calculations were performed using HSC equilibrium solver.[46] Information is presented for four different feed conditions in Table E.1.

Parameters used for calculations 1a, 2a, 3a and 4a are for independent cellulose reforming. Parameters used for calculations labeled 1b, 2b, 3b and 4b are for independent methane reforming. Parameters used for calculations 1c, 2c, 3c and 4c are for simultaneous co-reforming of both fuels.

[1] **Parts of this chapter appear in: J.L. Colby, P.J. Dauenhauer, Brian C. Michael, Aditya Bhan and L.D. Schmidt, "Improved utilization of biomass-derived carbon by co-processing with hydrogen-rich feedstocks in millisecond reactors," *Green Chemistry*, 2010, 12, 378-380 - Reproduced by permission of The Royal Society of Chemistry (RSC).**

Adiabatic equilibrium temperature results are included for each calculation performed. Adiabatic equilibrium selectivities to H_2, H_2O, CO, CO_2 and the H_2/CO ratio are presented for: 1) the mixed product streams from independent cellulose reforming and independent methane reforming, and 2) the product stream for simultaneous co-reforming of cellulose and methane. Results obtained after mixing products from the independent reforming of each fuel are presented in italics and centered between columns labeled 'a' and 'b' for each of the four feed conditions considered. Results obtained from concurrent reforming of both fuels are presented in regular font in columns 1c, 2c, 3c and 4c. The data demonstrates a substantial improvement in carbon efficiency through co-reforming, rather than independent cellulose and methane reforming followed by mixing.

Table E.1: Theoretical data at four different feeds for the reforming of cellulose (a) and methane (b) with mixed product streams (italics), and the co-reforming of cellulose and methane (c), both with carbon dioxide addition.

Calculation	1a	1b	1c	2a	2b	2c	3a	3b	3c	4a	4b	4c
Parameters												
C/O Ratio	0.6	0.6	0.6	0.6	0.6	0.6	0.6	0.6	0.6	0.8	0.8	0.8
$C_{(C_6H_{10}O_5)_n}/C_{CH_4}$	∞	0	5	∞	0	2	∞	0	1	∞	0	0.5
CO_2/O_2 Ratio	0.91	0.91	0.91	1.86	1.86	1.86	2.81	2.81	2.81	3.76	3.76	3.76
N_2/O_2 Ratio	2.86	2.86	2.86	1.90	1.90	1.90	0.95	0.95	0.95	0.00	0.00	0.00
Results												
Adiabatic Temp. (°C)	1677	960	1536	1565	863	1306	1468	806	1110	1161	617	673
H Selectivity (%)												
H_2		*21.4*	*10.6*		*28.3*	*14.0*		*32.0*	*18.2*		*45.8*	*50.8*
H_2O		*78.6*	*89.4*		*71.7*	*86.0*		*67.9*	*81.8*		*47.6*	*48.4*
C Selectivity (%)												
CO (Yield)		***44.4***	***55.7***		***65.4***	***82.9***		***87.9***	***107.5***		***107.1***	***123.9***
CO_2		*55.6*	*44.3*		*34.6*	*17.1*		*12.1*	*-7.5*		*-12.8*	*-24.5*
H_2/CO		*0.48*	*0.19*		*0.43*	*0.17*		*0.36*	*0.17*		*0.43*	*0.41*

Appendix F

Supplementary Information: Reactive Boiling of Cellulose for Integrated Catalysis Through an Intermediate Liquid[1]

F.1 Method for Small Cellulose Particles on Foams

Visualization of microcrystalline cellulose particles on a 80 ppi α-Al_2O_3 foam coated with Rh-Ce (2.5 wt% each) occurred in a 20 mm I.D. quartz reactor tube shown in Figure F.1. Three foams (10 mm high, 18 mm wide) were stacked on top of each other with a fourth blank 80 ppi foam on the bottom, wrapped in ceramic paper (for friction fit), and slid into the reactor tube. A type K thermocouple was inserted 10 mm from the leading surface. A 1 cm Pyrex tube combined with a size 20 Pyrex reactor tube

[1] **Parts of this chapter appear in: P.J. Dauenhauer, J.L. Colby, C.M. Balonek and L.D. Schmidt, "Reactive Boiling of Cellulose for Integrated Catalysis Through an Intermediate Liquid," *Green Chemistry*, 2009, 11, 1555-1561 - Reproduced by permission of The Royal Society of Chemistry (RSC).**

end cap provided the connection between the reactor and a cellulose hopper necessary for solid particle delivery. A quartz light pipe was inserted through the end cap and contacted the leading surface providing a light sample to an optical pyrometer. The cellulose particles (avg. 315 μm diameter) stored in an acrylic tube hopper ($\sim$10 cm diameter) were pushed into a feed tube (0.25 inch I.D.) using a 0.25 inch wood auger driven inreverse with a servo motor permitting variable feed rates. Air was supplied by a gas cylinder and metered by a flow control valve calibrated with a bubble column.

The reactor in Figure F.1 was wrapped in a resistive heater controlled by a variac and wrapped in insulation. Autothermal operation was initiated by heating the reactor externally with air flow to $\sim$400 °C, at which point particles were delivered to the surface. Steady operation was obtained within $\sim$5 minutes, and the heater was turned off. Varying surface temperatures were obtained by varying the air flow rate or cellulose flow rate.

Digital video was obtained by focusing a Photron Fastcam Ultima APX with color image through the curved quartz reactor. The four optical lenses placed in series to obtain the presented magnification were: 1) a Micro-NIKKOR 105 mm lens by Nikon of Japan, 2) a Nikon PN-11 extension tube by Nikon of Japan, 3) a Kenko extension tube for Nikon/AF 36 mm by Kenko of Japan, and 4) a Kenko 2x Teleplus MC7 telephoto extension tube by Kenko of Japan. Light was provided to the catalyst necessary for high speed imaging by a Solarc Light LB-50 by Welch Allyn, Inc. of New York, U.S.A.

Additional videos are shown as Figures F.2 and F.3, and Figure 6.1 from the Chapter 6 is repeated as Figure F.4. Figure F.2 shows the behavior of two particles impacting and coming to rest near each other on a the catalytic foam within $\sim$20 ms. After converting to an intermediate liquid, the two particles combine in about 3 ms to form a larger liquid particle which ultimately volatilizes at $\sim$180 ms. Gaseous evolution is clearly visible from 100-137 ms. The frames illustrate the particles tendency to form spherical liquid droplets. White streaks in frames 100 and 123 ms are small particles passing through the frame before contacting the surface and volatilizing. Figure F.3

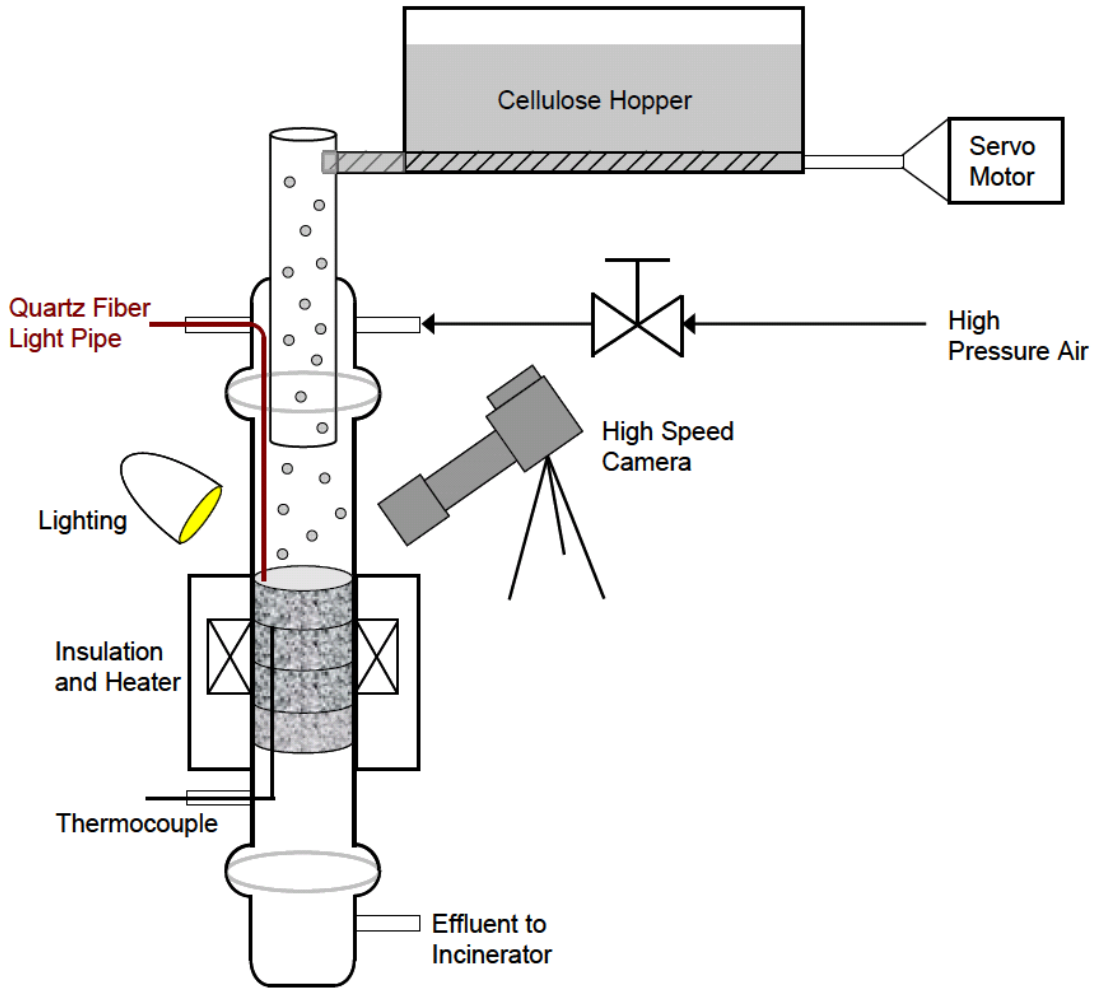

Figure F.1: Cellulose particle conversion was studied on RhCe-coated alumina foams in air in a visibly transparent 20 mm I.D. quartz tube surrounded by a resistive heater wrapped in ceramic insulation. Particles were delivered to the surface using an acrylic tube hopper through which passed a 0.25 inch wood auger operating in reverse. Cellulose flow rate was set by controlling the rotational speed of the wood auger with a servo motor. Air was supplied with a high pressure gas cylinder and metered using a gas-flow needle valve. A thermocouple was inserted into the catalytic bed 10 mm below the leading surface. A quartz fiber light pipe was inserted through the feed end-cap and impinged on the leading catalytic surface perpendicularly. Effluent was sent to an incinerator.

shows a lone, irregularly shaped particle coming to rest on an alumina strut, converting to a liquid, and volatilizing to gases in ∼123 milliseconds. The particle forms an intermediate liquid overhanging the narrower strut, but surface tension pulls the liquid into a more spherical conformation.

F.2 Method for Small Particle Cellulose Feedstock

Microcrystalline cellulose obtained from FMC biopolymer (Lattice NT-200) was sieved to average size ∼315 μm. As shown in Figure F.5, the particles are not perfectly spherical, but rather have an aspect ratio (defined as length/width) of 1.39±0.05 (95% confidence interval) when considering only particles large enough for examination with high speed photography (>20 μm). Examination of cellulose particles by light scattering reveals in the size distribution (vol%) that most of the mass of the cellulose exists as large particles (>200 μm). However, most of the particles are small (∼1 μm). Figure F.6 includes scanning electron micrographs of microcrystalline particles coated in Pt. The particles clearly exhibit high porosity with large void spaces (10-40 μm) within the particle.

F.3 Method for Small Particle Conversion on Catalytic Foams

Three video files with $T_{surface}$ = 700, 825, and 900 °C were obtained by varying the cellulose and air flow rates. At each of the listed conditions, approximately 50 particles were tracked from resting impact (not moving on the surface) to the point in time when no visual trace of the particle was evident. At each of the three conditions, the total conversion time was directly proportional to the square of the initial particle radius (measured at the point of resting impact). The difference between the measured conversion times and a linear fit appears to increase with increasing particle dimensions.

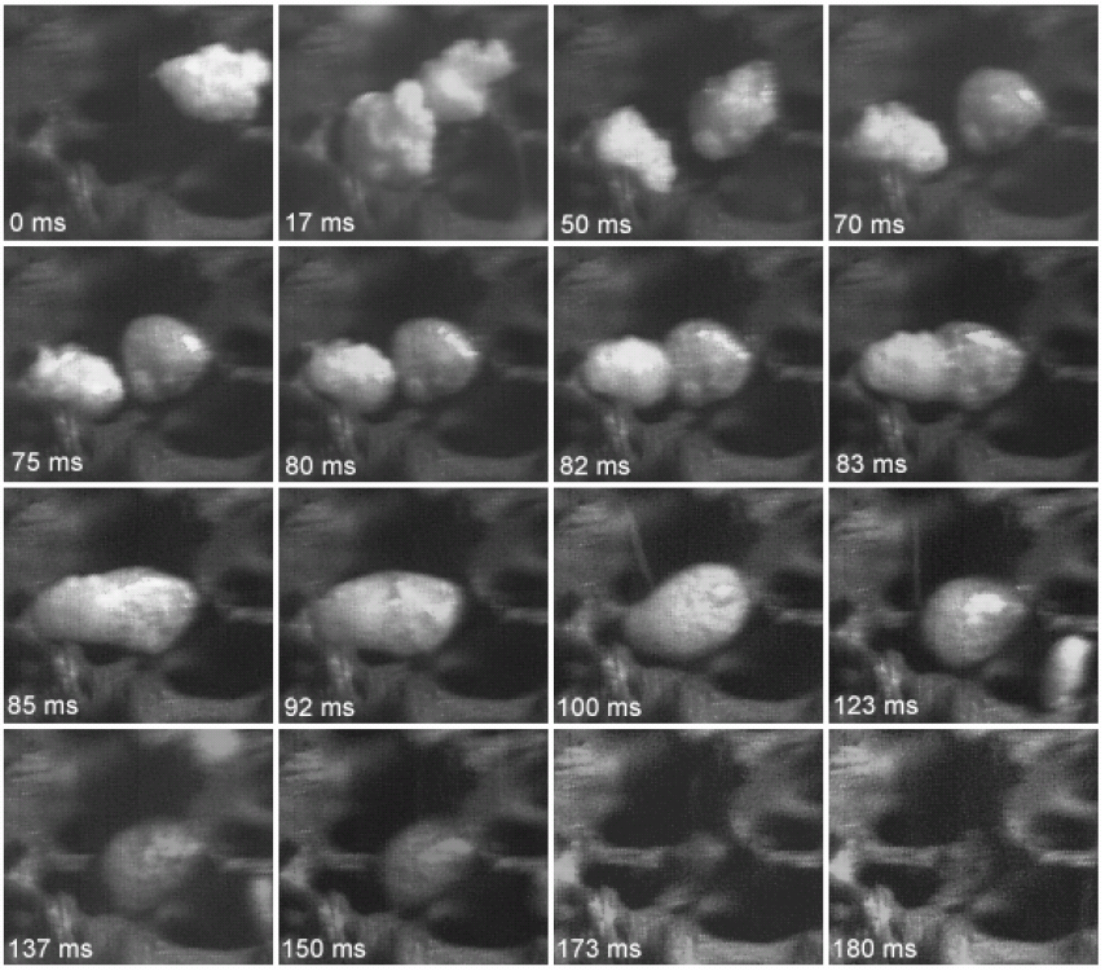

Figure F.2: Microcrystalline cellulose particles (∼300 μm) reacting to volatile species in air on a 700 °C Rh-Ce/α-Al_2O_3 surface have been visualized with high-speed photography on an 80 ppi Al_2O_3 foam support at C/O=1.15 at 45° from the surface normal with temporal resolution of one millisecond. Two particles (impacting at 0 and 17 ms) convert to a liquid and combine (82-85 ms) to a single particle which reactively volatilizes completely (180 ms).

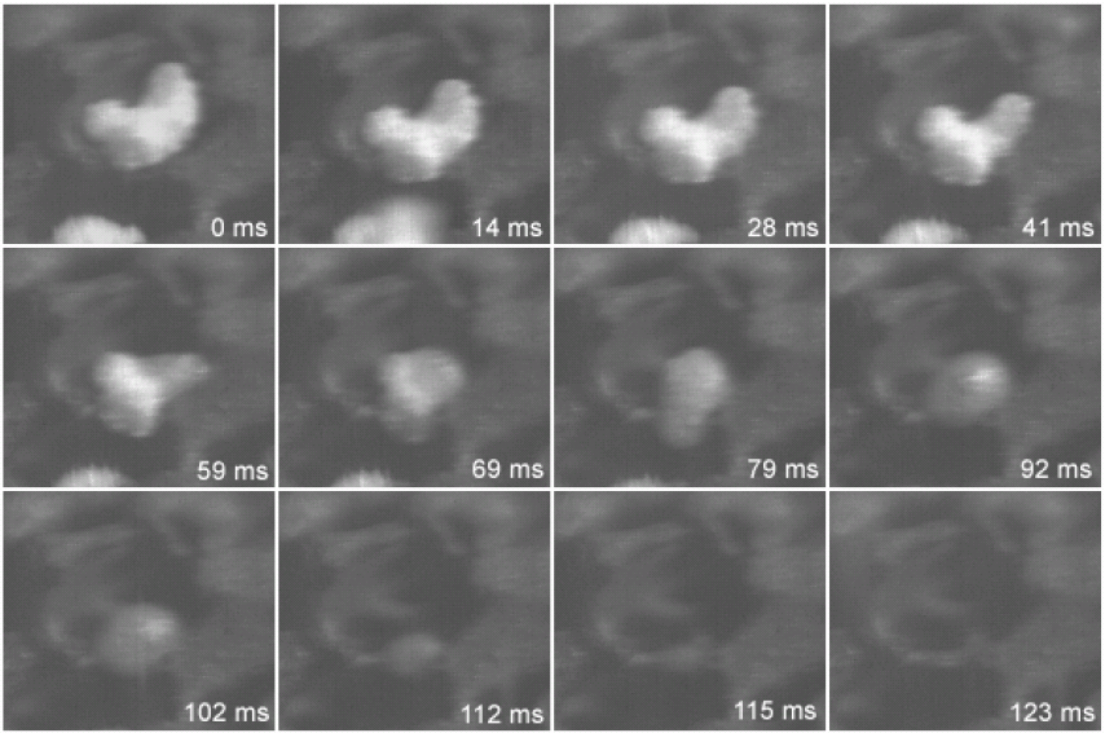

Figure F.3: Conversion of ∼300 μm microcrystalline cellulose particle to volatile species on a 700 °C Rh-Ce/α-Al_2O_3 surface. Cellulose passes through a molten intermediate state before volatilizing completely.

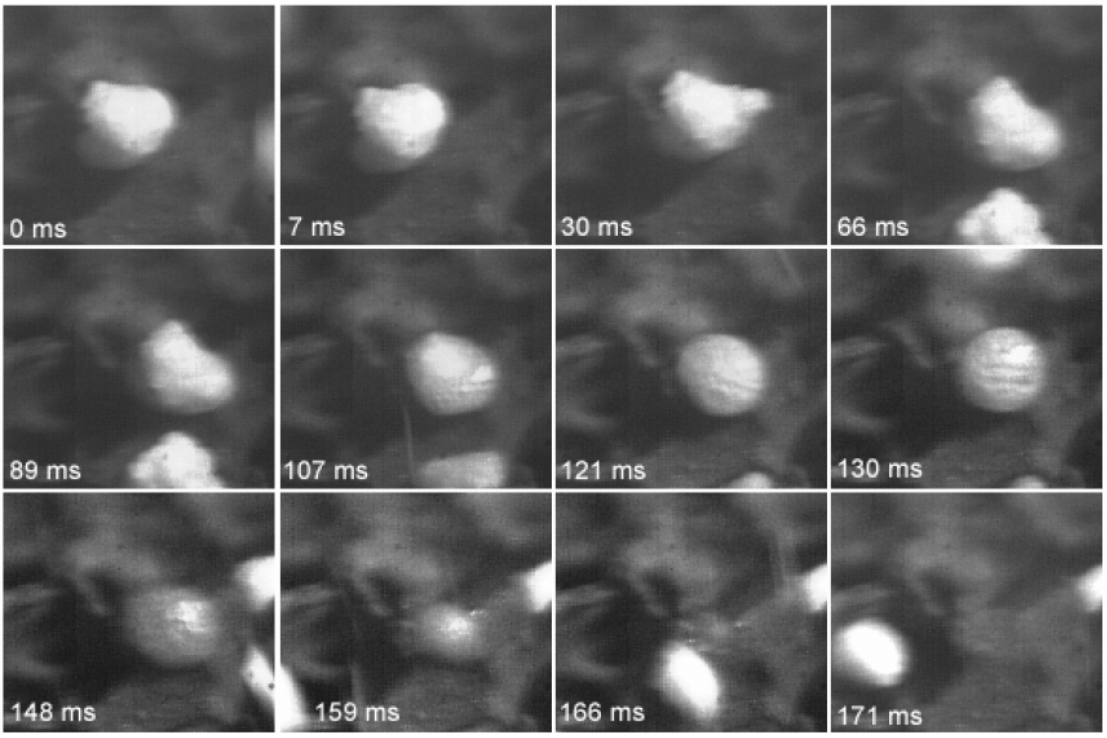

Figure F.4: Conversion of ∼300 μm microcrystalline cellulose particle to volatile species on a 700 °C Rh-Ce/α-Al_2O_3 surface. Cellulose passes through a molten intermediate state before volatilizing completely.

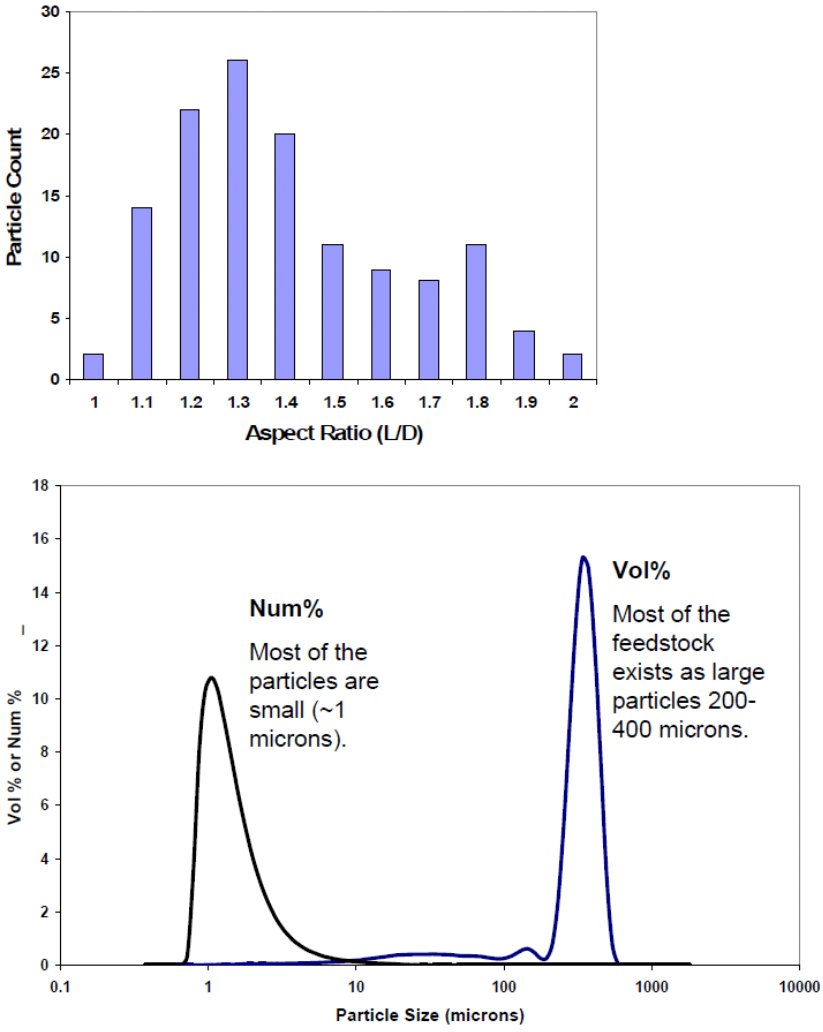

Figure F.5: Top: Particles of microcrystalline cellulose exhibited a distribution of aspect ratios defined as length/width with average aspect ratio 1.39±0.05. Bottom: Sieved microcrystalline cellulose considered in the small particle experiments exists mostly as ∼300 μm particles, but most of the particles are small (∼1 μm). Particle size distributions were collected by light scattering.

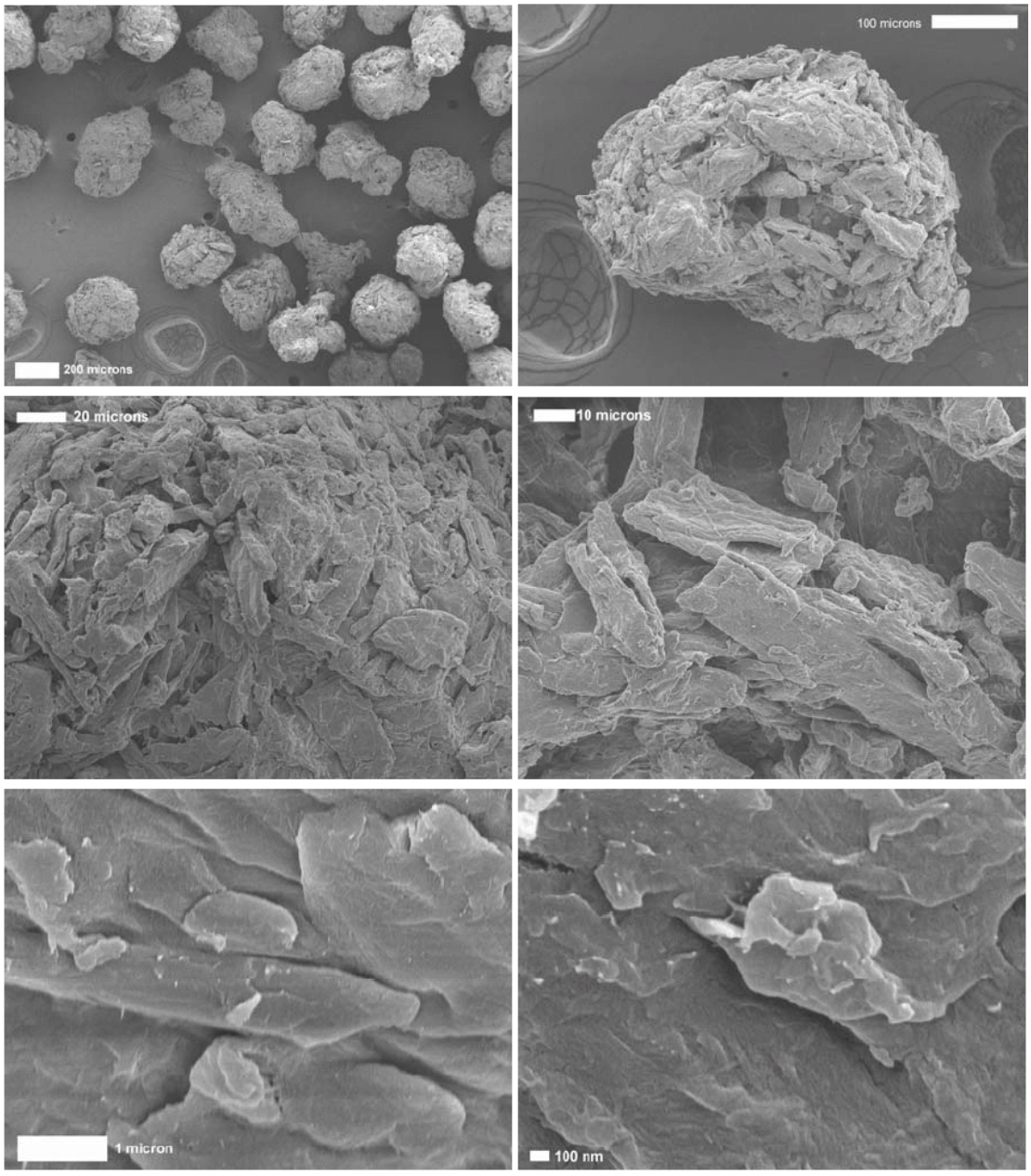

Figure F.6: Microcrystalline cellulose particles sieved to 300 μm average particle size (by volume) are shown. Particles exist as porous structures of crystalline cellulose rods 1-20 microns in width.

As shown in the three panels of Figure F.7, the proportionality constant decreased with increasing surface temperature.

Particles landing on struts of the catalytic foam within the depth of field of the camera were clearly visible and measurable during their conversion lifetime. All observable particles exhibited nearly constant (or only slightly decreasing) width for most of their lifetime through the conversion from solid to liquid. Near the end of the particle conversion, fast linear decrease in particle width was observed.

F.4 Method for Small Particle Conversion on Catalytic Flat Surfaces

Particles of cellulose and sucrose pyrolyzing on a flat catalytic wafer (Rh-Ce/α-Al_2O_3, 2.5 wt% each) were also recorded using a high speed camera using the experimental setup depicted in Figure F.8. A quartz reactor was held in place 1-2 cm above the catalytic wafer by metal clamps. Air was supplied by a high pressure gas cylinder through a needle valve, and particles of solid material were supplied from a side tube sealed with a pushrod. A quartz fiber light pipe delivering light to an optical pyrometer was attached through the quartz reactor such that it contacted the catalytic surface. A butane torch was clamped directly below the catalytic wafer such that its distance was adjustable to control the surface temperature. The high speed camera was placed at a low angle relative to the flat surface ($\sim$10°) obtaining light through a flat Pyrex protector plate. Light was provided from behind the particles.

Figures F.9 and F.10 depict the conversion of two very different shaped cellulose particles at 700 °C. Both particles generate a liquid layer in contact with the surface followed by gas evolution as small bubbles. The liquid layer progresses up the particle finally generating a fully liquid droplet. The liquid droplet, hemispherical in shape, decreases rapidly in size leaving a clean surface behind.

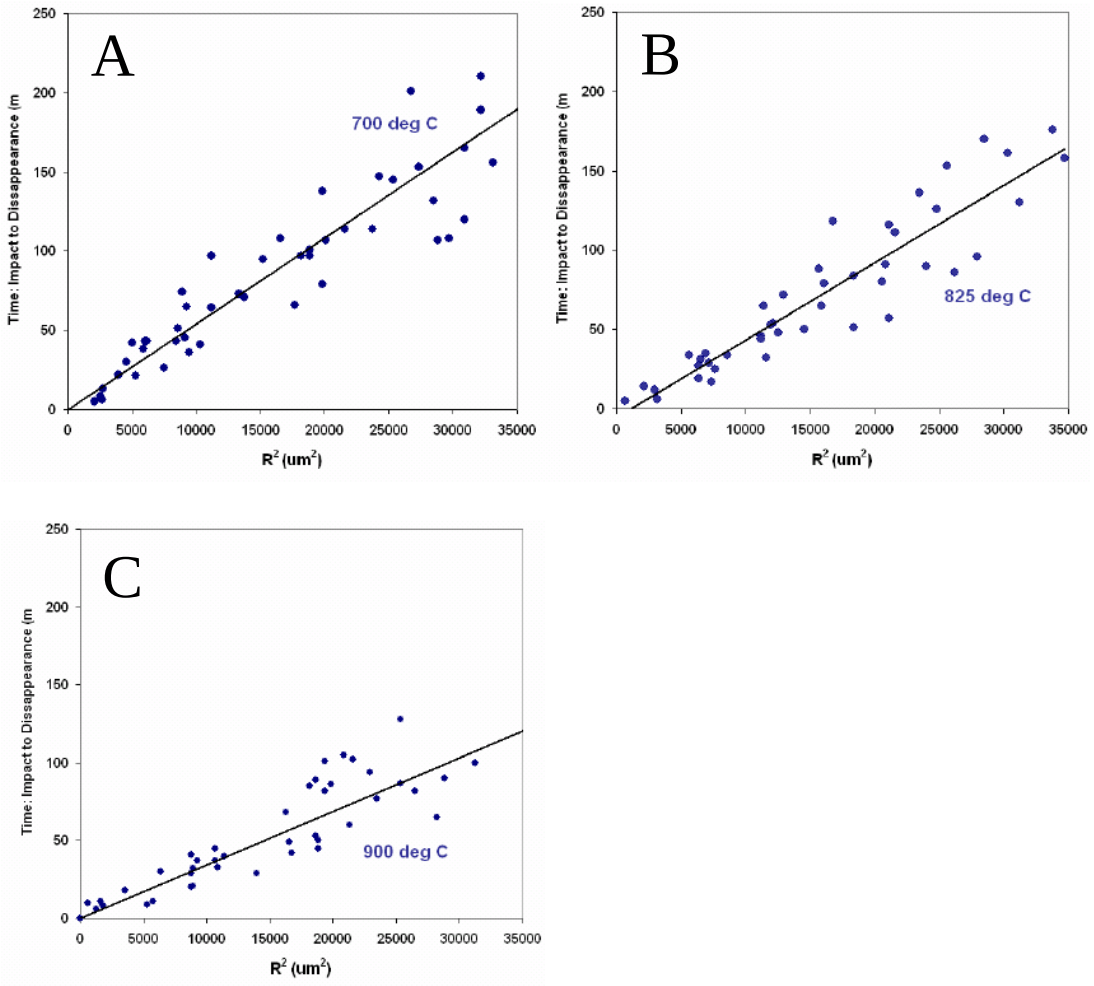

Figure F.7: Microcrystalline cellulose particle conversion time as a function of size on a hot Rh-Ce foam catalyst at variable temperatures. Panel A: $T_{surface}$=700 °C, 1.52 SLPM air flow, 53.1 g hr^{-1} cellulose flow, C/O=1.15; Panel B: $T_{surface}$=825 °C, 2.21 SLPM air flow, 37.2 g hr^{-1} cellulose flow, C/O=0.55; Panel C: $T_{surface}$=900 °C, 1.98 SLPM air flow, 30.6 g hr^{-1} cellulose flow, C/O=0.51. The conversion of microcrystalline cellulose particles on Rh-Ce/α-Al_2O_3 foam supports (80 ppi) exhibited conversion time in milliseconds (impact to disappearance) linearly dependent on the square of the particle radius. Hotter surfaces decreased conversion time by increasing heat transfer rates to the particle.

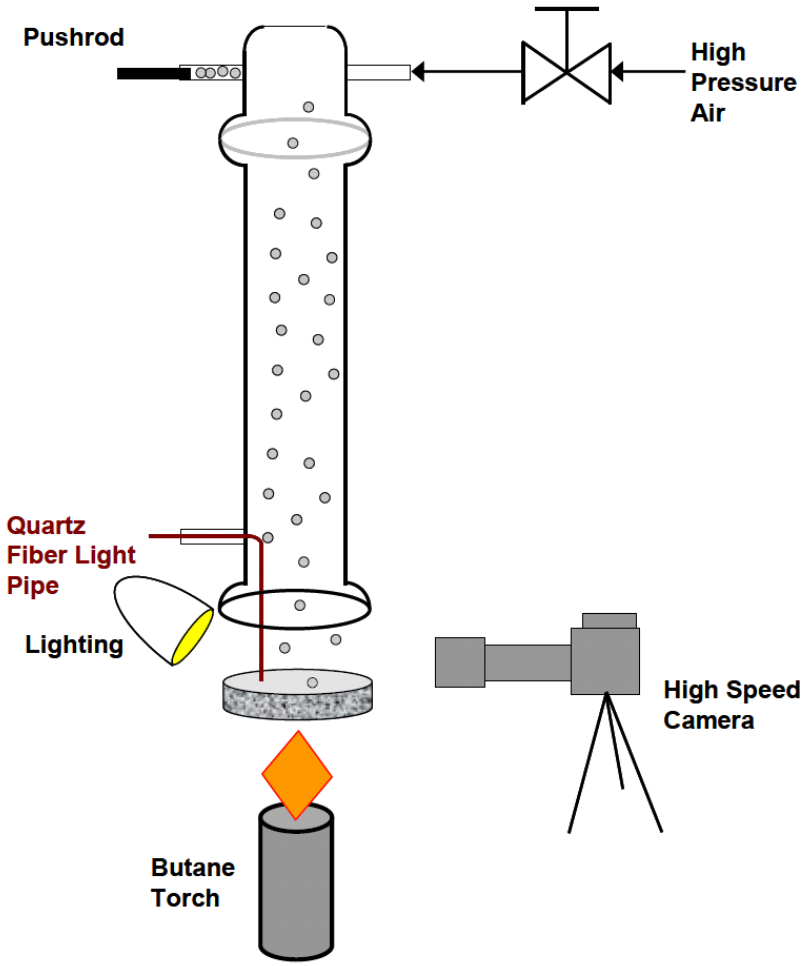

Figure F.8: Cellulose particle conversion was studied on RhCe-coated alumina wafer in air heated from below by a butane torch. Particles were fed to the surface by addition to the side of the reactor by a sealed push rod. Air was supplied by a compressed cylinder through a needle valve to control the flow. A quartz fiber light pipe was inserted through a side arm and impinged on the leading catalytic surface perpendicularly.

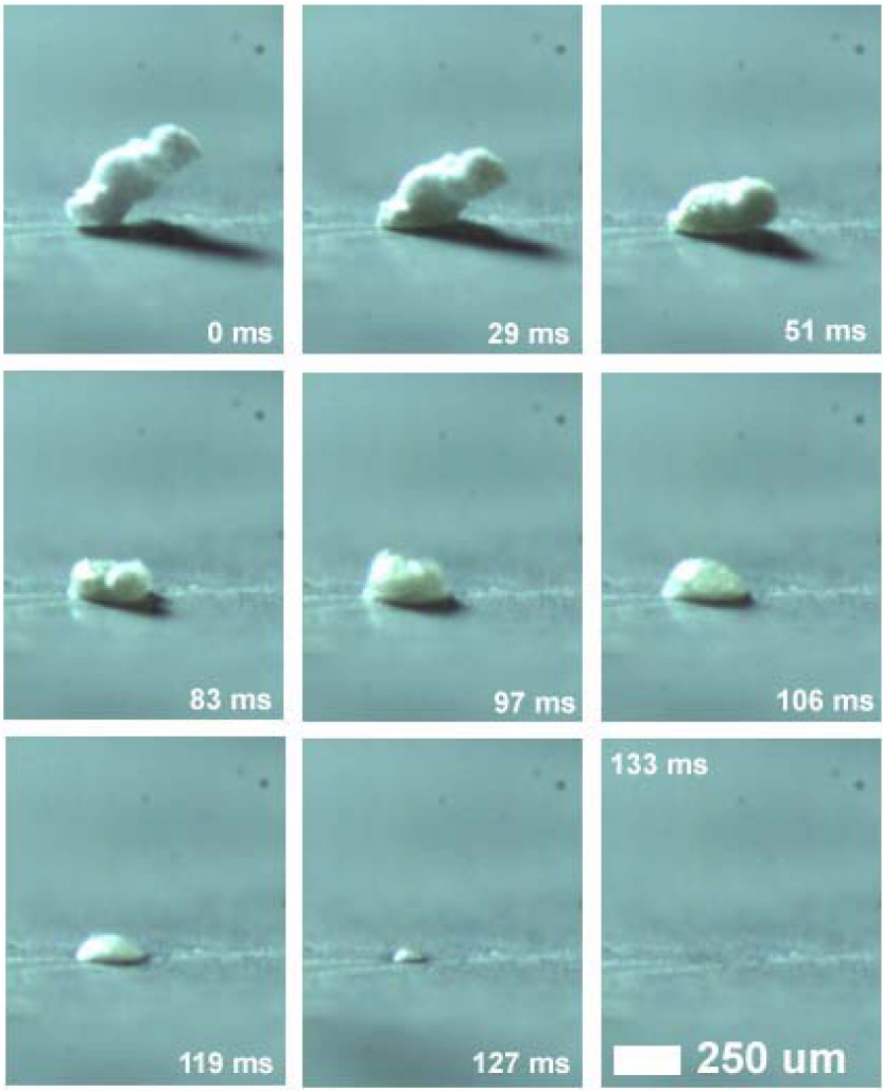

Figure F.9: Additional images of a microcrystalline cellulose particle reacting to volatile species on a hot catalyst wafer surface. Cellulose particle conversion was studied on RhCe-coated alumina wafer in air heated from below by a butane torch at 700 °C.

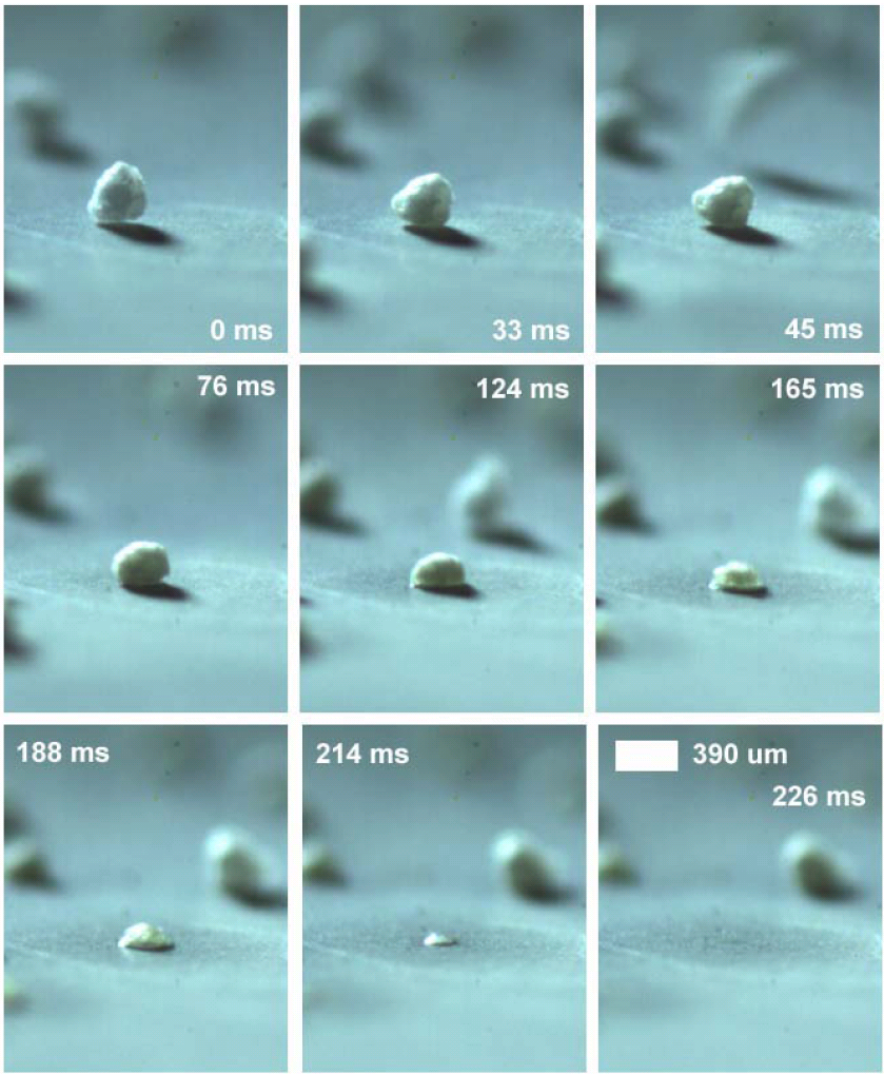

Figure F.10: Additional images of a microcrystalline cellulose particle reacting to volatile species on a hot catalyst wafer surface. Cellulose particle conversion was studied on RhCe-coated alumina wafer in air heated from below by a butane torch at 700 °C.

Calculations in Figure 6.2 were completed using the following equations:

$$R_C = \frac{X^2 + Y^2}{2X} \tag{F.1}$$

$$V = \pi \left(RX^2 - \frac{1}{3}X^3 \right) \tag{F.2}$$

where R_C is the radius of curvature, X is the particle height, and Y is the particle half-width. The height (X) and width (2Y) were measured directly from the video frames by relating the number of pixels to objects of known dimension such as the optical fiber. Calculation of the radius of curvature, which defines the shape of the liquid droplet, permitted the calculation of the liquid droplet volume, V. As shown in Figure F.11 and F.12, the radius of curvature and droplet volume exhibited constant linear change with time.

Figure F.13 depicts the conversion of a particle of sucrose (mp=190 °C) on the flat catalytic surface at 700 °C. The solid crystalline particle appears very different (transparent with flat surfaces) than the microcrystalline (semi-crystalline) cellulose particle at the moment of impact. The sucrose particle rapidly melts to a nonvolatile liquid droplet which initiates reactive gas and volatile organic evolution. The liquid droplet rapidly decreases in volume leaving a clean, flat surface.

F.5 Glycerol Droplets on Catalytic Foams and Wafers

Glycerol boils under atmospheric pressure at ∼290 °C permitting a liquid particle to form a gaseous film between itself and a hot surface. Figure F.14 shows the impact dynamics (impact and breakup) of a large particle (∼800 μm) of glycerol on a catalytic foam at 650 °C. Due to its boiling point restriction, the temperature difference between the surface and the particle must be approximately 350 °C. The key observation of the frames (particularly 27-47 ms) is the absence of the nucleating gaseous bubbles.

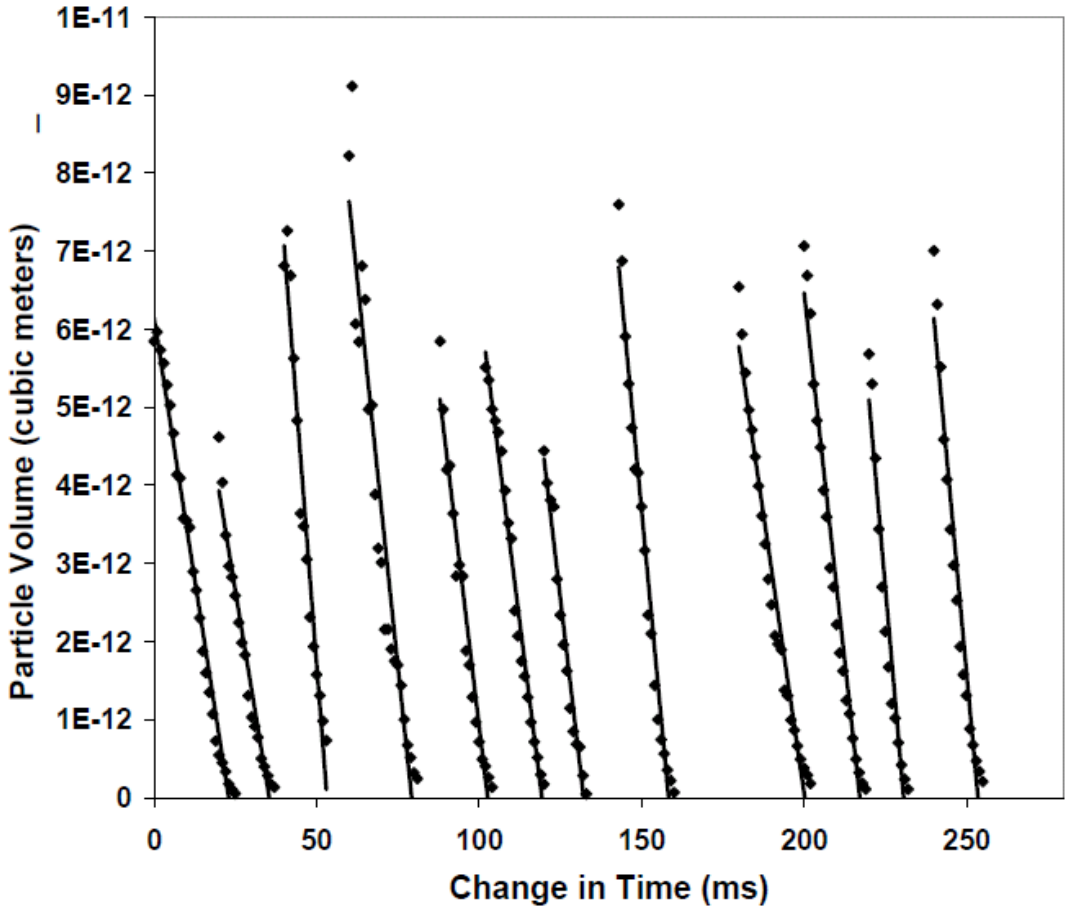

Figure F.11: Cellulose particles completely converted to liquid exhibit approximately linear change in volume as a function of time. Twelve particles are shown decreasing in volume starting from arbitrary time.

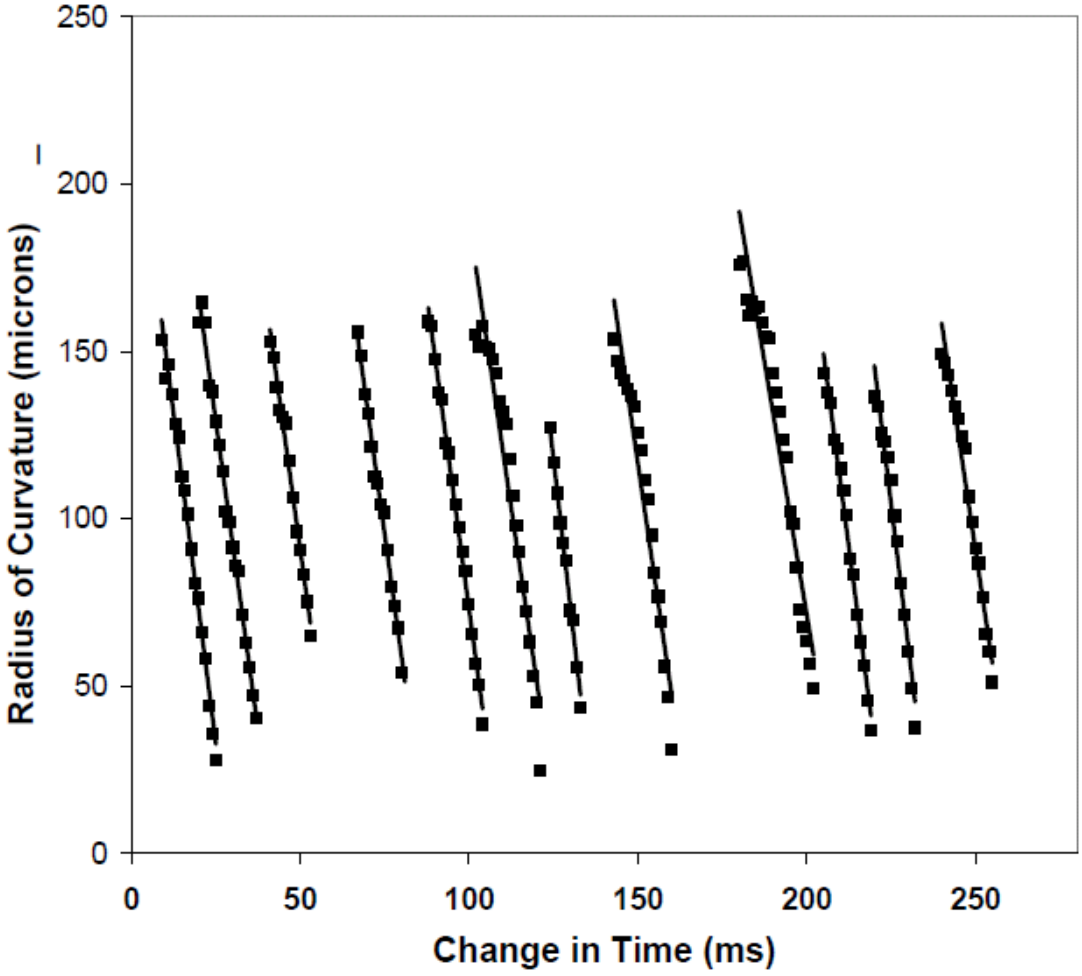

Figure F.12: Cellulose particles completely converted to liquid exhibit approximately linear change in radius of curvature as a function of time. Twelve particles are shown decreasing in radius starting from arbitrary time.

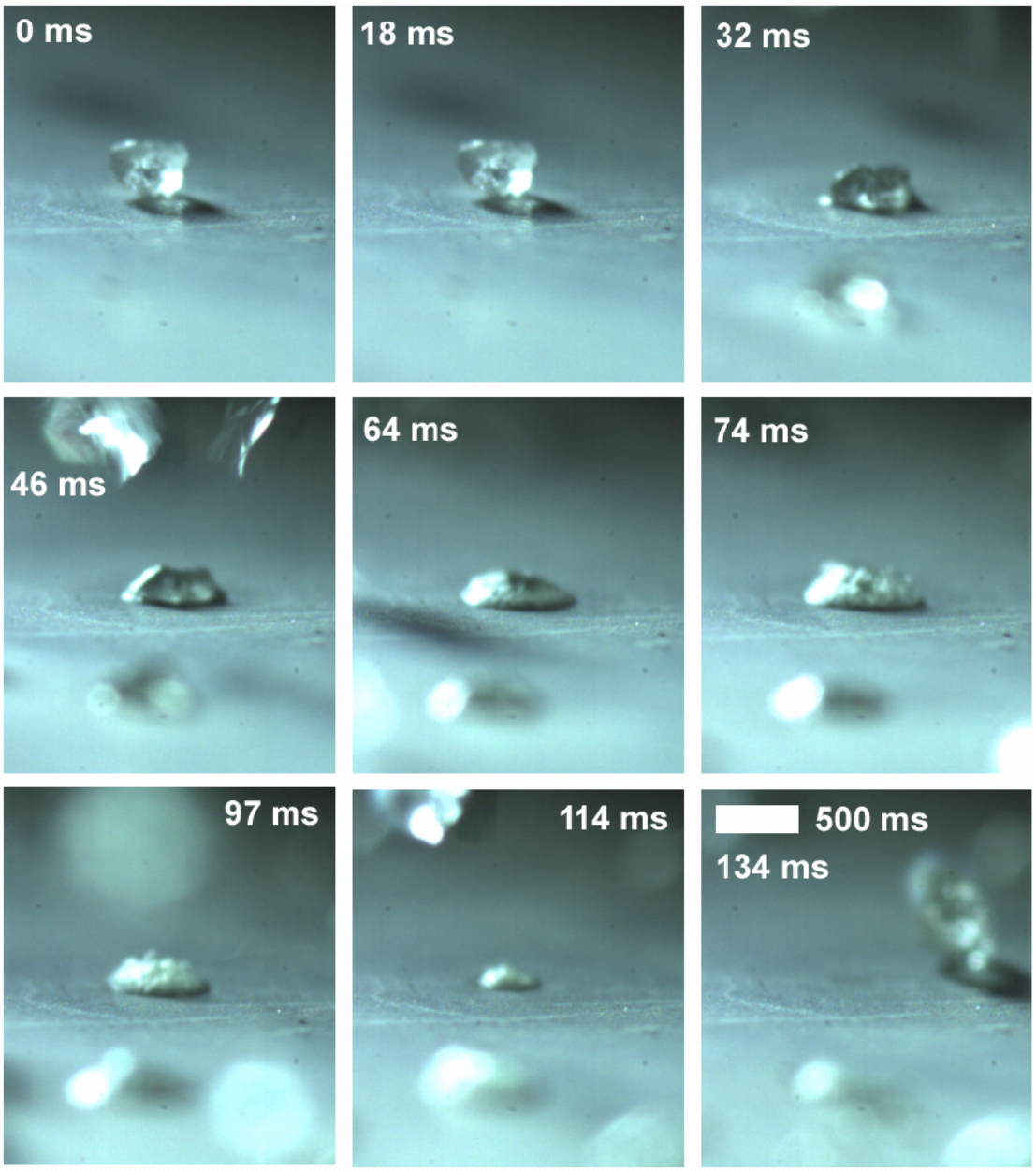

Figure F.13: Crystalline sucrose particle conversion was studied on RhCe-coated alumina wafer in air heated from below by a butane torch at 700 °C.

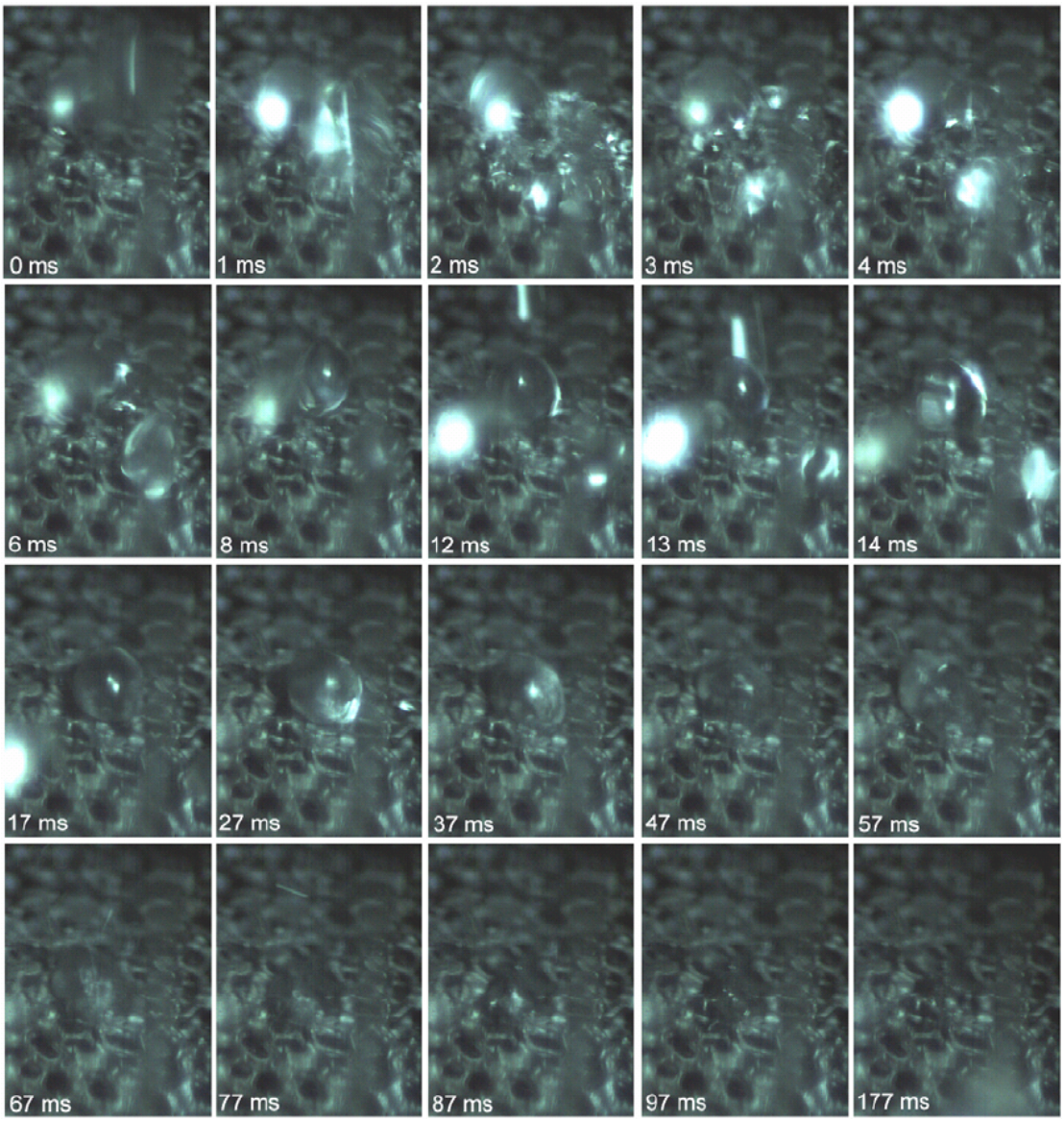

Figure F.14: Impact of a large droplet (∼800 μm) of room temperature glycerol on a Rh-Ce (2.5 wt% each) on 80 ppi alpha alumina (99%) foam at C/O=1.5 and a surface temperature of 650 °C measured with an optical pyrometer. Large droplet impact (2 ms) results in two smaller particles with the back particle remaining in the frame until completely disappearing in 177 ms. Original images were collected at 1000 frames per second. Frames have been contrast adjusted. Liquid glycerol droplets do not exhibit development of bubbles but rather appear to move around on the hot surface under a film of gas consistent with the Leidenfrost phenomenon.

F.6 Method for Cellulose Rod Experimental Setup

Cellulose rods were prepared by pulping (grinding at high speed in the presence of distilled water) prepared sheets of cellulose-rich biopolymer. Analysis of the cellulose-rich sheets showed that some hemicellulose was still mixed with cellulose (79.8% glucan, 19.5% xylan, 0.3% lignin, 0.4% ash). The liquid pulp was poured into a mold with a mesh bottom (50 cm x 50 cm x 1 cm deep), compressed with a board, and dried for two days. The semi-dry slab was removed from the mold, and air-dried in the presence of a fan for three additional days. The board was then cut using a table saw in the following manner. All four edges were lightly trimmed (1-2 mm) creating a square slab. Strips of cellulose were cut with a saw to 7 mm width. The strips were then trimmed with a razor blade to 7 mm cross width, creating a cellulose rod 7 mm x 7 mm x 500 mm.

Processing of the cellulose rods was performed in the setup outlined in Figure F.15. Three catalytic foams and one blank heat shield were wrapped in ceramic paper and held in place inside a quartz reactor by friction fit. A thermocouple was placed 10 mm down from the leading edge of the catalytic bed. The reactor was wrapped in insulation. Attached to the top of the reactor was a size 20 Pyrex reactor endcap fused to a 1 cm I.D. Pyrex tube extending $\sim$1 m from the top of the reactor. Gases (N_2, O_2, and CH_4) flowed into the cap through the outside of the annulus to the catalyst. A quartz light pipe was inserted into the outside of the annulus and down to the leading edge of the catalyst. The long Pyrex tube was graduated (Δx=1 cm) along its entire length to measure the movement of the rod with time. Metal weights (60, 120, 180 g) were inserted through the top of the tube, and an end cap assured a reactor seal. The catalytic reactor was attached to a secondary fixed bed reactor with 9 cm long by 18mm diameter of Rh-Ce/α-Al_2O_3 spheres. The secondary bed assured that all organics were broken down to non-condensible carbon species (CO, CO_2, CH_4) for measurement with a gas chromatograph. The secondary reactor bed was wrapped in a resistive heater and then in 1 inch thick ceramic insulation and the bed temperature was maintained at 700 °C.

Effluent gases were sampled during initial rod experiments to validate carbon flow rates measured visually.

The reaction was initiated by flowing CH_4, O_2, and N_2 over the catalyst and supplying heat externally from a butane torch. Methane was selected as the control fuel due to its inability to exhibit homogeneous chemistry at the considered temperatures upstream of the catalyst where the virgin cellulose rod rested. The methane catalytic partial oxidation (CPO) reaction lit off at ~350 °C generating sufficient heat to initiate an orange glow at the leading edge of the catalyst. The rod was supported on a sealed pull-pin and dropped on the catalyst after light off. Initiation of the methane CPO reaction generates sufficient heat to initiate cellulose decomposition. In general, 5-10 cm of rod was permitted to process before data was collected to allow steady-state processing conditions. The first catalyst was replaced every three rods.

Figure F.16 shows the surface temperature measured with the optical pyrometer attached to the quartz light pipe on the surface of the reaction catalyst. Without the presence of a cellulose rod, methane CPO exhibited $T_{surface}$ behavior that was satisfactorily fit with a third degree polynomial as a function of the dilution parameter (N_2 mol%). The methane temperature served as a measure of the bulk surface temperature. Naturally, the interaction of the rod with the catalyst foam will alter the temperature immediately at the interface in a complex manner requiring future study.

Figure F.17 shows that rod height as a function of time for three rods with the 60 g weight as a function of the bulk surface temperature to demonstrate the behavior of continuous, steady state cellulose processing. Each data point represents the recorded time at which the top edge of the cellulose rod passed a length marker on the reactor tube. These experiments generated a large number of measurements for each experimental parameter combination by examining multiple applied pressures and dilution parameters.

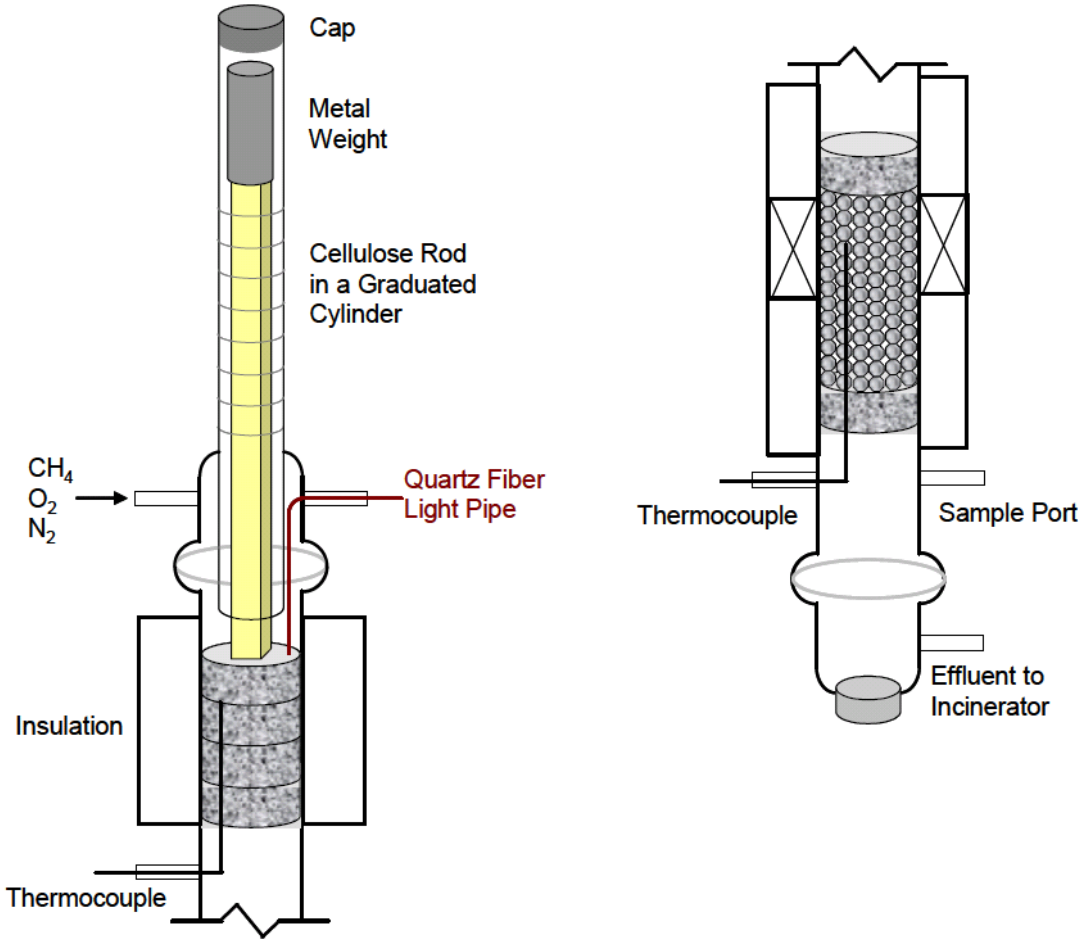

Figure F.15: Conversion of cellulose rods to synthesis gas was examined using a RhCe-coated 80 ppi alumina foam catalyst in a 20 mm I.D. quartz reactor wrapped in ceramic insulation. A size 20 Pyrex tube end-cap was fused with a graduated 1 cm O.D. Pyrex tube extending ∼1 m above the reactor and 1 cm past the interface between the end-cap and the reactor. Cellulose rods (7 mm by 7 mm) placed in the Pyrex tube were pressed against the foam catalysts by cylindrical steel weights placed on top of the cellulose rod. A thermocouple was placed in the catalytic bed 10 mm from the catalyst/cellulose interface. A quartz light pipe fiber was inserted in the feed end-cap and contacted the catalyst perpendicularly. Effluent gases then passed over a 9 cm RhCe bed of spheres heated by an external resistive heater to 700 °C to ensure complete breakdown to combustion products and synthesis gas. Products were sampled with a syringe, and the effluent was passed to an incinerator.

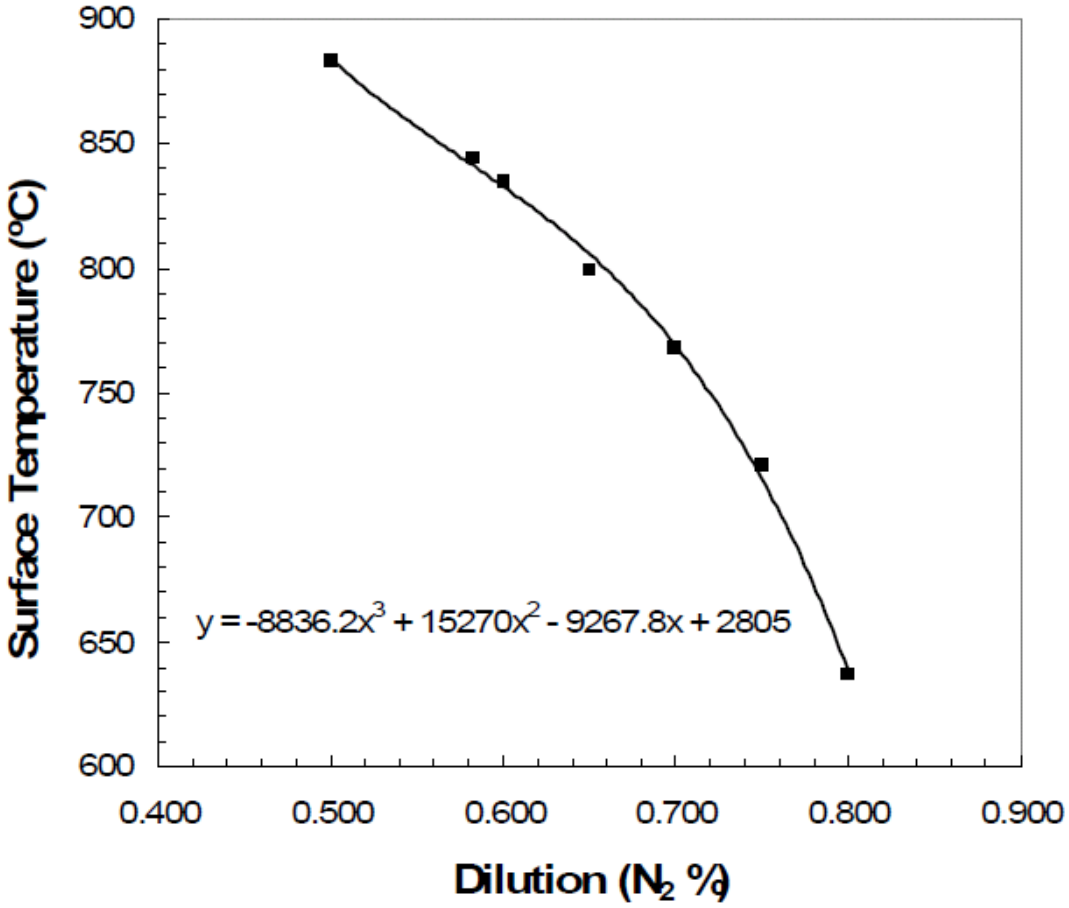

Figure F.16: The bulk surface temperature was measured using an optical pyrometer collecting light through a quartz light pipe touching the surface of an Rh-Ce/α-Al_2O_3 80 ppi foam operating with CH_4, O_2 and N_2. The total gas flow rate was maintained at 5.0 SLPM, and the C/O ratio was maintained at 0.8. The dilution (N_2 / (N_2 + O_2 + CH_4)) was varied between 0.5 and 0.8 to vary the surface temperature on the catalytic foam.

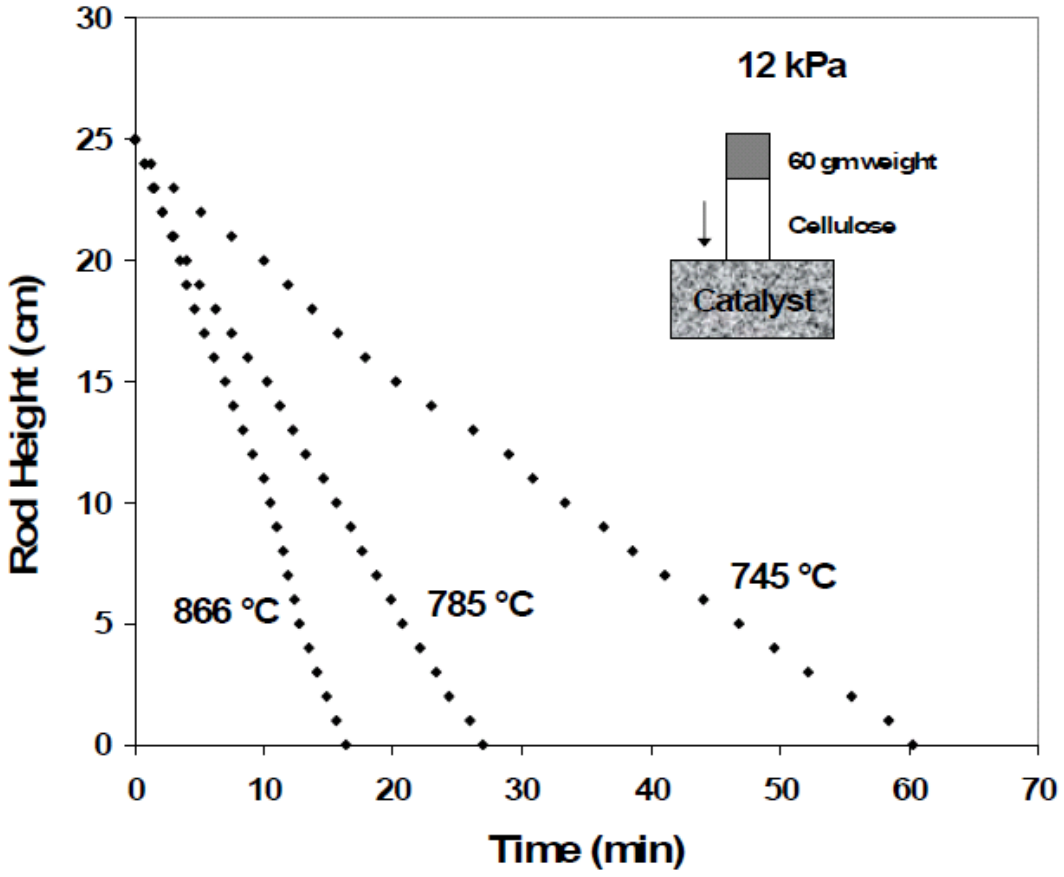

Figure F.17: Rods of cellulose (7 mm x 7 mm x 500 mm) were pressed against an operating Rh-Ce/α-Al_2O_3 80 ppi foam catalyst operating with CH_4, N_2 and O_2. The rate of rod pyrolysis was measured as rod height as a function of time.